

Alma Mater Studiorum – Università di Bologna

DOTTORATO DI RICERCA IN
INGEGNERIA ELETTRONICA, TELECOMUNICAZIONI E
TECNOLOGIE DELL'INFORMAZIONE

Ciclo XXX

Settore Concorsuale di afferenza: 09/F1

Settore Scientifico disciplinare: ING-INF/02

DESIGN AND MODELLING OF WIRELESS POWER TRANSFER
AND ENERGY HARVESTING SYSTEMS

Presentata da: Marco Fantuzzi

Coordinatore Dottorato

Prof. Ing. Alessandro Vanelli-Coralli

Supervisore

Prof.ssa Ing. Alessandra Costanzo

Co-supervisore

Prof. Ing. Diego Masotti

Esame finale anno 2018

Abstract

This thesis reports the main outcomes of the research activity conducted within the Ph.D. program in Electronics, Telecommunications and Information Technologies Engineering at the University of Bologna, Italy. Close collaboration with the COST action IC1301, WIPE - Wireless Power Transmission for Sustainable Electronics was carried on throughout the whole duration of the Ph.D. studies. Two distinct visiting research periods were completed at KU Leuven, Belgium and LCIS Labs - Grenoble INP, France.

The escalation of the Internet-of-Everything topicality has motivated an increased interest in both academia and industry research for efficient solutions enabling self-sustained smart operations. From the maintenance point of view, indeed, battery-less strategies represent the most valuable way for distributed zero-power standalone electronics. With this purpose, different scavenging techniques are being adopted, gathering energy from different sources such as mechanical, solar, thermal and electromagnetic waves. Due to the wide spread of wireless communication systems, the latter technology has recently benefited a renewed interest. This Ph.D. research activity has been focused on the investigation of new efficient solutions for radiofrequency energy harvesting and wireless power transmission techniques, aiming at improving the state of the art, by also taking into account the imperative necessity of

eco-friendly materials for the development of green electronics. The combination of radiofrequency energy harvesting and ultra-wideband techniques is also proposed as possible candidate for future RFID systems. These functionalities are integrated in a novel, compact and low-profile tag, whose details are provided thoroughly from both electromagnetic and nonlinear circuit viewpoints. Results validation is provided through experimental characterization. Compatibility with the environment is assured by implementation with recyclable material. This concept is then extended with the investigation of more elaborated energy scavenging architectures, including rectenna arrays. Finally, a near-field wireless power transmission system is presented on low-cost materials, therefore suitable for possible mass-market deployment.

Contents

Abstract	i
Contents	iii
List of Figures	vi
List of Tables	xvi
Abbreviations	xvii
Introduction	xx
1 Eco-Compatible Next Generation RFID Tag	1
1.0.1 Objectives and Potential Applications	3
1.1 System Architecture	7
1.2 Integrated UWB-UHF Antenna	8
1.2.1 Antenna Design	10
1.2.2 Antenna Experimental Characterization	16
1.3 Diplexer Network	23
1.4 Taconic Implementation	26
1.4.1 Antenna-Diplexer Connection	29
1.4.2 Diplexer Layout and Performance	30
1.5 Paper Implementation	34
1.5.1 Tag UHF Performance	39
	iii

1.5.2	Tag UWB Performance	41
1.6	Remarks and Future Developments	50
2	Diode Model Optimization for Simultaneous Data and Power Transfer	52
2.1	Experimental Setup and Model Optimization	55
2.2	Model Validation	58
2.2.1	Frequency Validation	59
2.2.2	Fundamental Frequency and Baseband Validation	60
2.3	Remarks and Future Developments	63
3	Rectenna Array for Long Distance Autonomous IoT Tag Localization	65
3.1	System Architecture	68
3.1.1	Performance Evaluation of the Available Solution .	70
3.2	Single Rectenna Design	73
3.3	Four Dipoles Rectenna Array	79
3.4	Two Monopoles Rectenna Array	89
3.5	Remarks and Future Developments	94
4	Low-Cost UHF Near-Field Contactless Solution for RFID Applications	95
4.1	WPT for RFID Applications	96
4.1.1	DGS Resonators	98
4.1.2	Low-Cost Materials	100
4.2	WPT Implementation	101
4.2.1	DGS Parametric Study	103
4.2.2	Experimental Validation on Different Materials . .	106
4.3	RFID Reader Antenna	110
4.3.1	Antenna Implementation	110

Contents

4.4 Remarks and Future Developments	114
Conclusions	115
Acknowledgements	118
List of Achievements	119
Bibliography	124

List of Figures

1	Building blocks of a far-field WPT or EH system.	xxiv
1.1	Representation of the GRETA system.	4
1.2	Example of GRETA potential application for logistics and industrial production chain.	6
1.3	Example of GRETA potential application for smart hospital.	7
1.4	Schematic representation of the GRETA tag architecture, where the highlighted area corresponds to the described design activity.	8
1.5	Modeled dc output power for two comparable rectennas, operating at 900 and 2450 MHz.	9
1.6	Integrated UWB-UHF one-port antenna architecture. . .	13
1.7	(a) Final topology of the proposed antenna. (b) Reactance and maximum realized gain as a function of the length of the dipole.	14
1.8	Full-wave simulation results in terms of surface current magnitude in the UHF and UWB bands.	15
1.9	Antenna performance in terms of reflection coefficient, without dipole (gray line) and with dipole (black line).	16

1.10	Antenna performance in terms of realized gain in the yz-plane at the central UWB band frequency of 4 GHz, without dipole (gray line) and with dipole (black line).	17
1.11	Antenna simulated axial ratio at the central UWB band frequency of 4 GHz, with and without dipole, in the yz- and xz-plane.	17
1.12	Photo of the FR-4-based prototype: (a) front view and (b) perspective view with the coaxial cable used in radiation pattern measurements.	18
1.13	Measured and modeled antenna input impedance: (a) real part; (b) imaginary part in the UHF band; (c) real part; and (d) imaginary part in the UWB band.	19
1.14	Measured and modeled reflection coefficient in the UHF band (normalized to 12Ω). $0.5\text{-}\lambda$, $1.5\text{-}\lambda$, and $2.5\text{-}\lambda$ resonances can also be recognized.	20
1.15	Measured and modeled reflection coefficient in the UWB band (normalized to 120Ω).	20
1.16	Measured and modeled normalized field radiation patterns of the co- and cross-polarized component at 868 MHz, in the (a) E-plane (yz) and (b) H-plane (xz) of the dipole.	21
1.17	Measured and modeled normalized field radiation patterns at 3, 4, and 5 GHz, in the yz-plane (left column), and in the xz-plane (right column).	22
1.18	Simulated (solid line) and measured (markers) realized gain of the FR4-prototype in the (a) UHF band and (b) UWB band.	23

1.19 Schematic of the diplexer circuit topology. Port 2 is an artificial termination introduced for evaluation of the diplexer performance.	24
1.20 Simulated scattering parameters of the three-port network of Fig. 1.19 in the (a) UHF band and (b) UWB band.	25
1.21 Diplexer UHF (a) matching and (b) filtering performance distortion during the UWB modulation (SC - Short Circuit, OC - Open Circuit).	27
1.22 Filter insertion loss in the UWB band for different incident UHF power levels.	27
1.23 Photo of the Taconic-based prototype with the corresponding dimensions. The highlighted part in the center part of the antenna represents the diplexer area on the backside of the tag.	28
1.24 Representation of the antenna-diplexer connection. A removal in the diplexer ground plane allows one of the two balanced lines to reach the diplexer top layer.	31
1.25 Diplexer (a) layout representation and (b) photo of the realized prototype. With reference to Fig. 1.19, the ground plane aperture corresponds to port 1, which connects to the antenna, test port corresponds to port 2 and UWB modulator/test port corresponds to port 3.	31
1.26 Comparison between the measured and simulated reflection and transmission coefficient at ports 1 and 3 of the Taconic diplexer. Both ports are normalized on 50 Ω . . .	32

1.27 RF-to-dc conversion efficiency for low levels of RF incoming available power. Inconsistent measured results are a consequence of the inaccurate manufacturer model of the Schottky diodes.	34
1.28 Pictures of the complete tag realized on Taconic substrate.	35
1.29 Tag architecture: (a) side multilayer view and (b) zoomed perspective 3-D view, where the multiple layers are made transparent for ease of visualization.	36
1.30 Comparison between modeled gain patterns of the standalone antenna and the antenna with the back side diplexer at the UWB central frequency (4 GHz).	36
1.31 (a) Integrated UWB-UHF antenna layout. (b) Prototype on paper substrate.	37
1.32 Simulated and measured integrated UWB-UHF antenna reflection coefficient with respect to 50Ω (vector network analyzer reference impedance).	38
1.33 Comparison between measured and simulated antenna input impedance in the UHF band, (a) real part and (b) imaginary part.	38
1.34 (a) Miniaturized diplexer layout, with area $13.2 \times 13.2 \text{mm}^2$ and thickness $370 \mu\text{m}$. (b) Picture of the prototype on paper substrate.	39
1.35 RF-to-dc conversion efficiency and rectified voltage on the optimum load for typically available RF input power levels.	41

1.36 Comparison between measured and modeled diplexer antenna port return loss and antenna-to-UWB port insertion loss. Both UWB port and antenna port are referred to 50Ω terminations.	42
1.37 (a) Antenna in receiving mode. (b) Corresponding equivalent circuit representation in frequency domain for the HB analysis.	44
1.38 Antenna distortion effects on the received pulse. (a) UWB pulse incident on the antenna. (b) Received pulse by the standalone antenna, for fixed polarization ($\psi = 0^\circ$) and varying incident elevation θ angle. (c) Received pulse by the standalone antenna, for fixed AOA and two different polarizations of the incident field. (d) Received pulse by the standalone antenna and the complete tag with the diplexer.	45
1.39 UWB communication measurements in a real office scenario.	47
1.40 Representation of a passive backscattering communication, showing all the distinct signal components: clutter, tag structural mode and tag antenna mode (the only one dependent on the information).	48
1.41 Received measured backscattered signal amplitudes: (a) at the oscilloscope with no processing and (b) after post-processing, for a fixed reader-tag distance of 70 cm. . . .	49

2.1	Schematic representation of (a) a conventional, separated, harvesting and information receiver architecture, where two distinct nonlinear conversion units are employed and (b) integrated harvesting and information architecture, featuring a single nonlinear rectifying/mixing section followed by a low-pass filter.	53
2.2	LSNA vector-calibrated measurement setup adopted for the single diode measurements. In the center part of the picture it is possible to see the PCB on Rogers substrate.	56
2.3	Magnitude of the transmitted voltage waves at the third-order (a) low and (b) high IM products around the fundamental frequency and respective phase (c-d).	58
2.4	Magnitude of the transmitted voltage waves at the (a) first and (b) second IM products in the baseband and respective phase (c-d).	59
2.5	(a) Picture of the full-wave rectifier and (b) and comparison between measured and modeled OC dc voltage at the rectifier output, for a fixed input RF power of -10 dBm.	60
2.6	(a) Picture of the single-diode rectifier, realized on 0.76 mm-thick Rogers RO3003 substrate and (b) NVNA measurement setup.	61
2.7	(a) dc output voltage of the single-diode rectifier for different values of RF input power and (b) output voltage wave magnitude at the first IM product in the baseband.	62
3.1	Schematic representation of the system architecture.	68
3.2	Detailed representation of the digital electronic blocks.	69

3.3	Schematic representation of a multi-stage rectifier topology for voltage multiplication, connected to the UHF antenna through a proper matching network.	72
3.4	Circuit schematic of the monopole rectenna. The RF available power is modeled as an ac voltage source with the antenna impedance as internal resistance. V_{rect} and V_{WUR} are fed at the input of the respective electronic block described in Fig. 3.2.	74
3.5	Picture of the monopole rectenna prototype. The zoomed view shows the layout of the rectifier and wake-up circuitry.	76
3.6	Comparison between measured and modeled (a) OC voltages at the output of the rectifier and wake-up sections and (b) RF-to-dc conversion efficiency and dc voltage on the optimum load of the rectifier, for different values of RF input power.	76
3.7	Comparison between measured and modeled dc voltage at the rectifier and WUR outputs for different values of (a) the rectifier load and (b) the WUR load.	78
3.8	Modeled dipoles (a) reflection coefficient and (b) mutual coupling. Ports numbers are in accordance with the numbering of Fig. 3.9.	81
3.9	Layout of the quasi-isotropic four-element harvester, coplanar with a UWB spiral antenna for the optimum dipole distance $d = \lambda/4.3$. Dimensions $100 \times 100 \times 1.5 \text{ mm}^3$, designed on Rogers RO4350B substrate ($\epsilon_r = 3.48$, $\tan(\delta) = 0.0037$ at 10 GHz).	82

3.10 Gain patterns of dipole 1 in $\varphi = 90^\circ$ -plane (yz-plane) (see Fig. 3.9), for different inter-dipole distances $d = \lambda/x$. . .	82
3.11 3D gain pattern of dipole 1 for the optimum dipole distance $d = \lambda/4$. Identical gain patterns pertain to the other three dipoles, with a 90 degrees rotation along φ . . .	83
3.12 Near-field behavior in terms of (a) self-admittances and standalone dipole admittance, (b) trans-admittances. . .	85
3.13 Topology of the multi-rectenna series dc connection. Each stage number corresponds to the respective dipole of Fig. 3.9. Matching networks of stages 2 to 4 are identical, while the first stage is optimized for the provisioning of the additional WUR output.	86
3.14 Representation of the final layout and picture of the four-rectenna array prototype. Red lines on the left image represent metalizations on the bottom side of the PCB. . .	86
3.15 Circuit schematic of the two-monopole rectenna array with decoupling network.	90
3.16 Picture of the realized two-monopole prototype. The bottom-left part of the tag, containing a green solder mask, is designed for integration of the electronic components.	91
3.17 Comparison between the measured and modeled insertion and return loss at the two test ports, in correspondence of the interface between the decoupling network and the two rectifying sections.	93

3.18 Comparison between measured (a) dc power and (b) dc voltage for the single monopole and the two-monopole array rectennas for different distances from a CP UHF source, transmitting 2 W ERP. PMU requirements are highlighted in red. The optimum load for the two-monopole array is equal to 15 k Ω	94
4.1 Schematic representation of a contactless connection between the RFID reader processing unit and the reader antennas.	98
4.2 (a) H-shaped DGS, where the capacitive and inductive areas of the deflection are highlighted and (b) equivalent circuit representation.	99
4.3 Multilayer substrate representation. Two PET layers with printed conductive aluminum are employed as top and bottom metalization, linoleum is used as main dielectric substrate.	100
4.4 Schematic representation of the designed DGS: (a) top view, where the line width is set for a 50 Ω characteristic impedance and (b) bottom view, showing the interdigital capacitor. The bottom dotted black line marks the DGS section, at the far end of the multilayer microstrip line.	102
4.5 Perspective view of the two microstrip lines ending/beginning with the DGS section. One layer of linoleum is placed as spacer between the two DGSs.	103
4.6 Tuning of the resonant frequency obtained by varying the significant parameters of the DGS. The black curve represents the reference starting point, obtained for $L_L = 28\text{ mm}$, $W_L = 8\text{ mm}$ and $W_C = 8\text{ mm}$	104

4.7 Effect of the varying distance between the two DGSs in terms of number of linoleum layers, K , placed as spacer between the two. One layer of linoleum has a thickness of 2.55 mm, in accordance with Fig. 4.3. DGS dimensions are in this case $L_L = 27\text{ mm}$, $W_L = 8\text{ mm}$, $W_C = 8\text{ mm}$ and $L_{stub} = 18\text{ mm}$. (a) Reflection coefficient and (b) transmission coefficient. 105

4.8 Pictures of the measurement setup on different material. (a) Non-metallic support. (b) Metallic support. 107

4.9 Comparison between simulated and measured reflection and transmission coefficients for the first prototype, over non-metallic material. 108

4.10 Comparison between simulated and measured reflection and transmission coefficients for the second prototype, over non-metallic material. 109

4.11 Comparison between simulated and measured reflection and transmission coefficients for the third prototype, over metallic material. 109

4.12 Schematic representation of a possible application for RFID antenna contactless feeding. 111

4.13 Comparison between the measured and simulated contactless fed patch antenna return loss. In the zoomed graph it is possible to observe the frequency shift due to air-gaps. 112

4.14 Picture of the realized contactless fed patch antenna prototype, tested in the anechoic chamber. 113

4.15 Measured and simulated gain patterns of the contactless fed microstrip patch antenna, in both H- and E-planes. . . 113

List of Tables

1.1	List of SMD components of the diplexer Taconic implementation.	32
1.2	List of SMD components of the diplexer paper implementation.	40
1.3	Received power by the UWB reader in different link conditions.	50
1.4	Received power by the UWB reader for different distances.	50
2.1	Schottky Diode Model Parameters.	57
3.1	dc outputs of the multi-stage rectifier topology.	72
3.2	List of SMD components of the monopole rectenna.	75
3.3	List of SMD components of the four-dipole rectenna array.	87
3.4	OC rectified voltage comparison of the presented harvesters.	88
3.5	List of SMD components of the two-monopole rectenna array.	91
4.1	List of realized prototypes.	106

Abbreviations

AGV	Automated Guided Vehicle
AOA	Angle-Of-Arrival
AWG	Arbitrary Wave Generator
BB	BaseBand
CPT	Capacitive Power Transfer
CW	Continuous Wave
DGS	Defected Ground Structure
DUT	Device Under Test
EH	Energy Harvesting
EIRP	Effective Isotropic Radiated Power
EM	Electro-Magnetic
ERP	Effective Radiated Power
EV	Electric Vehicle
HB	Harmonic Balance
HF	High Frequency
IC	Integrated Circuit
IM	InterModulation
IOE	Internet Of Everything
IOT	Internet Of Things
IPT	Inductive Power Transfer
LF	Low Frequency

LHCP	Left Hand Circular Polarization
LOS	Line Of Sight
LSNA	Large Signal Network Analyzer
MCU	MicroController Unit
MPPT	Maximum Power Point Tracking
MPT	Microwave Power Transfer
NLOS	Non Line Of Sight
NVNA	Nonlinear Vector Network Analyzer
PAPR	Peak-to-Average Power Ratio
PCB	Printed Circuit Board
PET	polyethylene terephthalate
PMU	Power Management Unit
POW	Power Optimized Waveform
RF	Radio Frequency
RFID	Radio Frequency IDentification
RHCP	Right Hand Circular Polarization
RSS	Received Signal Strength
RTLS	Real Time Locating System
SMD	Surface-Mount Device
SNR	Signal-to-Noise-Ratio
SPS	Solar Power Satellite
SWIPT	Simultaneous Wireless Information and Power Transfer
TDOA	Time Difference Of Arrival
TOA	Time Of Arrival
UHF	Ultra High Frequency
UWB	Ultra-WideBand
VNA	Vector Network Analyzer
WPT	Wireless Power Transfer

Abbreviations

WSN	Wireless Sensor Network
WUR	Wake-Up Radio

Introduction

The act of conveying power by means of radio waves without a physical connection between source and user was conceived more than a century ago [1, 2]. The first pioneer conducting practical experiments was Nikola Tesla. In the late 19th century, Tesla performed its earliest tests in Colorado Springs, USA, involving wireless power transmission via electric fields, feeding a coil with 300 kW at the low frequency of 150 kHz [3]. The main ambition of Tesla was that of setting up oscillations of electrical energy with vast terrestrial coverage for wireless power broadcasting, to be then collected at remote user locations [4]. With this purpose, in 1901 he began the construction of the Wardenclyffe Tower, a huge installation in Long Islands, New York, USA, which, though, was never completed due to the lack of financial resources.

Contemporary to Tesla's experiments, Guglielmo Marconi was achieving similar discoveries, even though his main motivation in the transmission of radio waves was that of delivering information wirelessly [5]. Nevertheless, in the following decades very few attempts of power transmission without wires were registered, the main one being apparently the demonstration undertaken by Harrell Noble in 1931, where power was transmitted wirelessly between two 100 MHz half-wavelength dipoles at

few meters of distance, with 15 kW used in transmission. The main reason justifying the scarce interest in this field was plausibly the awareness that for the retrieval of meaningful efficiency in the wireless transmission link, the electromagnetic (EM) energy had to be concentrated into narrow beams, which for a practical implementation entailed a shift towards shorter wavelengths.

Microwave technology became sufficiently mature only after World War II, when the technology provided by vacuum tubes allowed the transmission of high power waves at microwave frequencies. In 1963, the first experiment of microwave power transmission was performed by William Brown, who successfully delivered 100 W of dc power with an overall dc-to-dc efficiency of about 13%. The following year, he demonstrated the wireless powering of a model helicopter, by transmitting 5 kW of power at 2.45 GHz, with a 3-meters diameter parabolic antenna. In his later experiments, dated 1975, Brown was also able to demonstrate the wireless reception of 30 kW dc power at about 1.6 km from the transmitter [1].

In the late 20th century strong interest has also been focused on long-distance power transmission from space to Earth [6, 7, 8, 9]. The main motivations were those of finding new ways of better exploiting solar energy. Solar energy harvesting is indeed much more efficient in space compared to terrestrial level and it is also independent from weather conditions and day/night cycles, therefore an array of solar panel placed in space, also known as solar power satellite (SPS), could beam the energy back to earth using microwave radiation. A similar approach was also investigated for powering propel spacecrafts [10]. For such application, the spacecraft would be composed of the receiving harvesting elements instead of containing the conventional propulsion chemicals,

this way reducing its weight and the consequent power needed to propel the craft.

From the dawn of energy transmission without wires with Tesla, to modern age, research in wireless power delivery attained disruptive developments. This technology is considered essential for the industry in several areas of expertise, including consumer electronics, automotive, and industrial control process [11]. Indeed, thanks to the most recent successful breakthroughs, increased interest has emerged also in the industry, as testified by the foundation of different worldwide consortia [12, 13].

Wireless power transmission (WPT) can be defined as the process by which electrical energy is delivered from a power source to a load, without the connection of electrical conductors. When talking about WPT, three different categories can be identified: (i) near-field coupling of inductive or capacitive type in resonant or non-resonant mode, (ii) far-field directive power beaming, and (iii) far-field non-directive power transfer.

The first approach is of non-radiative type and it is used strongly when the device is close to the power source [14, 15, 16, 17, 18, 19, 20]. Well-known and commercially successful applications are primarily for short-range charging of devices, avoiding the need of power cables, such as induction powered toothbrush, or more recent mobile phones being charged by inductive coils [21, 22, 23]. Similar applications are also gaining a lot of attention, such as the recharge of electric vehicles without connecting to an outlet [24, 25, 26], or the wireless transmission of power to charge the battery of pacemakers, without the need for further surgery to replace them [27, 28]. In this case the power mechanism is similar to what happens in a voltage transformer, where a magnetic field traverses

a coil and generates an electromotive force on the secondary inductor, which, if correctly aligned, can power up a device. This method firstly achieved a range of a few millimeters to a meter, and its low efficiency for higher distance imposed certain constraints in terms of possible applications. Nevertheless, this technology evolved to few meters of distance in case of deployment of resonant links, as first demonstrated by a group at the Massachusetts Institute of Technology (MIT): they provided 60 W to a lamp placed 2 m from the transmitter with an efficiency of about 40% [29].

The other two forms of wireless power transmission make use of electromagnetic wave propagation. In this scenario two possibilities are envisioned: the first one, referred to as far-field WPT, or microwave power transmission (MPT), is a technique employing directive power beams, where radiofrequency (RF) power is intentionally sent to a receiver which collects it before performing a conversion into dc power [30, 31, 32, 33, 34]. The latter, conversely, called electromagnetic energy harvesting (EH) exploits the EM energy already present in the environment, coming from existing EM waves radiated from sources not intended for the specific harvesting device [35, 36, 37, 38, 39].

The Ph.D. activity reported in this thesis is mainly focused on far-field WPT and EH-related topics. More specifically, on the receiving part of the WPT system, namely the device responsible for the collection of the RF incident energy and for its successive conversion into dc output. Such device is called rectenna: a compound for rectifying antenna. The concept of rectenna has been first proposed by Brown [1] and identifies the combination of an antenna with a rectifier (RF-to-dc converter), which makes it possible an efficient conversion of RF energy into dc energy.

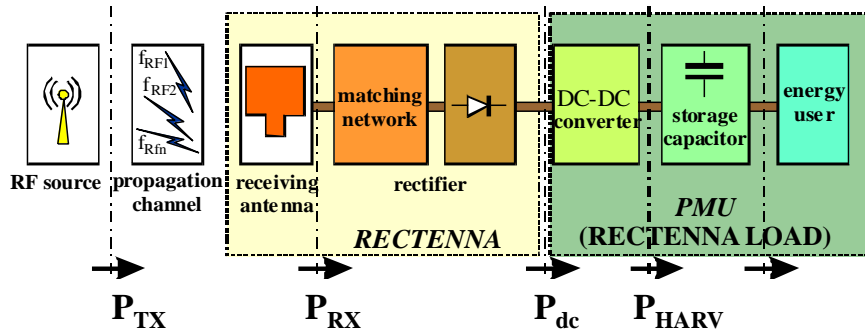


Figure 1: Building blocks of a far-field WPT or EH system.

Fig. 1 displays a representation of a far-field WPT or EH system, highlighting its main building blocks. The RF source can be of many kinds, featuring different characteristics, such as, single frequency (also called continuous wave - CW), multi-band or broadband; different polarizations, namely, linear polarization (LP), right- or left-hand circular polarization (RHCP - LHCP); different power levels, and so on. The second block is the propagation channel, whose effects are often difficult to predict with precision and generally entail a degradation of the RF source, from unavoidable attenuation, to possible alterations of the source polarization. The design of the receiving antenna is typically application specific, with the goal of adapting to the specific RF source(s) available. In case of intentional far-field WPT, for example, both antennas at transmitter and receiver sides are directive, while in case of EH application, rectennas are typically demanded of omnidirectionality features. A challenging aspect, directly affecting the efficiency of the system, is the design of a proper matching network, providing suitable adaptation between the antenna and the rectifying unit respective impedances, challenge further increased by the nonlinearity of the rectifier. As regards the rectification process, this is responsible for the actual conversion of RF power into dc power. For low-power applications Schottky diodes are primarily employed as rectifying elements, mainly due to

their low threshold, and they can be arranged in different topologies, such as half-wave, full-wave, voltage multiplication, and so on. Before being delivered to the final user, the dc output of the rectenna is typically processed by a power management unit (PMU), which can therefore be considered as the reference load during the rectenna design. The PMU is mainly composed by a dc-dc converter and a storage capacitor, which preserves the harvested energy for its final consumption.

When talking about efficiency it is of critical importance specifying which are the precise quantities that are being compared. The RF-to-dc conversion efficiency is defined as:

$$\eta_{RF-dc} = \frac{P_{dc}}{P_{RX}} \quad (1)$$

that is, the ratio between the dc power at the output of the rectenna versus the RF power received by the antenna and made therefore available at the input of the matching network (refer to Fig. 1). On the other hand, dc-to-dc efficiency, defined as:

$$\eta_{dc-dc} = \frac{P_{HARV}}{P_{dc}} \quad (2)$$

always referring to Fig. 1, identifies merely the conversion efficiency of the dc-dc converter contained in the PMU. In other cases dc-to-dc efficiency can also be an evaluation of the whole system efficiency, starting from the dc energy at the transmitter side, before its conversion into RF, the transfer to the receiver and its subsequent re-conversion into dc for the receiver load. Typically, this last definition is mainly embraced in near-field WPT application.

Regardless the specific technique implemented, the objective of WPT is to remove or eliminate all the power cables connected to electronics,

but also to eliminate or at least reduce the needs of charging batteries in electric devices. In particular, far-field WPT systems are expected to be the solution to deploy battery-less distributed electronics that are difficult and/or are in such a large quantities that battery replacement is too costly or even unfeasible. In this case the use of wireless power transmission techniques can be exploited to develop and foster the internet of everything evolution. Indeed, among the countless possible applications of EH and WPT, the Internet of Things (IoT) is most assuredly one of them, especially for low power WPT. The Internet of Things refers to uniquely identifiable objects (things) and their virtual representations in an Internet-like structure. It is expected to bring about massive improvements in user experience and system efficiency. It will have a transformational impact on all industries and re-shape business models and industry configurations. An estimated 30 billion connected devices will be deployed by 2020 [40] and the total IoT revenue is expected to grow to \$1.2 trillion in 2022. As a result, IoT services are expected to be a key driver for growth in the telecommunication industry. In an IoT-perspective, the precise geographic location of a thing will be a strategic requisite [41]. Indeed, some things in the IoT will be sensors, and sensor location is usually important [42]. Therefore, the combination of radiofrequency identification (RFID), real time locating systems (RTLS) and sensor technologies will enable the Internet to observe, identify and understand the world without the limitations of human-entered data [43]. Besides localization, sensing and all the possible implemented features, a paramount prerequisite will be energy supply. Indeed, every single device, or connected object, needs a certain amount of power to operate. It is well known that the usage of batteries entails inherent disadvantages in many situations, such as unsuitability or impracticability

of their replacement, impact on environmental pollution and so on. It is in these cases, especially for low-power μW applications [44, 45], that EH and WPT find room for development.

Throughout the whole duration of my Ph.D. activity I have been mainly dedicated to the design of new solutions for rectennas, envisioned for EH and low-power WPT applications. The following Ph.D. thesis is organized as follows: Chapter 1 describes the design of an eco-compatible tag for simultaneous EH and communication, realized on paper substrate, Chapter 2 introduces a new concept for simultaneous wireless power and information transfer, for which an accurate model of a Schottky diode has been derived, Chapter 3 describes novel solutions for increasing the activation distance of an energy autonomous tag, and finally Chapter 4 illustrates the design of a low-cost near-field WPT system, envisioned for RFID applications.

Chapter 1

Eco-Compatible Next Generation RFID Tag

The evolution of the contemporary society and the developments of information technologies have driven the pervasive diffusion of wireless systems in the environment. More specifically, new systems employing a large number of spatially distributed low-cost nodes (tags) are being adopted in applications among heterogeneous fields such as logistics (e.g., tracking of goods in supply and distribution chains), security (e.g., localization and tracking of authorized people and goods in areas under surveillance), environmental monitoring, and health-care (e.g., monitoring of patients, medical or paramedical personnel, medicines, and health-care equipment). In all these scenarios, tags are required to be identifiable, localizable and capable of sensing physical quantities with high accuracy: functionalities traditionally offered by separated wireless technologies, such as RFID, wireless sensor network (WSN), and RTLS. Indeed, the ultra high frequency (UHF) RFID second generation (Gen. 2) [46] proved its validity in numerous application fields but still does not offer capabilities of localization with high resolution, nor low power

sensing functionalities [47]. RTLS systems present some examples in the commercial world, but uniquely based on active devices (with battery) and with no integrated sensors [48]. Finally, the WSN technology, as RTLS, does not provide either zero-power characteristics by means of backscatter transmission techniques or implementation of components and circuits on eco-compatible materials [49]. Obviously, the possibility to integrate all the aforementioned capabilities in a unique system, with innovative and low-cost solutions, would tremendously extend the range of applications. Moreover, the employed electronics should possess a feature so far considered only marginally and usually *ex post*, but key in the future: full compatibility with the environment.

Given these premises, the Italian national project GRETA (GREen TAGs and sensors with ultra-wideband identification and localization capabilities) [50], was born to focus on the research of innovative solutions and technologies aimed at the realization of a distributed system for identification, localization, tracking and monitoring in indoor and outdoor scenarios, based on environmentally friendly materials. The main goal is that of realizing tags which are:

- localizable with sub-meter precision even in indoor scenarios or in presence of obstacles;
- small-sized (with an area in the order of a few square centimeters) and lightweight;
- eco-compatible (i.e., made with recyclable materials);
- energy-autonomous (no batteries);
- low-cost to permit the employment of several tags in the application scenario;

-
- capable of sensing physical quantities from the environment.

Specifically, to meet the requirements of low energy consumption and high-localization precision ultra-wideband (UWB) techniques are exploited to efficiently transmit identification and positioning information in backscattering from the tags towards the reader [51, 52]. These schemes have been recently proposed and are growing of interest for the unique capabilities of ensuring passive communication (i.e., without the need of equipping the tag with an active transmitter) and high-resolution ranging [53, 54, 55]. For this reason, UWB is adopted for the communication of data generated by the autonomous non-powered sensors. Besides passive backscattering modulation, energy autonomy is reached by implementation of energy harvesting techniques, together with ultra-low power signal processing. Finally, eco-compatible recyclable materials (e.g., paper, polyethylene terephthalate, etc.) are investigated for the substrate of electronic circuits, to assure the “green electronics” feature.

1.0.1 Objectives and Potential Applications

In order to guarantee the correct functionalities of the distributed low power intelligence (zero power smart tags), the GRETA system is designed to rely on an infrastructure composed of cooperative radio nodes (readers) able to perform real-time identification and tracking with sub-meter resolution of tagged objects/persons. Moreover, besides the mere scavenging of ambient RF power, the use of dedicated emitters, denoted as “energy showers”, is also foreseen in the system scenario. The GRETA system architecture is depicted in Fig. 1.1.

The study of these tags/sensors networks, combined with the employment of recyclable materials and energy harvesting systems, paves the way to numerous applications, mainly oriented to the Internet of

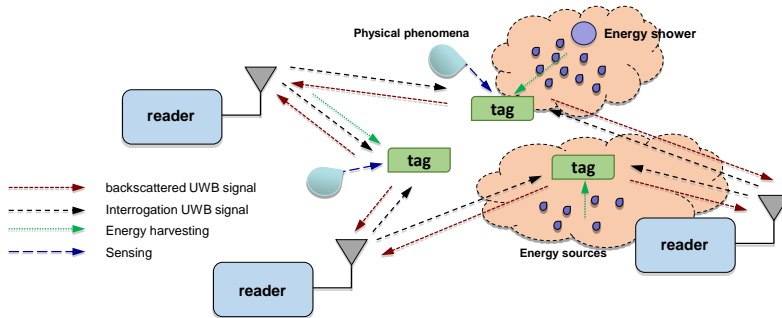


Figure 1.1: Representation of the GRETA system.

Things concept, some of which are also pointed out in the Horizon 2020 objectives. Among them:

- e-Health: energetically autonomous and not invasive sensors for biomedical parameters (e.g., smart band-aids) or drugs monitoring and in general for efficient hospital activities management;
- ICT for food: on-paper tags with embedded sensors for continuous monitoring of the product along the production and commercial distribution chain (e.g., cold chain).
- Factories of the future: goods tracking and monitoring along the industrial process for an advanced logistic management (supply chain management).

Further applications concern domotics (e.g., for temperature, moisture, and presence sensors) and cultural heritage conservation (capillary, continuous, and non-invasive monitoring of the environmental conditions near artworks in museums and galleries). Two possible application scenarios are further detailed hereafter.

Factories of the Future

The introduction of an advanced RFID network able to identify, monitor, and track objects based on eco-compatible technology has the poten-

tial to revolutionize the way of producing, transporting and consuming various goods, and its use is interesting in innumerable applications in several areas of our daily life. Probably the deepest impact will be in the logistics and related areas, which will benefit an increase in productivity, costs and time saving. The achievable high level of precision and the extremely low cost of UWB ecological tags (compared with actual active RTLS) can be exploited with great benefits for logistic. The possibility to apply low cost tags to boxes, pallets, and other objects inside factories, deposits, warehouses, and stores can introduce many advantages. It will also enable to know the spatial and the temporal coordinates of the different components of the manufacturing process. This will increase the potential for efficient logistics and manufacturing. With the “just-in-time” philosophy one will minimize the time components and final products stay in stock. Furthermore, the same tags can prevent robbery because they are also alarm activating. The presence of tag with embedded sensors paves the way to continuous monitoring of perishable goods which require a continuative check of the environmental parameters (e.g., temperature/moisture). Special automated guided vehicles (AGVs), equipped with smart tags and able to move from the manufacturing line to the warehouse, could pick up the right boxes/containers and move them to the right place in the manufacturing line. The AGVs themselves could be guided, without the need of any fixed guidance, using the real-time localization capability so that they would have a high operative flexibility with respect to different working scenes. Assuming that personnel is identifiable and localizable through the same smart tags, active protection against the moving AGVs can be enabled. Fig. 1.2 shows a possible scenario.

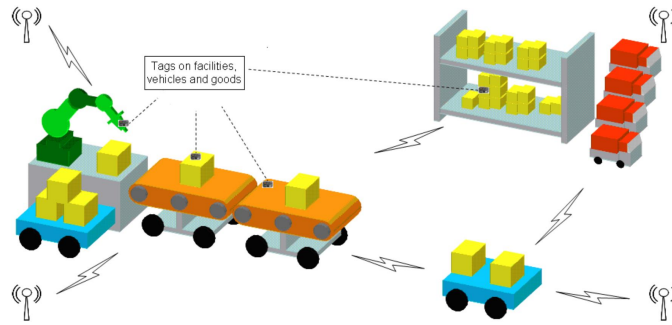


Figure 1.2: Example of GRETA potential application for logistics and industrial production chain.

e-Health: Smart Hospital

In this context the proposed eco-compatible technology lends itself to various applications, able to enhance efficiency management and patients safety in hospitals. As an example, with reference to Fig. 1.3, one could think of single-use “smart band-aid” with an integrated temperature sensor (thermometer) in continuous contact with the skin of the patient. In such a way, when interrogated, the temperature sensor is already at the equilibrium temperature, so the measurement time is only due to the wireless data communication (few ms), and the current drawbacks of mercury or infrared thermometers, such as systematic errors, long measurements duration, use of highly polluting substances, and difficulties in applying to kids patients, will be eliminated. The localization characteristics of the proposed system would finally allow the continuous tracking of drugs and equipment also maintaining a continuous checking on environmental conditions. For example, the tracking and monitoring of blood product fluid bags of human nature from production phase (blood donor) to consumer phase (transfusion in a patient) in order to reduce the risk in the clinical transfusion field. In this contest the main parameter to guarantee the good quality of blood products is the temperature.

1.1. System Architecture

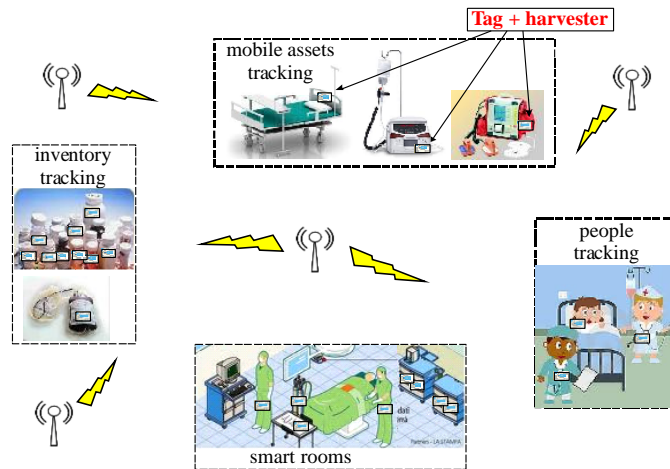


Figure 1.3: Example of GRETA potential application for smart hospital.

1.1 System Architecture

The activity and outcomes contained in this thesis fall within the GRETA project. Specifically, the presented part describes the design of the green tag antenna: an innovative ad hoc antenna suitable for joint UWB-UHF simultaneous backscatter communication and energy harvesting, featuring a flat, low profile and compact size architecture. The design of the RF electronics, integrated in the tag, is also detailed in the thesis. Correct functionalities and dual-band operation simultaneity are guaranteed by a diplexer network. This network provides matching conditions for both operating bandwidths, as well as decoupling between them. To comply with the small required dimensions, the diplexer network is miniaturized. Connection between the antenna and the diplexer is also described in details. Fig. 1.4 shows the GRETA system architecture, where the part subject of this activity is highlighted.

Design details of the various part of the tag are described in the following Sections, together with the corresponding performance. An extensive illustration of the various prototypes realization is given, for intermediates steps on FR-4 and Taconic substrates. Finally, in view of

1.2. Integrated UWB-UHF Antenna

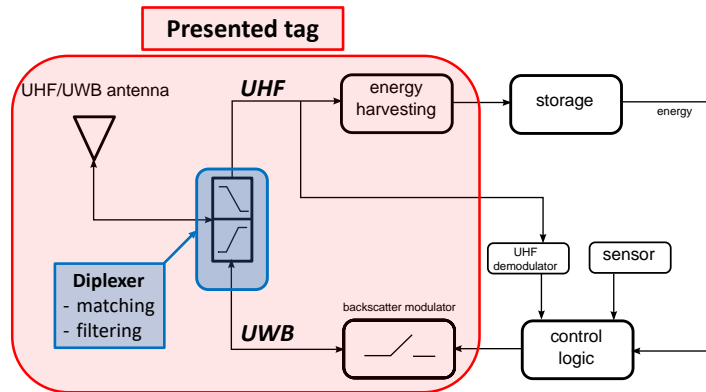


Figure 1.4: Schematic representation of the GRETA tag architecture, where the highlighted area corresponds to the described design activity.

the eco-compatibility requirement, the whole tag is designed and realized on paper substrate. Paper is indeed an excellent candidate to reduce environmental impact of electronic circuits: it is widely available at a very low cost and most of all its highly biodegradability, with respect to other ceramic substrates, allows it to turn into organic matter in landfills in only a few months [56].

1.2 Integrated UWB-UHF Antenna

UWB techniques, in the European lower UWB band from 3.1 to 4.8 GHz, are chosen for the communication and localization functionalities thanks to their interference robustness characteristics, even in indoor scenarios. Moreover, an additional benefit in adopting UWB communication is the ultra-low power consumption, which makes it possible to deploy battery-less RFID sensors by exploiting RF energy harvesting. For energy harvesting purposes, though, UWB technology is not adoptable due to the allowed extremely low-spectral power density [57], which does not make it a good candidate for efficient usage of nonlinear devices, responsible for the RF-to-dc rectification.

1.2. Integrated UWB-UHF Antenna

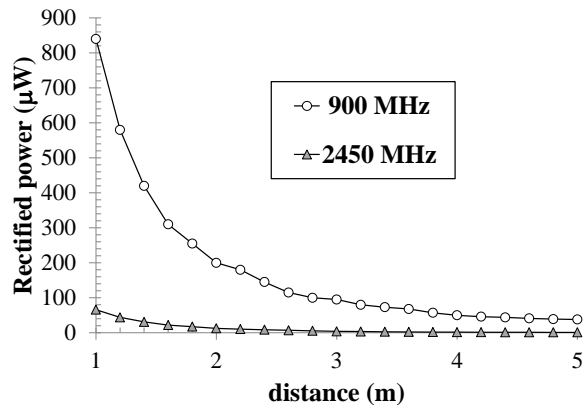


Figure 1.5: Modeled dc output power for two comparable rectennas, operating at 900 and 2450 MHz.

A possible solution, to keep the same radiating element for both communication and energy harvesting, could be the exploitation of the 2.45 GHz ISM band, which is close to the lower limit of the UWB band. However, this would limit the maximum reachable link distances, as clearly shown in Fig. 1.5. This plot compares the rectified power delivered to the optimum load of two rectennas operating at 900 and 2450 MHz, versus the free-space distance from a fixed RF source. In both cases, an effective radiated power (ERP) of 500 mW is employed, incident in the maximum link direction. Both the antennas are connected to the same full-wave rectifier through a suitable matching network [58]. The great advantage in collecting RF energy from the ambient by exploiting the UHF band is clear: roughly one order of magnitude less in terms of rectified power is achieved at 2.45 GHz. Thus, the best solution appears to be the combination of two radiating elements: one designed for energy harvesting purposes in the UHF band and the other one to sustain UWB communication. Moreover, this choice has the great advantage of guaranteeing possible compatibility with previous RFID generations, as strongly recommended by market needs.

Combined UWB-UHF solutions have been recently investigated [59,

1.2. Integrated UWB-UHF Antenna

60, 61, 62], but most of them consist of optimized placement of separate antennas with two different ports: one for UWB communication and the other for UHF communication/harvesting. The presented activity describes the first single-port antenna solution for hybrid UWB-UHF operation. This results in a superior size reduction with respect to previous solutions, at the same time guaranteeing a high quality of the radiation characteristics. Prior to the design of an eco-compatible tag with recyclable materials, a first prototype of the proposed topology is realized on a standard FR-4 substrate to validate design results.

1.2.1 Antenna Design

As in all wideband applications, an almost uniform antenna behavior in the whole frequency band, from the near-field (antenna impedance) and far-field points of view, is an important design requirement, though not always satisfied by the available solutions. Moreover, circular polarization is desirable in RFID applications to reduce tag installation constraints. A large number of wideband antennas are available from literature. The simplest choice is to resort to step-wise [63] or tapered [62, 64, 65] planar monopole topologies, with partial ground plane for image theorem application, or similarly inspired solutions, such as the Vivaldi antenna [65]. Many drawbacks pertain to these antennas: the dispersive behavior in terms of both far- and near-field, the linear polarization of the radiated field, and the unbalanced nature of the port (less suitable to chip connection). The antipodal Vivaldi antenna [66] solves the problem of the unbalanced port, only. For the present design, we exploit the self-complementary architecture [67] which theoretically provides an almost constant port impedance behavior in the whole band (ideal $Z \approx 188.5 \Omega$, practical $Z \approx 120 \Omega$, due to finite met-

1.2. Integrated UWB-UHF Antenna

alization thickness and feed line [67]) and identical radiation properties, as a fixed-shape “active zone” moves along the structure, by varying the operating frequency. Within this family of antennas, some topological choices permit to satisfy the circular polarization constraint, too: as the cases of standard Archimedean [67] and logarithmic spiral [65] topologies, both providing a balanced port, or a tapered version of the Archimedean spiral with unbalanced port [68]. The selected topology for the present design is the Archimedean spiral, providing the minimum size. This choice has been taken by comparison of EM simulations of an Archimedean and a logarithmic spiral antenna printed on a 1.5 mm thick FR-4 substrate ($\epsilon_r = 4.3$, $\tan(\delta) = 0.025$ at 10 GHz), offering a similar behavior.

Optimization of the Archimedean Spiral Antenna

A first coverage of the UWB band, from 3.1 up to 4.8 GHz, is obtained by a 3.2-cm-diameter spiral, with lines width (equal to lines gap for the autocomplementarity principle) of 1 mm. The “active zone” of this antenna is the circular portion of the spiral having a circumference equal to the working wavelength, λ : in this section, an in-phase condition for the currents flowing in the two stripes is reached, thus providing a behavior equivalent to a full-wavelength loop antenna [67]. It is well known that superior performance is achieved by thin-arms spiral antenna: the exploitation of vertical metallic strips (i.e., strips lain on the thin thickness side) allows to have much tighter turns: this way the number of strip turns can be considerably increased and thus a purer spiral behavior can be achieved [69]. A further goal, however, is to accomplish an additional UHF band coverage by means of a unique, compact, planar structure. As a first attempt in this direction, the above-described Archimedean

1.2. Integrated UWB-UHF Antenna

spiral can be used by simply increasing its dimension; however, this solution requires a spiral diameter of almost 13 cm to reach good radiation properties at the desired frequency, thus obtaining a total area incompatible with almost all RFID applications. This result clearly points out the necessity to investigate ad hoc solutions to obtain the demanded goal within suitable overall dimensions. Antenna miniaturization has always been of great interest in both commercial and military applications, therefore several techniques and guidelines have been proposed in literature [70, 71]. A possible solution would be that of using high dielectric constants [72] or even magneto-dielectric [73] materials, but the final aim of realizing an eco-friendly device forces to discard these possibilities. Hence, a different miniaturization solution is investigated, the so-called “gap-loading” technique [74]: the inclusion of a capacitive load (a 1-mm-circular stripe, placed 1-mm-far from the spiral) increases the electrical length of the structure, thus reducing its overall dimension. However, the almost 23% reduction factor reached is not yet enough for the desired purpose.

Novel UWB-UHF Antennas Hybrid Topology

A new solution for co-localizing a UWB and a UHF antenna sharing the same substrate and the same port can be obtained by extending the spiral length to form a meandered dipole. In Fig. 1.6, the principle of the presented idea is shown. The new topology justifies, from another point-of-view, the choice of the Archimedean spiral, instead of the logarithmic one: the fusion of the spiral with the dipole can be straightforwardly obtained without any tapering in between the two structures. It is worth noting that all the spiral paths contribute to the dipole antenna, thus allowing an overall dipole length suitable for UHF band applications. It

1.2. Integrated UWB-UHF Antenna

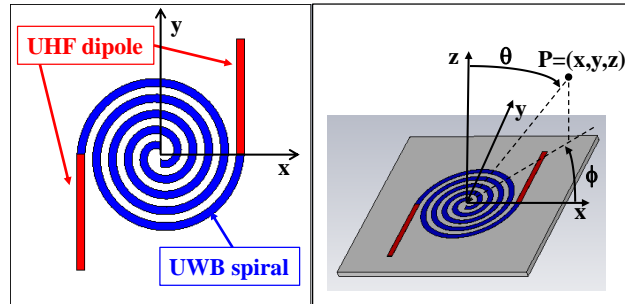


Figure 1.6: Integrated UWB-UHF one-port antenna architecture.

must be stressed that the UHF dipole still offers linear polarization, as standard straight dipoles: in fact, the far-field polarization is determined by the vertical arms departing from the spiral, while the rest of the branches mainly contribute as reactive loads. Linear polarization of the UHF antenna is required by the wireless powering mechanism foreseen in the National Project for which this antenna has been developed [50]: this is based on a set of intentional, linearly polarized UHF sources cleverly deployed in the ambient to provide the RF power on demand (“energy showers”), compliant with the maximum EIRP emission in the European UHF 868 MHz RFID band [75]. Conversely, circular polarization for the UWB antenna is chosen for communication/ranging purposes, as usually required in most RFID applications.

To preserve the autocomplementarity of the spiral and to minimize lines coupling in the long path providing the dipole operation, wider lines with respect to previous experiments are chosen: lines and gaps width is set to 1.5 mm. This value has been chosen as a good compromise to guarantee the best spiral and dipole coexistence. Indeed this width leads to a total UHF dipole length of a $1.5\text{-}\lambda$ UHF dipole, while preserving a compact layout. Conversely, reduced width size better ensures the spiral currents in-phase condition [69] (with the number of turns increased accordingly, to preserve the outer circumference dimension). However,

1.2. Integrated UWB-UHF Antenna

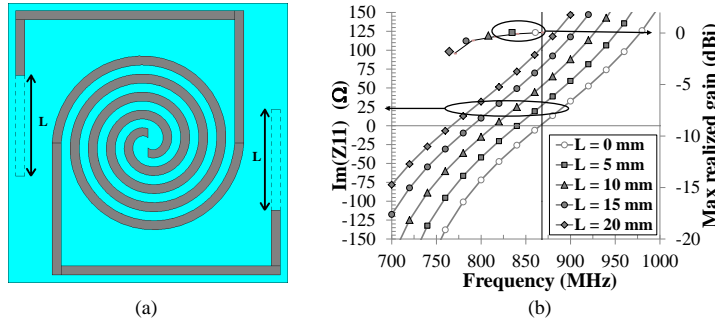


Figure 1.7: (a) Final topology of the proposed antenna. (b) Reactance and maximum realized gain as a function of the length of the dipole.

this choice directly lengthens the UWB spiral arms and forces the use of a $2.5\text{-}\lambda$ UHF dipole, as the whole spiral path contributes to the dipole antenna. By EM simulation [76], it is proved that this configuration worsens dipole performance, as most of its length comes from the spiral path. As a consequence, its polarization is turned from perfectly linear to elliptical. Moreover, longer and thinner paths involve higher losses, which would be a critical aspect in view of an ultra-low power, eco-compatible realization on recyclable substrate. Finally, a standard $0.5\text{-}\lambda$ dipole cannot be adopted as well, as it would require an excessive reduction of the number of turns at the expense of the spiral performance, especially in the lower UWB frequency range.

The final topology of the antenna is reported in Fig. 1.7(a). The folded dipole layout guarantees a resonant behavior at 868 MHz (imaginary part of the dipole impedance equal to zero). However, if the antenna is used with a standard UHF-RFID chip (for compatibility purposes with previous generations), an easy conjugate matching can be obtained by varying the final part of the dipole length (L) of Fig. 1.7(a). This is clearly shown in Fig. 1.7(b), where the imaginary part of the dipole input impedance is plotted versus frequency, with L as a parameter. It can be observed that a 20-mm length variation provides a $100\ \Omega$

1.2. Integrated UWB-UHF Antenna

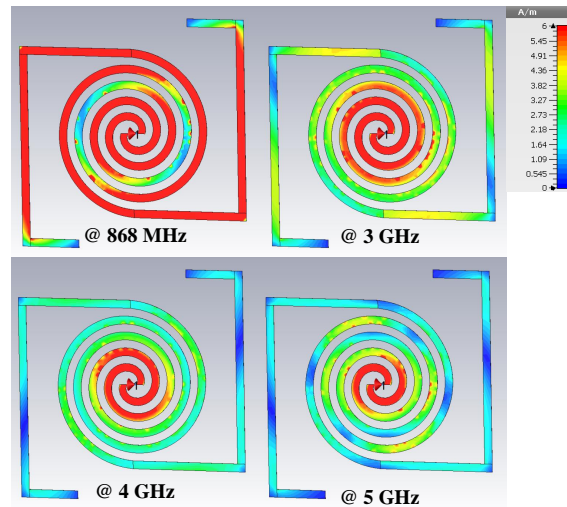


Figure 1.8: Full-wave simulation results in terms of surface current magnitude in the UHF and UWB bands.

reactance span. From Fig. 1.7(b), it is also clear that, for any selected length value, the reactance slope with respect to frequency does not vary significantly. This allows us to conclude that the operating UHF-RFID bandwidth (conjugate matching conditions) can be guaranteed for many different dipole lengths. In Fig. 1.7(b), the corresponding realized gain, in resonant conditions, is also plotted: its almost flat behavior confirms that, by varying the branch L of the total dipole length, the radiation properties in the UHF band are not significantly degraded. Thus, these tuning properties can be potentially exploited for compatibility with standard RFID chips.

The first demonstration of the effectiveness of the presented idea is reported in Fig. 1.8, where the surface current magnitude, computed by full-wave simulation in correspondence to the operating frequencies, is assessed. Besides the shift of the active zone within the UWB band, the 1.5λ behavior in the UHF band can be noticed, too: indeed two zero current values for each branch are evident. A further confirmation of the optimal coexistence of the two antennas is then provided by the highly

1.2. Integrated UWB-UHF Antenna

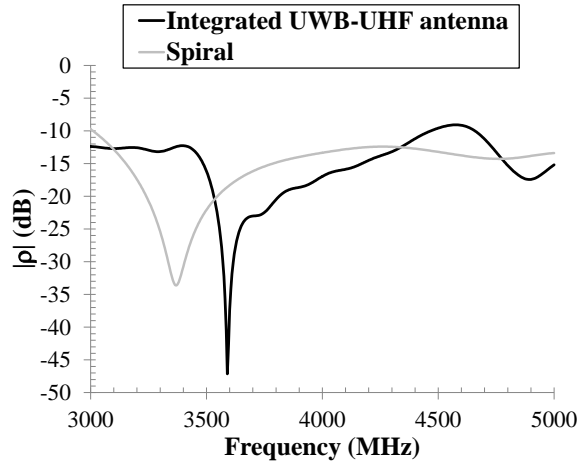


Figure 1.9: Antenna performance in terms of reflection coefficient, without dipole (gray line) and with dipole (black line).

similar spiral performance with and without the dipole. In Fig. 1.9, the reflection coefficient (normalized to 120Ω) is shown: a maximal value of -10 dB is guaranteed for the two configurations in the frequency band of interest. In Fig. 1.10, the plots of the radiation patterns in the yz -plane (see Fig. 1.6) at the UWB center-frequency are compared, showing an excellent agreement. The same is true for the antenna circular polarization properties: in Fig. 1.11, the axial ratio (AR) in the xz - and yz -planes of the UWB antennas is compared: a maximum difference of 1.5 dB is predicted in both planes. Similar results have been obtained all over the $3 - 5$ GHz band, thus ensuring the proper UWB communication in the presence of the UHF dipole. Previous results also justify the insensitivity of the UWB antenna near- and far-field properties to dipole length variation, as verified by EM simulation.

1.2.2 Antenna Experimental Characterization

For a first, extended characterization of the new UWB-UHF integrated antenna, the first prototype is realized on FR-4 substrate. The photo of the prototype with the associated dimensions is shown in Fig. 1.12(a).

1.2. Integrated UWB-UHF Antenna

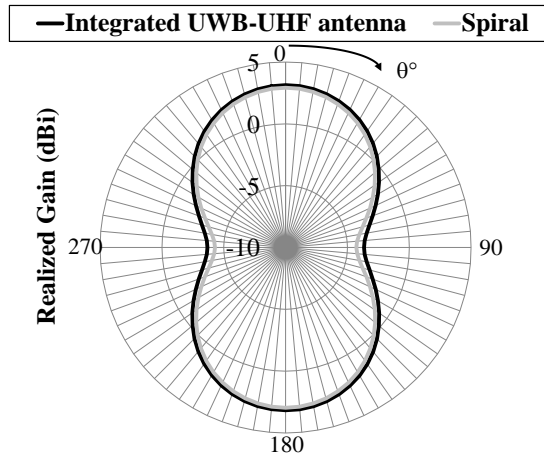


Figure 1.10: Antenna performance in terms of realized gain in the yz-plane at the central UWB band frequency of 4 GHz, without dipole (gray line) and with dipole (black line).

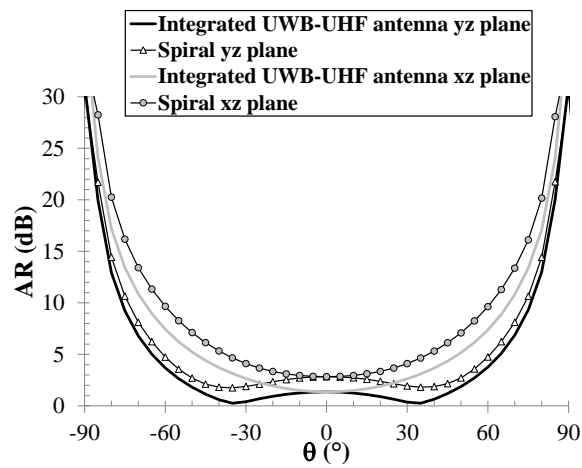


Figure 1.11: Antenna simulated axial ratio at the central UWB band frequency of 4 GHz, with and without dipole, in the yz- and xz-plane.

1.2. Integrated UWB-UHF Antenna

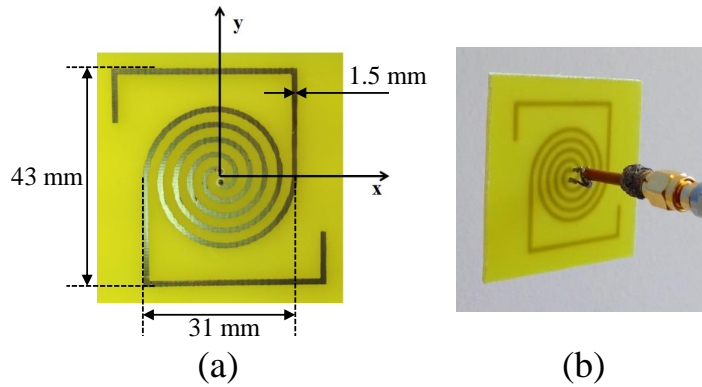


Figure 1.12: Photo of the FR-4-based prototype: (a) front view and (b) perspective view with the coaxial cable used in radiation pattern measurements.

As regards antenna port measurements, the interface between the unbalanced measurement equipment and the balanced nature of the antenna port has to be considered. A possible approach can be resorting to the measurement procedure proposed in [77], where a Y-shaped three-ports coaxial junction is used. After applying the cable de-embedding procedure, an excellent correspondence between measured and modeled antenna impedance is obtained, shown in Fig. 1.13, spanning both the UHF and UWB bands. From inspection of the figure, the exact resonance at 868 MHz, and the almost constant behavior in the UWB band can be easily evinced; the third zero-crossing of the reactance in the lower band clearly confirms that the total length of the dipole provides a 1.5λ behavior. It can be observed that in the UHF band, the integrated antenna shows an impedance real part of about 12Ω , which is acceptable for efficient matching to an RF-to-dc rectifier. These results also show that the real part of the impedance is of only few Ω in correspondence of the first zero-crossing of the reactance, which further confirms that a common half-wavelength topology would not be convenient due to its extremely low resistance values.

1.2. Integrated UWB-UHF Antenna

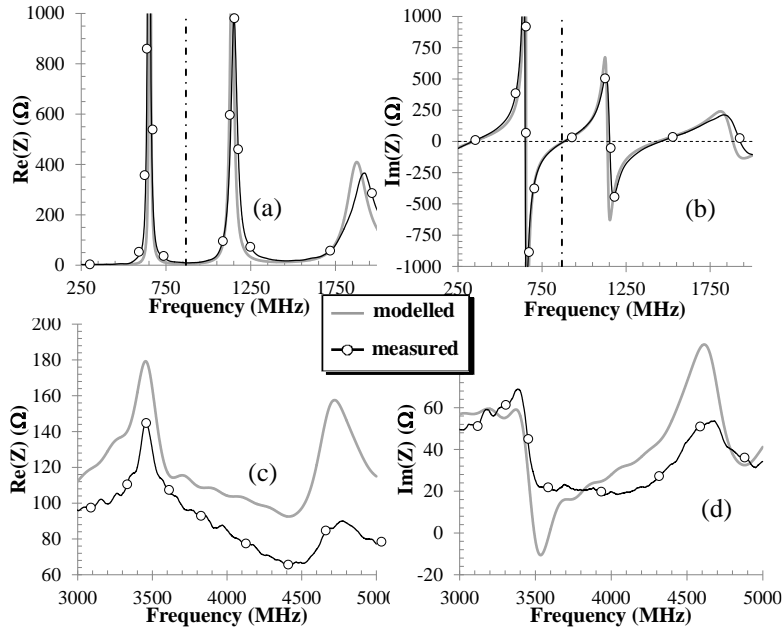


Figure 1.13: Measured and modeled antenna input impedance: (a) real part; (b) imaginary part in the UHF band; (c) real part; and (d) imaginary part in the UWB band.

Very good agreement can also be observed by comparison of the modeled and measured reflection coefficients in both the UHF and UWB bands, by resorting to the proper normalization, as shown in Figs. 1.14 and 1.15, respectively.

Antenna far-field measurements are carried out in a real-office scenario, and not in an anechoic chamber, to test the antenna performance in practical applications. As we look for normalized behavior of the radiation properties, direct connection of the conductors of a $50\text{-}\Omega$ coaxial cable [78, 79] to the antenna differential port is adopted in this case. In Fig. 1.16, the predicted and measured radiation patterns of the co-polarized and cross-polarized components in the E and H-plane (yz- and xz-plane, respectively) of the UWB-UHF antenna at 868 MHz are reported. As can be evinced, they prove to be almost identical to those obtained by a standard straight standalone dipole. The unique differ-

1.2. Integrated UWB-UHF Antenna

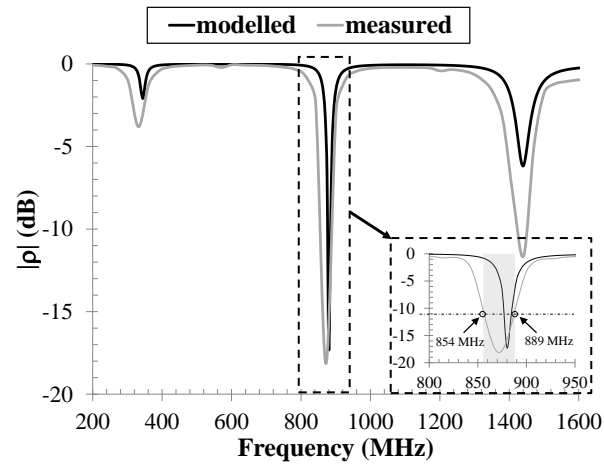


Figure 1.14: Measured and modeled reflection coefficient in the UHF band (normalized to 12Ω). $0.5\text{-}\lambda$, $1.5\text{-}\lambda$, and $2.5\text{-}\lambda$ resonances can also be recognized.

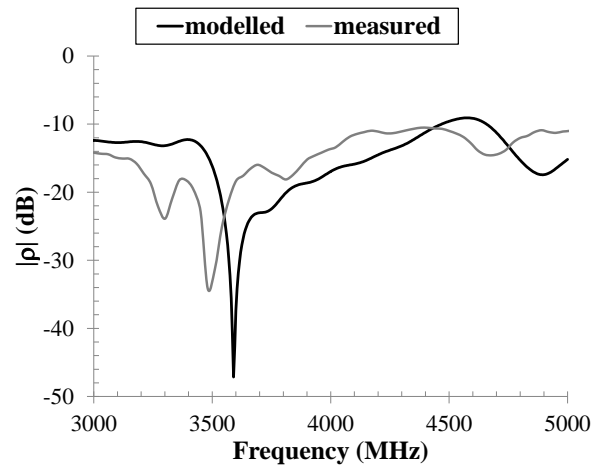


Figure 1.15: Measured and modeled reflection coefficient in the UWB band (normalized to 120Ω).

1.2. Integrated UWB-UHF Antenna

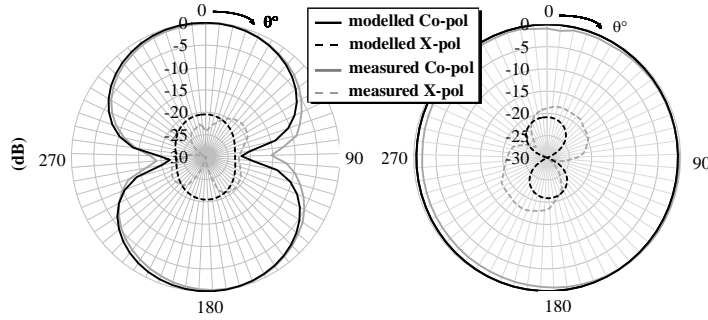


Figure 1.16: Measured and modeled normalized field radiation patterns of the co- and cross-polarized component at 868 MHz, in the (a) E-plane (yz) and (b) H-plane (xz) of the dipole.

ence with respect to a straight dipole is the absence of secondary lobes, despite the geometrical 1.5λ length, as most of its total length is arranged in a spiral-like configuration. As regards, the polarization of the dipole far-field, it results linearly polarized in the y -direction (main axis of the dipole) for a wide elevation range. The slight asymmetry of the radiation patterns of Fig. 1.16 is due to the coaxial cable termination shown in Fig. 1.12(b), which is taken into account in the simulation, too.

Similar conclusions can be drawn in the UWB band: Fig. 1.17 reports the simulated and measured radiation patterns at the UWB-band frequencies 3, 4, and 5 GHz, for both the co- and the cross-polarized components. Due to the ungrounded antenna structure, in the $z > 0$ half-space, the co-polarized component is the right-handed circularly polarized (RHCP) one, while in the $z < 0$ half-space (light gray area in the figure), the co-polarized component is the left-handed circularly polarized (LHCP) one. The coaxial cable junction in the back of the antenna is the main reason of a non-negligible cross-polarized component, as verified by simulation, too, and consequently of an AR worsening with respect to the isolated antenna results of Fig. 1.11. The simulated realized gain in the maximal radiation direction of the antenna is

1.2. Integrated UWB-UHF Antenna

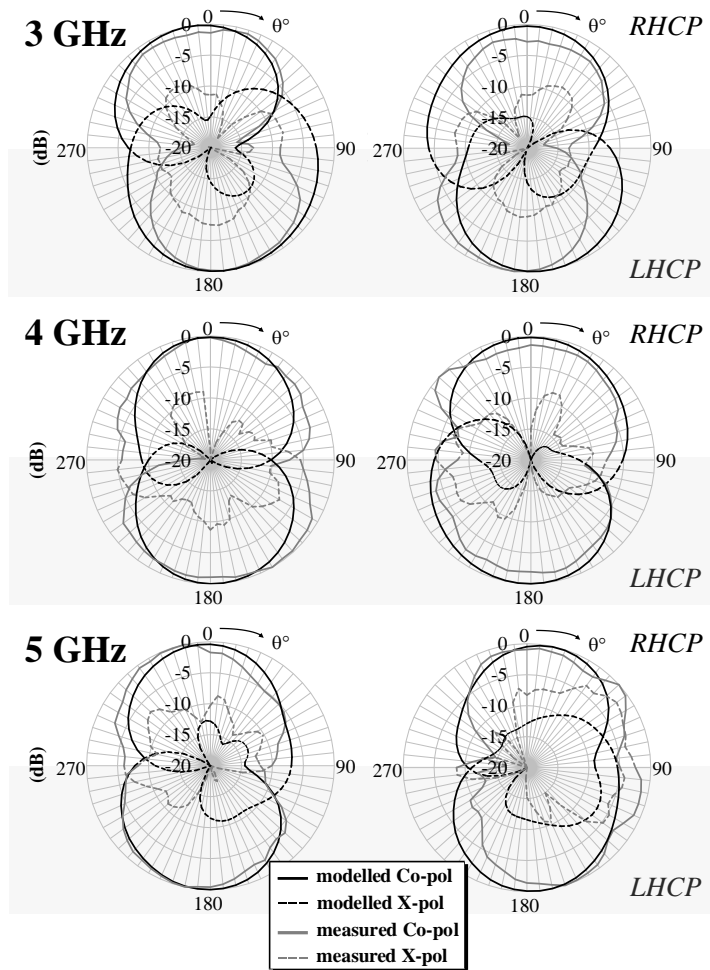


Figure 1.17: Measured and modeled normalized field radiation patterns at 3, 4, and 5 GHz, in the yz -plane (left column), and in the xz -plane (right column).

plotted in Fig. 1.18, in both the operating frequency bands: an almost constant behavior is obtained in the UWB band, as expected; a value of more than 0 dBi is guaranteed in the UHF band. In the same figure, the measured gain is superimposed, too: good agreement with modeled results is achieved. These results were obtained using a 12- and 120- Ω termination, for the UHF and the UWB bands, respectively.

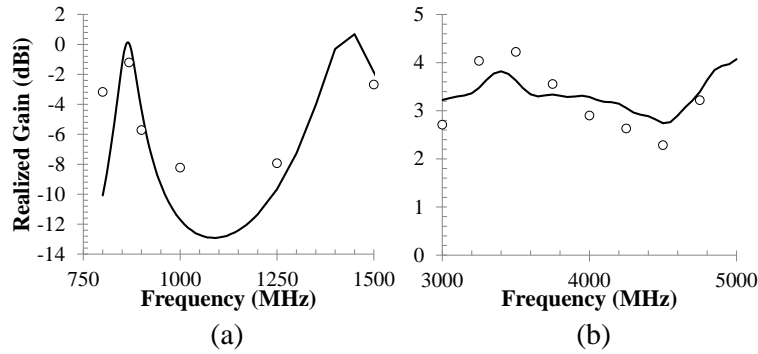


Figure 1.18: Simulated (solid line) and measured (markers) realized gain of the FR4-prototype in the (a) UHF band and (b) UWB band.

1.3 Diplexer Network

The co-localization of the two radiating elements leads to a single-port antenna architecture. This situation can be remarkably advantageous for the direct connection of a single chip, located in the center part of the antenna, which embeds the whole tag circuitry. For a hybrid prototype realization, though, a proper three-way matching network needs to be accurately designed. This network, or diplexer, is a three-port microstrip/lumped element antenna-feeding network able to simultaneously provide high decoupling between the UHF and the UWB paths as well as their respective matching conditions. In particular, the diplexer is designed to connect the antenna (port 1) to a rectifier for the UHF path (port 2), and a UWB modulator for the UWB path (port 3). This simultaneously guarantees decoupling and matching conditions for both the UHF and the UWB paths, by means of a lumped elements filter in the UHF band, and a microstrip filter in the UWB band. The challenging aspect is to reach these goals with reduced dimensions in order not to affect the antenna performance. In view of a unique UWB-UHF chip realization, the diplexer network can be used as a proof-of-concept to be integrated in a unique chip. Different aspects need to be simultaneously

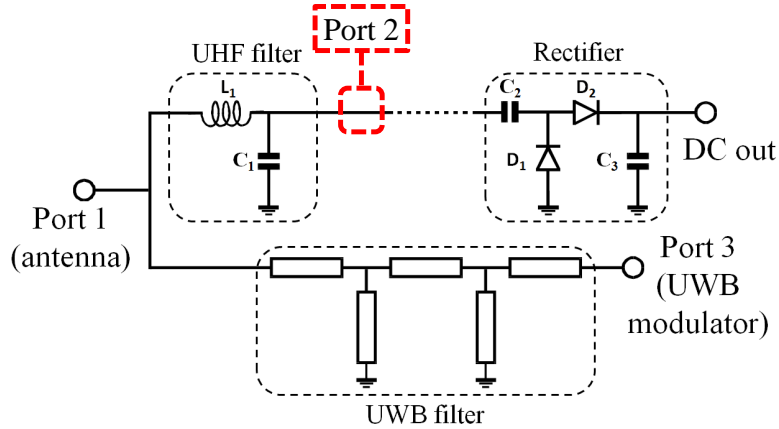


Figure 1.19: Schematic of the diplexer circuit topology. Port 2 is an artificial termination introduced for evaluation of the diplexer performance.

accounted for in this feeding network design, namely:

1. preserving the radiating performance of the ungrounded antenna;
2. realizing a suitable transition from the antenna balanced port to the unbalanced microstrip network;
3. separating and matching the UHF and UWB paths with minimum insertion losses.

Fig. 1.19 illustrates the diplexer topology. In the UHF band, the diplexer is responsible for filtering the signal as well as providing matching condition towards the following rectifier, which converts the RF incoming signal into dc output power. This filter is realized with lumped SMD components. For the rectifying section a full-wave voltage-doubler topology, exploiting Schottky diodes SMS7630-079LF from Skyworks [80], has been adopted. As regards the UWB band, the communication capabilities are provided by the exploitation of passive backscattering; therefore the UWB port of the diplexer will be connected to a backscatter modulator, which will be responsible for the modulation of the incoming signal by switching its impedance between the two mis-

1.3. Diplexer Network

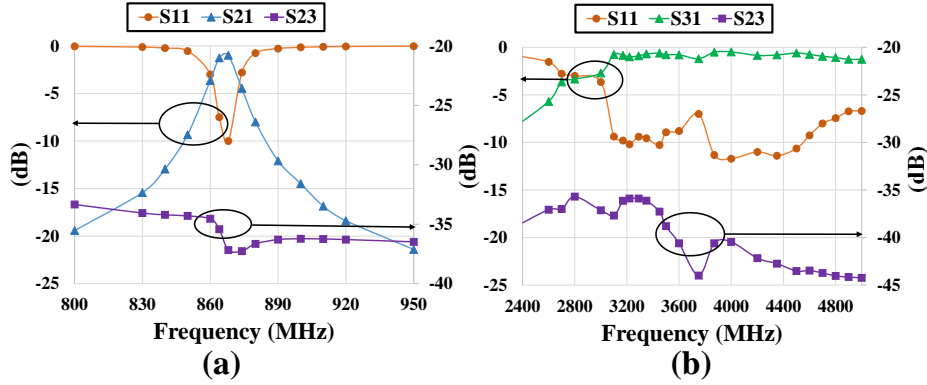


Figure 1.20: Simulated scattering parameters of the three-port network of Fig. 1.19 in the (a) UHF band and (b) UWB band.

matched conditions of open and short circuit terminations. For design purposes, the UWB path of the diplexer has been matched to a 50Ω termination; nevertheless a similar design procedure can be successfully followed for any other loading conditions. The UWB path is realized with a distributed element filter, composed by a microstrip line featuring two short-circuited stubs.

Nonlinear/electromagnetic co-simulation [81] is then adopted to optimize the network for the stringent design goals described earlier. In order to test the feasibility of the diplexer performance in view of an eco-compatible substrate realization, the network is designed on a 0.69 mm thick paper substrate ($\epsilon_r = 2.85$, $\tan(\delta) = 0.053$ at 4 GHz). The simulated three-port circuit behavior is reported in Fig. 1.20, in terms of scattering-parameter amplitudes: in this case, a complex impedance of $20 - j250 \Omega$ is used as the UHF port impedance (port 2 of Fig. 1.19). This constant value has to be understood as the mean-value of the variable nonlinear rectifier input impedance at the expected low input power levels (from -20 to 0 dBm). For the present purpose, the UWB port (port 3 of Fig. 1.19) has been kept referenced to 50Ω . The S21 and S31 plots show promising values of the transmission coefficients between the

1.4. Taconic Implementation

antenna port and the UHF and UWB ports, respectively: they are equal or greater than -2 dB in both cases and all over the bands of interests, in spite of the high paper losses.

The effectiveness of the designed network is also confirmed by the high decoupling between the UHF and the UWB ports all over the bands [see S23 in Figs. 1.20(a) and (b)]. Indeed, in order to successfully provide the demanded functionalities during all tag's operating conditions, the highest decoupling behavior between the UHF and the UWB frequency bands is mandatory. For this reason a further inspection of the diplexer performance under different operating circumstances has been conducted. During the UWB backscattering communication, the UWB modulator switches its impedance from an open circuit to a short circuit condition: these extremely different loads values could affect UHF behavior too, if not properly decoupled. Fig. 1.21 shows UHF filtering and matching performance for all the UWB different operating conditions; this result clearly shows how the high decoupling provided between the two operating bands guarantees a correct UHF operation. On the other side, rectifying operation in the UHF band could affect the UWB communication, especially because of the nonlinearity introduced by the rectifying section. For this purpose the insertion loss introduced by the UWB microstrip path is evaluated for different levels of the incoming RF signal incident in the UHF band, as depicted in Fig. 1.22. Once again, high decoupling proves to be guaranteed, allowing completely transparent operations between the two operating bands.

1.4 Taconic Implementation

Thanks to the promising results obtained with the first evaluations of both the UWB-UHF antenna and the diplexer network, a complete tag

1.4. Taconic Implementation

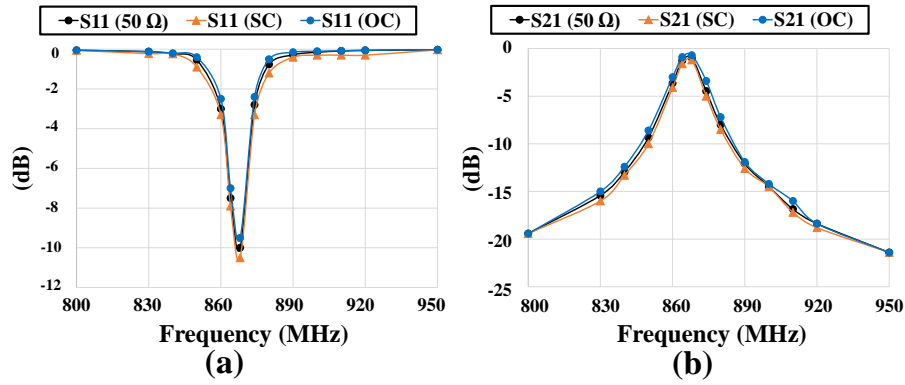


Figure 1.21: Diplexer UHF (a) matching and (b) filtering performance distortion during the UWB modulation (SC - Short Circuit, OC - Open Circuit).

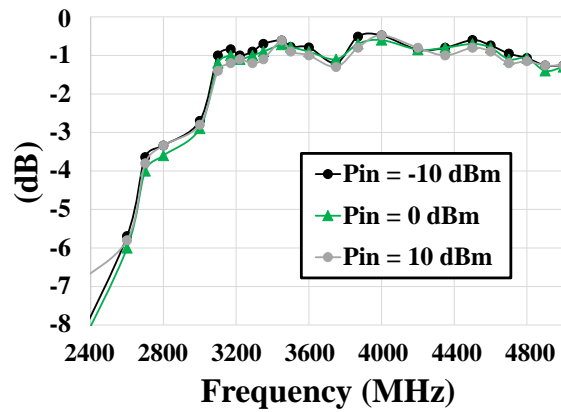


Figure 1.22: Filter insertion loss in the UWB band for different incident UHF power levels.

1.4. Taconic Implementation

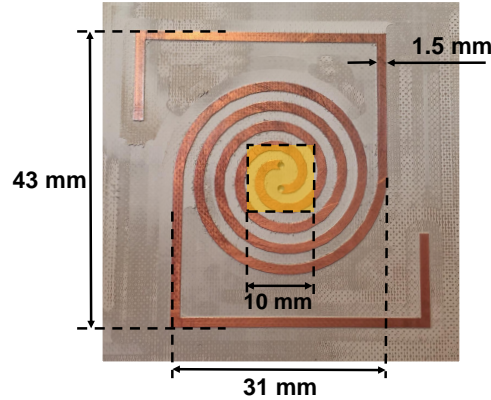


Figure 1.23: Photo of the Taconic-based prototype with the corresponding dimensions. The highlighted part in the center part of the antenna represents the diplexer area on the backside of the tag.

has been designed and realized on Taconic substrate.

First, the integrated UWB-UHF antenna presented in Section 1.2 is designed over a 0.635-mm-thick Taconic RF60A substrate ($\epsilon_r = 6.15$, $\tan(\delta) = 0.0028$ at 10 GHz). A picture of the prototype, realized with an in-house milling machine, is provided in Fig. 1.23, along with the corresponding dimensions. Electromagnetic simulation results exhibit very good radiating characteristics, similar to those obtained with the FR-4 realization. In the UWB band the antenna impedance has an almost constant value of 120Ω throughout the whole band, while radiation efficiency and realized gain are approximately equal to 95% and 3.5 dBi, respectively. In the UHF band the $1.5\text{-}\lambda$ meandered dipole shows a purely real impedance of approximately 5Ω at 868 MHz. The radiation efficiency is in this case of 82%, with a realized gain of 0 dBi.

As previously discussed, the significant dispersive behavior of the presented antenna needs a proper matching network in order to work correctly. The diplexer network, whose topology has been introduced in Fig. 1.19, is responsible for both matching and filtering of the UHF and UWB bands, as well as decoupling between the two. Since the

1.4. Taconic Implementation

adopted UWB-UHF antenna has no ground plane, its radiation pattern is bi-directional, being equally distributed in both the $z > 0$ and the $z < 0$ half-spaces, for the two operating bands. This means that the presence of nearby circuitry metalization can highly deteriorate antenna performance. Hence, for a practical implementation of the tag, several diplexer topologies have been investigated, focusing on preserving the radiating properties of the antenna while at the same time ensuring a low-profile structure. This means that, as anticipated, the diplexer has to be implemented with reduced dimensions.

Given these constraints, a 1-cm^2 microstrip/lumped elements diplexer has been designed on a 0.635 mm-thick Taconic RF-60A substrate, which runs parallel to the antenna substrate. The area of the diplexer network and its placement on the backside of the integrated UWB-UHF antenna can be observed in Fig. 1.23. Increasing circuit dimensions would lead to a degradation of the ungrounded antenna performance, especially for the higher frequencies of the UWB band: for this reason a miniaturization of the diplexer circuit is mandatory.

1.4.1 Antenna-Diplexer Connection

As anticipated, a future single chip realization, providing all the functionalities of the described diplexer, and directly connected to the balanced single port presented antenna, would lead to a very compact device. As a first hybrid implementation, though, the described diplexer has to be exploited, and because of the ungrounded nature of the antenna, its placement and connection need accurate consideration. Indeed, the presence of a metallic plane on the backside of the spiral antenna would strongly influence its radiation characteristics. This degradation would arise for increased diplexer dimensions, especially at the

1.4. Taconic Implementation

higher frequencies, involving the inner part of the spiral. The implementation of a 1-cm^2 circuit, at a distance of 5 mm from the antenna, proves to be a good compromise, influencing antenna behavior only marginally, in terms of both radiation patterns and polarization, all over the frequency bands of interest.

The single port antenna presents balanced feeding lines, therefore the connection with the unbalanced microstrip/lumped elements diplexer will have to take this transition into account. For this purpose a 5 mm-long balanced line departing from the center of the spiral arms is built over the same 0.635 mm-thick Taconic RF-60A substrate and is placed orthogonally to the antenna and diplexer substrate, connecting the radiating element and the matching/feeding network in a balun-free transition [82, 83]. This connection is shown in Fig. 1.24 where the antenna structure has been made transparent for clarification purpose; the diplexer ground plane removal is also visible, allowing one conductor of the balanced line to reach the “hot” microstrip line on the top layer of the diplexer. Two holes have been realized in order to wedge in the balanced line substrate, one on the diplexer substrate and the other one on the antenna substrate; extra Taconic sidewalls have also been added for support purpose.

1.4.2 Diplexer Layout and Performance

The layout of the implemented diplexer is shown in Fig. 1.25. It is mainly composed of three sections: the microstrip UWB matching and filtering circuit, the lumped elements UHF matching and filtering circuit (L1 and C1), and the rectifying section. In order to realize the requested topology on a 1-cm^2 area, the 32.3 mm-long microstrip line composing the UWB path has been meandered. As regards the UHF path and

1.4. Taconic Implementation

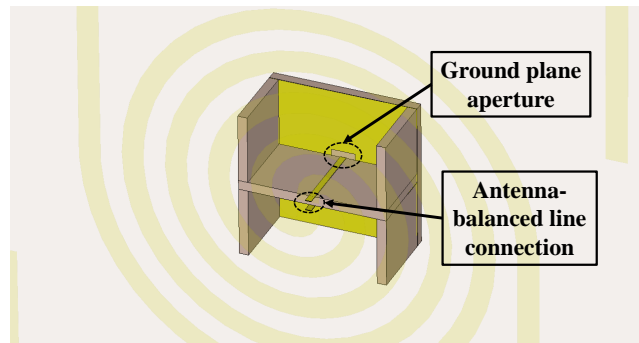


Figure 1.24: Representation of the antenna-diplexer connection. A removal in the diplexer ground plane allows one of the two balanced lines to reach the diplexer top layer.

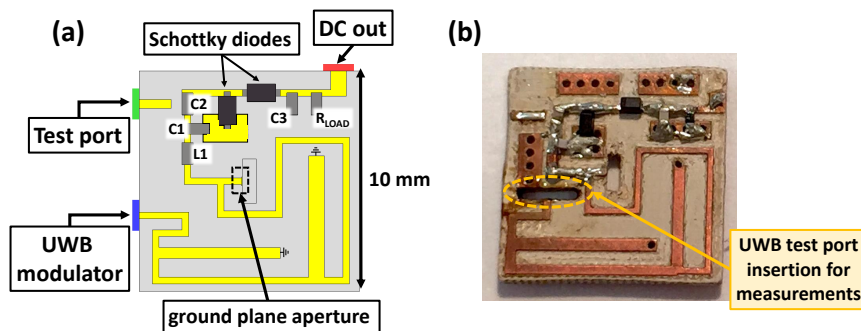


Figure 1.25: Diplexer (a) layout representation and (b) photo of the realized prototype. With reference to Fig. 1.19, the ground plane aperture corresponds to port 1, which connects to the antenna, test port corresponds to port 2 and UWB modulator/test port corresponds to port 3.

the rectifying section, the UHF filter is merely composed of a series inductance $L1$ and a parallel capacitance $C1$. Two Skyworks Schottky diodes are employed in the rectifier in a voltage-doubler topology, after which an optimum load of $6.5\text{ k}\Omega$ has been used. The aforementioned parts are all commercially-available components, of which the models employed are listed in Table 1.1. The SMD components are chosen with 0402 case, to comply with the miniaturization needs.

The UWB communication takes place with passive backscattering of the signal received by the UWB reader. To do so the diplexer is loaded with a UWB backscatter modulator, which basically consists of a vari-

1.4. Taconic Implementation

Table 1.1: List of SMD components of the diplexer Taconic implementation.

Part name	Manufacturer	Product code	Value
L1	Coilcraft	0402HP-15NXGLU	15 nH
C1	Murata	GRM0225C1C1R5CD05D	1.5 pF
C2-C3	ATC	600L100FT200T	10 pF
D1-D2	Skyworks	SMS7630-079LF	
R_{LOAD}	Vishay	CRCW04026K49FKED	6.5 k Ω

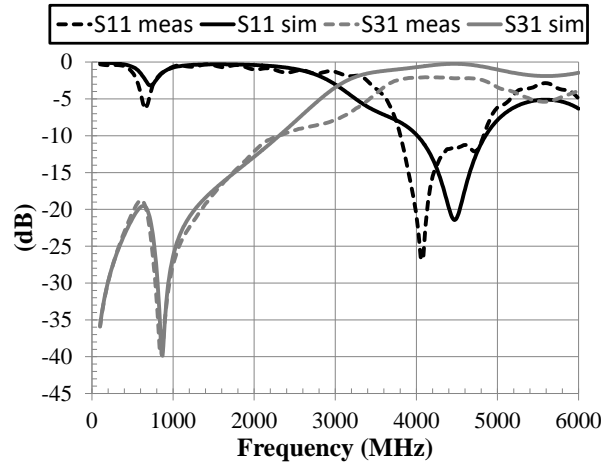


Figure 1.26: Comparison between the measured and simulated reflection and transmission coefficient at ports 1 and 3 of the Taconic diplexer. Both ports are normalized on 50 Ω .

able impedance switching its value from OC to SC conditions. In order to assess the diplexer performance in the UWB band, the scattering parameters at ports 1 and 3 are measured with a vector network analyzer (VNA). The comparison between modeled and measured results is given in Fig. 1.26. Despite an increased loss of 2-3 dB and a slight shrinkage in the operating bandwidth, acceptable agreement is obtained. It is worth noting that the simulated results are reported with a 50 Ω normalization at both ports, to match with the measured one.

One of the requested tag functionalities is the simultaneous recovery

1.4. Taconic Implementation

of RF energy while communicating in the UWB band. A non-linear/electromagnetic co-simulation of the whole circuit has been carried out, including real component models, taking into account the dispersive behavior of the antenna, with the goal of maximizing the RF-to-DC conversion efficiency. Since RF energy harvesting has to deal with typically low-levels of incoming signals, the optimization has been mainly focused on incoming available RF power ranging from -15 to -5 dBm. The resulted modeled conversion efficiency, in optimum loading conditions, is shown in Fig. 1.27 for this range of available RF input power: promising values from 30 to 55% are clearly observed.

In the same plot the measured data are also provided. In this case a serious efficiency drop is reported by the experimental validation. Such inconsistency might be attributed to different phenomena, namely: inaccurate modeling of the 3D antenna-diplexer transition, discrepancy between components model and their real behavior, or incongruous substrate dielectric properties. After thorough examination of the issue, by means of reverse engineering and consequent successive prototyping phases, it was found that this discrepancy could be mainly attributed to the inaccurate nonlinear model of the Schottky diodes adopted for the nonlinear circuit simulations. Furthermore, this inaccuracy was also proved by a following research activity, intensively described in Chapter 2, where a new SPICE model of the Schottky diode, different from the one given by the manufacturer, was generated to finally match the nonlinear behavior of the component.

Finally, Fig. 1.28 reports few pictures of the complete tag realized with the Taconic substrate, where the extra supporting Taconic displayed in Fig. 1.24 was temporarily removed for ease of visualization. On the leftmost side of the image it is possible to see how one of the

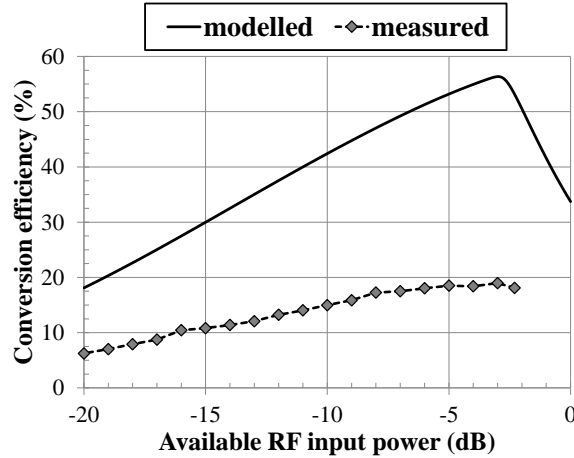


Figure 1.27: RF-to-dc conversion efficiency for low levels of RF incoming available power. Inconsistent measured results are a consequence of the inaccurate manufacturer model of the Schottky diodes.

two balanced lines is modified at one end for connection to the diplexer ground plane, in a balun-free transition. Whereas the rightmost part shows the further 3D transition for insertion of the UWB port used during the measurements, which has then to be replaced with the UWB backscatter modulator.

1.5 Paper Implementation

In this Section the final implementation of the eco-compatible integrated UWB-UHF tag is described. To fulfill the “green electronics” requirement the whole tag is designed and fabricated on paper. The tag fabrication, realized by the University of Perugia, partner of the GRETA project, is based on conventional copper layer to be glued onto paper sheets, which provides a possible alternative to the well-demonstrated inkjet printing technology [84, 56, 85, 86, 87, 88]. Moreover, the proposed low-profile paper layout guarantees eco-compatibility for more than 93% of the total tag volume.

Since low-profile characteristics play a significant role as key enabler

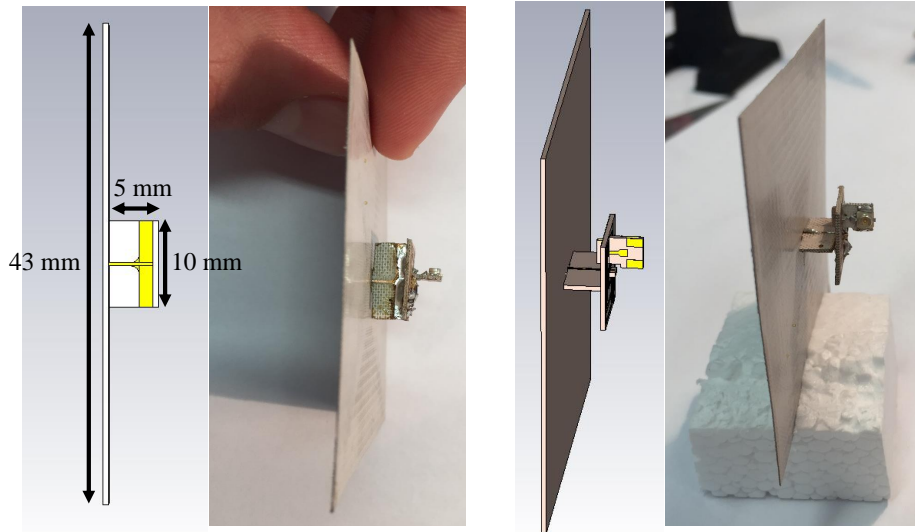


Figure 1.28: Pictures of the complete tag realized on Taconic substrate.

for a large number of applications, with respect to the architecture presented in Section 1.4, a new, more compact and mechanically stable solution has been designed, allowing a total thickness of less than 1 mm. To do so, the multilayer structure, shown in Fig. 1.29(a), is adopted, with the goal of settling the low-profile and robustness requirements with the lowest influence on antenna performance. Two paper sheets, $370\ \mu\text{m}$ -thick, are used as the substrate for the antenna metalization on the top and for the diplexer circuitry on the bottom, whose ground plane is provided by inserting a $13.2 \times 13.2\ \text{mm}^2$ flexible copper sheet, 0.3 mm-thick, between the two paper layers.

Antenna-diplexer connection is realized by means of two via-through connecting one antenna arm to the diplexer ground plane, and the other one to its input microstrip line. This way an effective balun-free transition between the unbalanced diplexer topology and the balanced antenna port is realized. Fig. 1.29(b) shows a 3-D zoom of this connection, where a squared slot of $2.2 \times 2.2\ \text{mm}^2$ in the ground plane allows one arm of the antenna to be connected to the microstrip. This solution does have

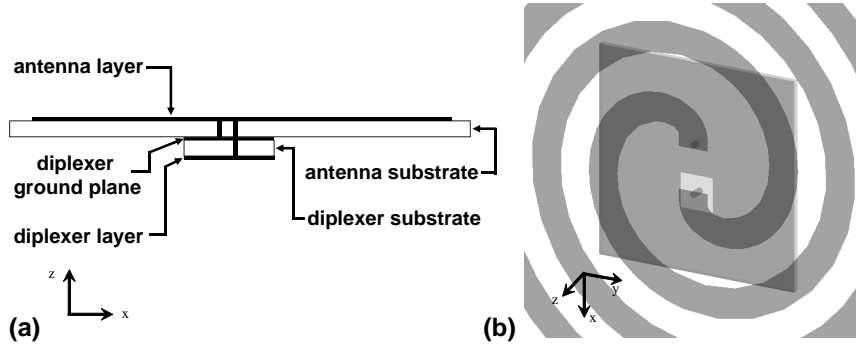


Figure 1.29: Tag architecture: (a) side multilayer view and (b) zoomed perspective 3-D view, where the multiple layers are made transparent for ease of visualization.

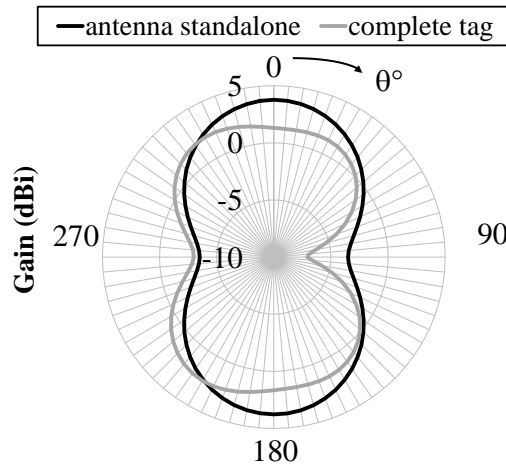


Figure 1.30: Comparison between modeled gain patterns of the standalone antenna and the antenna with the back side diplexer at the UWB central frequency (4 GHz).

a negligible impact on the antenna radiation behavior as shown in Fig. 1.30, where the antenna gain behavior at 4 GHz in the yz -plane (see Fig. 1.29), with and without the diplexer attached on its back side, is shown: a reduced influence of the diplexer structure can be observed. Similar results have been observed all over the frequencies of interest.

The adopted paper substrate has thickness $370 \mu m$, $\epsilon_r = 2.55$, and $\tan(\delta) = 0.05$ (at 24 GHz). The fabrication technique is very simple and consists in gluing a copper adhesive tape, etched by means of a conventional photo-lithographic process, onto the paper substrate, as described

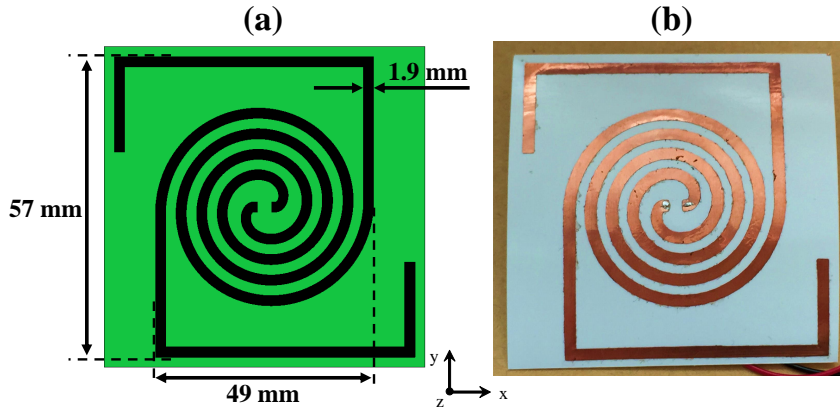


Figure 1.31: (a) Integrated UWB-UHF antenna layout. (b) Prototype on paper substrate.

in [89]. This procedure is employed for all the tag metalization layers. Via-through junctions, which connect the antenna to the diplexer, have been realized by means of copper wires with a diameter of 0.4 mm.

Fig. 1.31 reports the layout of the integrated UWB-UHF antenna. It is worth noting that the frequency-dependent antenna-diplexer matching is obtained with no need to refer to $50\text{-}\Omega$ terminations, thus reducing the needed circuitry between them and the associated losses [90, 91]. In Fig. 1.32 the measured and modeled antenna reflection coefficients are reported, normalized to the $50\text{-}\Omega$ termination of the instrument at any operating frequency: a very good agreement is observed all over the frequency band. With such unified normalization impedance for any frequency, these plots do not directly provide the antenna operating bandwidth, which would require a different normalization impedance for each frequency point. As a representative result, Fig. 1.33, reports the antenna input impedance in the UHF band, where the 868-MHz resonance is clearly displayed.

The challenging requirements of the diplexer network are still applicable. Indeed, it is simultaneously requested to be: i) miniaturized, to ensure the low-profile of the entire tag; ii) inserted in such a way that

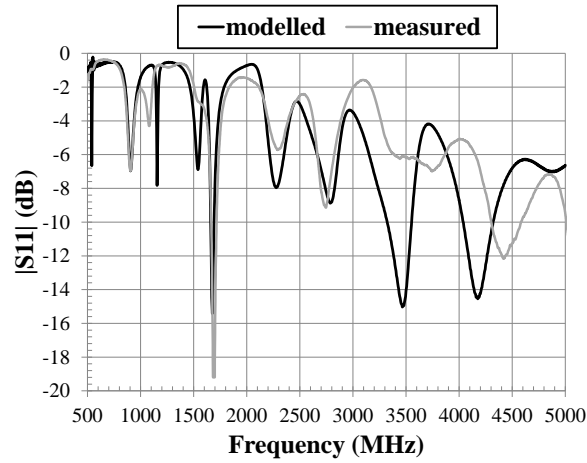


Figure 1.32: Simulated and measured integrated UWB-UHF antenna reflection coefficient with respect to 50Ω (vector network analyzer reference impedance).

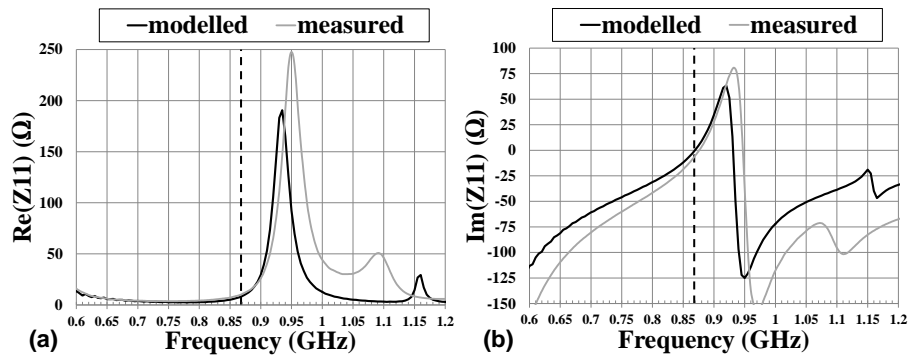


Figure 1.33: Comparison between measured and simulated antenna input impedance in the UHF band, (a) real part and (b) imaginary part.

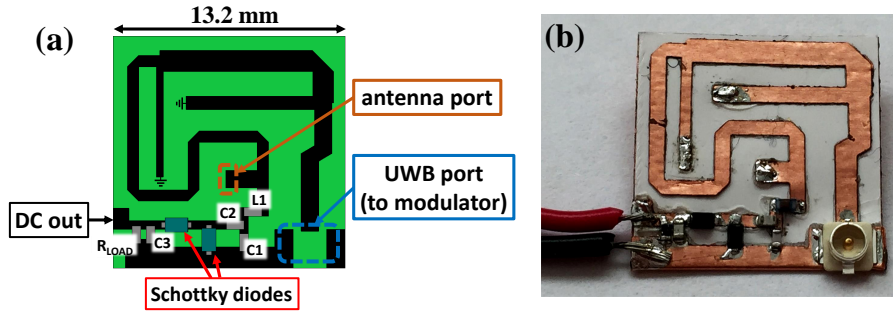


Figure 1.34: (a) Miniaturized diplexer layout, with area $13.2 \times 13.2 \text{ mm}^2$ and thickness $370 \mu\text{m}$. (b) Picture of the prototype on paper substrate.

it does not perturb the antenna radiation characteristics; iii) able to provide two paths: the UWB one, to be loaded by the backscattering modulator, for localization and addressing; the UHF one to be loaded by the rectifier for RF harvesting, with minima insertion losses in both cases.

Once again, with reference to Fig. 1.19, the UWB branch consists of a meandered two-stage microstrip filter, while the UHF one is based on lumped element small SMD components (0402-case) and is connected to a full-wave rectifier employing Schottky diodes. SMDs soldering has been realized with the aid of conductive paste, at temperatures below 300°C , in order not to damage the paper substrate. The new layout of the diplexer network on paper substrate is reported in Fig. 1.34. The values and models of the UHF components are listed in Table 1.2.

1.5.1 Tag UHF Performance

Tag UHF harvesting capabilities are tested by connecting the diplexer UHF output port to the rectifier. The RF-to-dc conversion efficiency is the figure of merit to characterize the tag EH capabilities. The effective RF received power is first measured using the antenna standalone, on a $50\text{-}\Omega$ load, for a fixed distance and orientation of the transmitting UHF

1.5. Paper Implementation

Table 1.2: List of SMD components of the diplexer paper implementation.

Part name	Manufacturer	Product code	Value
L1	Coilcraft	0402HP-18NXGLU	18 nH
C1	Murata	GJM1555C1H1R0WB01D	1 pF
C2-C3	ATC	600L100FT200T	10 pF
D1-D2	Skyworks	SMS7630-079LF	
R_{LOAD}	Vishay	CRCW04028K06FKED	8 k Ω

antenna. By taking into account the mismatch loss factor between the instrument 50- Ω termination and the actual antenna impedance in the UHF band, the available RF power at the diplexer input can be evaluated. The measurement has been carried outside an anechoic chamber, in different indoor scenarios, in order to realistically evaluate the RF energy incidence at the tag locations. In a second step the reference antenna is replaced with the entire tag for the same conditions of the transmitting antenna and the dc rectifier output voltage is measured on the optimized load (8 k Ω for the present design); the dc power is computed accordingly.

The excellent comparison between the predicted EM-based nonlinear results and the measured ones, in terms of RF-to-dc conversion efficiency, are superimposed in Fig. 1.35, for a wide range of input RF power, from -30 to 0 dBm. The corresponding rectified voltages on the optimum load are also superimposed on the same plot. This test campaign, has been repeated for all the possible loading conditions of the diplexer UWB port (i.e., open-circuit, short-circuit or 50 Ω) to confirm the optimized decoupling between the UHF and the UWB operations of the tag. For an available input power as low as -10 dBm, the UWB-UHF tag is able to provide a dc power of 44.8 μ W and a dc voltage of 600 mV. Such

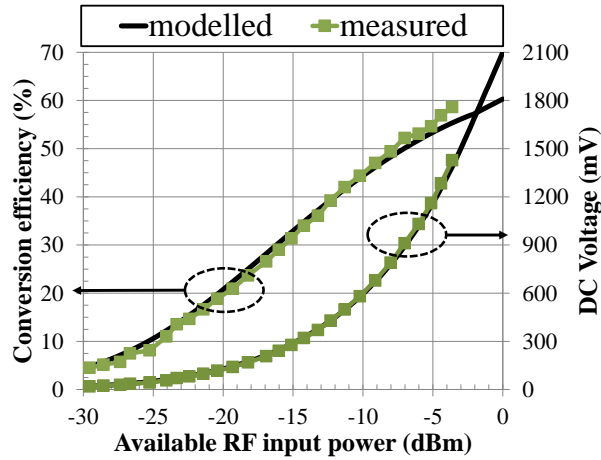


Figure 1.35: RF-to-dc conversion efficiency and rectified voltage on the optimum load for typically available RF input power levels.

quantities are well suitable to activate the ICs of the UWB path, for localizing and addressing the paper tag [92].

For the present case the outcomes of the activity described in Chapter 2 were exploited. Thanks to the new accurate SPICE model of the Schottky diodes, capable of matching the nonlinear behavior of the component, an excellent agreement was obtained.

1.5.2 Tag UWB Performance

Communication in the UWB band is carried out by passive backscattering. For this reason, the diplexer UWB port will be connected to a backscatter modulator. The modulation of the incident interrogation signal can be implemented by a controlled switching of the UWB load between the two conditions of open and short circuit terminations. For the design of the diplexer, a reference $50\ \Omega$ load has been chosen. In this way, when the tag is inactive, no reflections will occur from the tag if the UWB port is terminated on a $50\ \Omega$ load (an equivalent design procedure can be successfully followed for any other reference impedance).

The tag performance in the UWB band are first assessed in terms

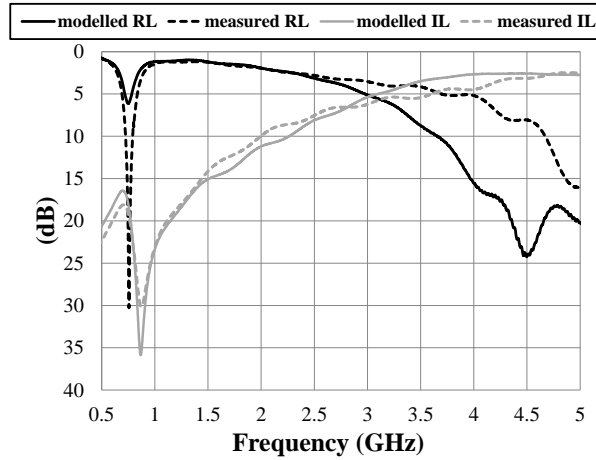


Figure 1.36: Comparison between measured and modeled diplexer antenna port return loss and antenna-to-UWB port insertion loss. Both UWB port and antenna port are referred to 50Ω terminations.

of filtering and matching capabilities of the diplexer network. The scattering parameters at ports 1 and 3 are measured with a vector network analyzer (VNA). The measured and simulated insertion and return loss are compared in Fig. 1.36, where the antenna port is replaced by the 50Ω termination of the instrument.

Despite diplexer optimized miniaturization, because of the absence of a ground plane, the antenna is influenced by the presence of the diplexer metalization, as also reported by Fig. 1.30. Even though this influence appears to be minor, it is worth evaluating to which extent it might affect the communication capabilities of the tag. To do so, an accurate evaluation of the system performance is carried out by means of circuit/EM co-simulation. This procedure allows to predict in a straightforward way the received UWB pulse spectrum and the associated contributions to its amplitude and phase distortion for different tag configuration and different TX-RX respective orientations. From the system point of view, this information is fundamental, especially when time difference of arrival (TDOA) techniques are adopted for localization purposes [93].

1.5. Paper Implementation

For the present case a linearly polarized UWB plane wave is chosen as incident signal of the tag. According to the Harmonic Balance (HB) principles the system excitation must be given in the frequency domain. The adopted UWB pulse waveform has duration and amplitude dynamic designed to fit the European requirements [57], not exceeding -41.3 dBm/MHz of transmitted EIRP in the 3.1-4.8 GHz band: a fourth derivative of a Gaussian pulse with duration $\tau_d = 300 \text{ ps}$ and period $T_{UWB} = 6 \text{ ns}$ is chosen. By the HB-based technique, such pulse is accurately described by a fundamental frequency $f_{UWB} = 1/T_{UWB} = 166 \text{ MHz}$ with $N_H = 64$ harmonics: this way a wider frequency range is retained in the HB analysis in order to accurately evaluate the effects of nonlinear signal processing. The antenna is considered in receiving mode. By resorting to EM theory [94, 95] a rigorous evaluation of the pulse distortion at the antenna port can be carried out. The incident linearly polarized UWB plane wave can be written as:

$$\mathbf{E}_i(\mathbf{r}; \omega_k) = E_i(\mathbf{r}; \omega_k) \left(\cos \psi \hat{\theta} + \sin \psi \hat{\phi} \right). \quad (1.1)$$

In these conditions the equivalent Norton current generators are obtained by combining 1.1 with the electric field the antenna would radiate at a distance r and direction (θ, ϕ) , in transmitting mode. In particular the straightforward application of the reciprocity theorem to the transmitted UWB pulse harmonics ($\mathbf{E}_i(\mathbf{r}; \omega_k)$) and the harmonics of the field transmitted by the spiral antenna when powered by a voltage source of known amplitude U and internal resistance R_0 ($\mathbf{E}_A(\mathbf{r}; \omega_k)$) allows to evaluate the 64 equivalent Norton current generators needed for the analysis, according to the following formula [96]:

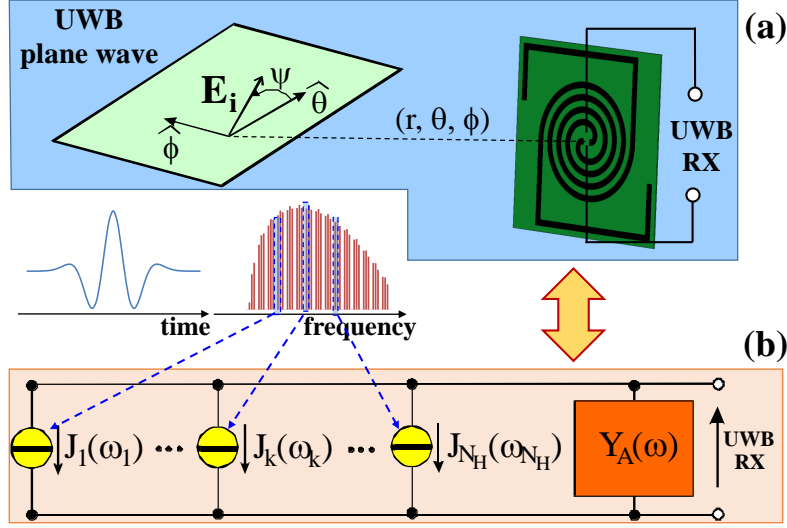


Figure 1.37: (a) Antenna in receiving mode. (b) Corresponding equivalent circuit representation in frequency domain for the HB analysis.

$$J_{eq}(\omega_k) = j \frac{[1 + R_0 Y_A(\omega_k)]}{U} \frac{2\lambda_k r e^{j\beta r}}{\eta} \mathbf{E}_i(\mathbf{r}; \omega_k) \cdot \mathbf{E}_A(\mathbf{r}; \omega_k) \quad (1.2)$$

where \cdot indicates the scalar product, η is the free-space wave impedance, $Y_A(\omega)$ is the frequency-dependent antenna admittance computed by full-wave EM analysis, and $\mathbf{r} = (r, \theta, \phi)$ is the spatial vector defining the UWB source distance and the UWB pulse direction of arrival in the receiver-referred spherical reference frame.

The corresponding situation is depicted in Fig. 1.37: 64 current generators are placed in parallel to the full-wave description of the antenna admittance in the whole bandwidth (by means of the admittance $Y_A(\omega)$) in order to compute the actual received UWB voltage at the UWB RX port: this port is simply given by the balanced antenna terminals for the evaluation of a case without diplexer, while in the second case it corresponds to the port 3 of Fig. 1.19 [97].

In this way, for a given polarization of the incident field (angle ψ in

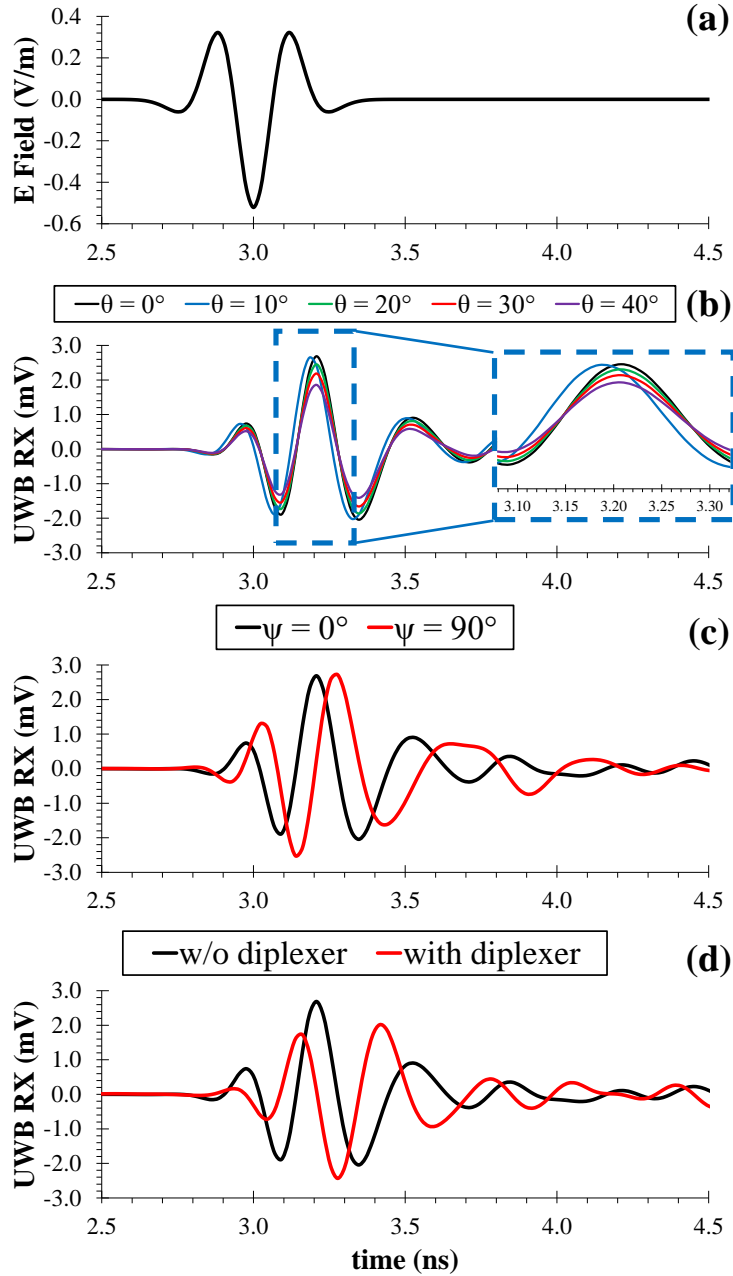


Figure 1.38: Antenna distortion effects on the received pulse. (a) UWB pulse incident on the antenna. (b) Received pulse by the standalone antenna, for fixed polarization ($\psi = 0^\circ$) and varying incident elevation θ angle. (c) Received pulse by the standalone antenna, for fixed AOA and two different polarizations of the incident field. (d) Received pulse by the standalone antenna and the complete tag with the diplexer.

Fig. 1.37), the procedure allows to predict the relationship between a received pulse shape and its angle-of-arrival (AOA) and vice-versa. Furthermore, the effect on distortion due to the antenna or to the antenna-diplexer assembly are available as well, after the circuit-level analysis. Comparison among transmitted (ideal) and received (real) pulses are reported in Fig. 1.38. It is possible to notice that, besides amplitude distortion, a certain phase delay is observed in all the cases. From Fig. 1.38(b) it is possible to see that different AOAs cause short delays, the maximum one being 30 ps, reported for $\vartheta = 10^\circ$. In this case the main contribution for such distortion is due to the shape of the antenna radiation pattern along that direction. Fig. 1.38(c) shows that a much longer delay is obtained if the polarization of the incident UWB field is rotated by 90° , and reaches 70 ps. Such contribution can be attributed to slightly imperfect circular polarization provided by the antenna. Finally, Fig. 1.38(d) shows that the energy levels (defined as the difference between the two received pulses areas over the pulse duration) at the UWB RX port are comparable, which confirms that the presence of the diplexer in the backside of the antenna does not weaken the UWB system activity. From this figure it can also be noted that the presence and absence of the diplexer introduces a 180° phase shift in the received pulse. This last result is not detrimental, since such phenomenon is commonly solved in practical UWB communication by means of a first reference pulse of known polarity for each transmitted bit. Nevertheless this behavior confirms the need for such a co-design technique to take into account all these significant contributions in the evaluation of the system performance. Moreover, it should be noted that in case of a complete backscatter communication, all these delays are doubled.

The tag communication capabilities are finally experimentally vali-

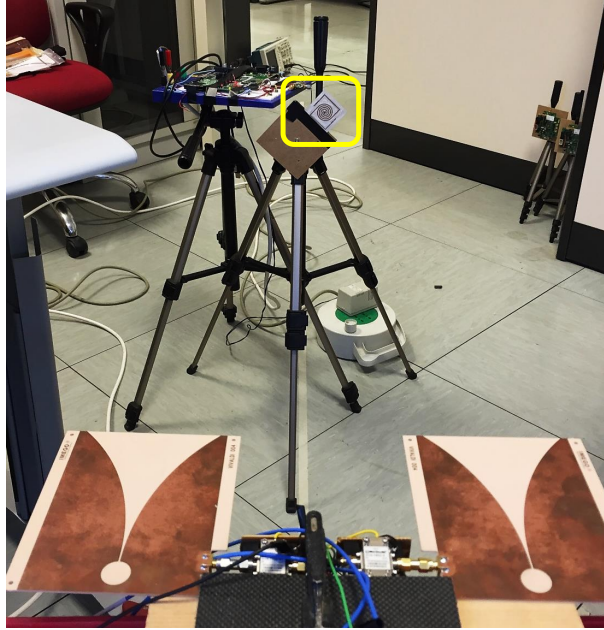


Figure 1.39: UWB communication measurements in a real office scenario.

dated in a real environment, by setting up a scaled test-bed for the UWB reader-tag system. The measurement setup is shown in Fig. 1.39. It consists of an in-house quasi-monostatic linearly polarized UWB reader, fed by an Arbitrary Wave Generator (AWG), with a pulse in this case generated with a Root Raised Cosine centered at the UWB middle frequency of 4 GHz, a pulse-width factor of 1 ns and roll-off factor 0.6 [98]. The AWG sequence of pulses is first amplified by a TX amplifier and then delivered to the UWB reader antenna (a Vivaldi commercial antenna was adopted). With a pulse repetition period set to 50 ns, 200 successive pulses are transmitted and subsequently received by the UWB reader, which is the maximum acquisition window of the available oscilloscope at the receiver side. Such pulses redundancy allows increasing the backscattered energy at the reader side and, therefore, the corresponding Signal-to-Noise Ratio (SNR). Nevertheless, due to the limited acquisition window of the oscilloscope, the transmitted power was increased with the TX amplifier above the spectral mask limit, with a

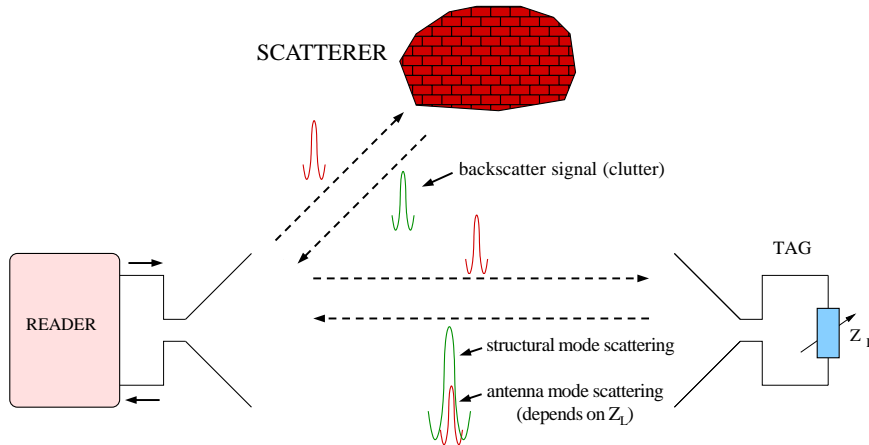


Figure 1.40: Representation of a passive backscattering communication, showing all the distinct signal components: clutter, tag structural mode and tag antenna mode (the only one dependent on the information).

power spectral density of about 25 dB over the -41.3 dBm/MHz limit. The received backscattered signal at the reader side is captured by the UWB RX antenna (identical to the one used for transmission) and amplified before being sampled by the oscilloscope and post-processed with a MATLAB algorithm.

The crucial operation during the post-processing phase is that of being able to isolate the modulation of the pulses by the UWB tag (tag antenna mode) from the received signal, especially in a strong multipath cluttered environment, typical of most application scenarios. Indeed, the complete received signal contains the clutter contribution and both the tag antenna and structural modes, as schematically shown in Fig. 1.40.

The received signal amplitude measured at the oscilloscope with the adopted setup is reported in Fig. 1.41(a) over a pulse repetition period window. In this signal the dominant component is represented by the strong clutter of the multipath environment, therefore the backscattered signal is not directly detectable. After the de-spreading and post-processing phase the clutter component can be removed. Fig. 1.41(b) shows the post-processed resulting signal, now composed of antenna

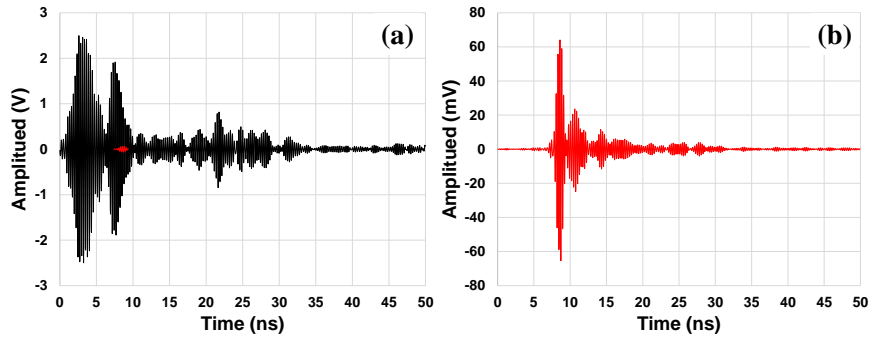


Figure 1.41: Received measured backscattered signal amplitudes: (a) at the oscilloscope with no processing and (b) after post-processing, for a fixed reader-tag distance of 70 cm.

mode component and noise only. Since 200 successive pulses, composing a symbol, are accumulated and summed up to increase the SNR of the received signal, the time domain amplitude shown in Fig. 1.41(b) has also been divided by the number of accumulated pulses, therefore providing in the vertical axis the amplitude of a single backscattered pulse (including amplifiers gain at receiver side). It is worth observing that the time shift of the delayed received pulse is directly related to the reader-tag distance of the signal propagation in air.

During the tests, the modulation was performed at the tag side with a commercial UWB switch driven by an external control board, also visible in Fig. 1.39. The measurements conducted allowed to reveal the tag antenna mode under all the different test conditions. The results, in terms of received power at the reader side, are provided in Table 1.3, where the mean value and standard deviation of 10 consecutive measurements is reported. At a fixed reader-tag distance of 70 cm, the backscatter communication was tested in four different conditions: in the first two the circular polarization capabilities are verified by measuring the received power with two tag positions rotated by 90° ; the same two measurements are then repeated in the presence of an UHF RFID

1.6. Remarks and Future Developments

Table 1.3: Received power by the UWB reader in different link conditions.

Measure	Mean Value	Standard Deviation
Polarization 1 w/o UHF	-45.7 dBm	0.6 dB
Polarization 2 w/o UHF	-45.4 dBm	0.8 dB
Polarization 1 with UHF	-47.3 dBm	0.6 dB
Polarization 2 with UHF	-46.5 dBm	0.9 dB

Table 1.4: Received power by the UWB reader for different distances.

Reader-Tag Distance	Mean Value	Standard Deviation
50 cm	-41.3 dBm	0.8 dB
70 cm	-45.4 dBm	0.8 dB
90 cm	-50.8 dBm	0.7 dB
110 cm	-52.8 dBm	1.9 dB
130 cm	-57.0 dBm	2.9 dB

reader transmitting a maximum ERP of +33 dBm [75], placed at 1.5 m distance from the tag. The successful backscatter communications prove that the simulated pulse waveform changes of Fig. 1.38(c) do not affect the link performance and that, thanks to the decoupling provided by the diplexer network, the nonlinearities of the UHF section do not interfere with the UWB communication capabilities. Finally, Table 1.4 reports the UWB link performance for different reader-tag distances for a fixed tag orientation.

1.6 Remarks and Future Developments

The presented system proposes a novel, single-port, compact, low-profile tag, capable of hybrid UWB-UHF operations, with the goal of providing sensing, communication and high accuracy localization/tracking func-

1.6. Remarks and Future Developments

functionalities. A UHF link is exploited as WPT channel, to energize the tag, while UWB technology is adopted for communication and precise localization. The two functions are able to operate simultaneously thanks to the excellent performance provided by the diplexer network, both in terms of respective matching and strong decoupling between the two operating bands. The designed diplexer miniaturization exerts only minor influence on antenna performance and leads to the optimization of both RF-to-dc conversion efficiency as well as the gain of the overall system. The final tag thickness is lower than 1 mm. Nonlinear circuit optimization have been performed and combined with EM simulations. All provided results, including the intermediate realization, are experimentally verified and validated.

The described diplexer network can be considered a proof-of-concept hybrid realization guaranteeing simultaneous UWB-UHF tag operations. This network could be straightforwardly adopted for the realization of a UWB-UHF chip, with equivalent functionalities, to be placed in the inner part of the integrated UWB-UHF antenna. Such realization would lead to an even more compact, robust and appealing tag, directly adoptable for future next-generation UWB-based RFID systems.

Chapter 2

Diode Model Optimization for Simultaneous Data and Power Transfer

In a scenario in which energy efficiency management is more than ever fundamental, the concept of radiofrequency energy harvesting acquires a leading role to prolong the operation of energy-constrained wireless networks. On the other hand, one of the requirements of future 5G networks is the deployment of systems capable of simultaneous wireless information and power transfer (SWIPT) [99, 100]. Current receiver designs, though, impose technical constraints on the hardware realization of such systems, as circuits for harvesting energy from radio signals are not yet able to decode the carried information directly [101, 102, 103]. This means that the received signal has to be separated into two different paths (as schematically shown in Fig. 2.1(a)): one dedicated to the decoding of the information, the other one responsible for the conversion of the RF energy into dc power. However, the active mixers used in conventional information receivers for retrieving the baseband (BB)

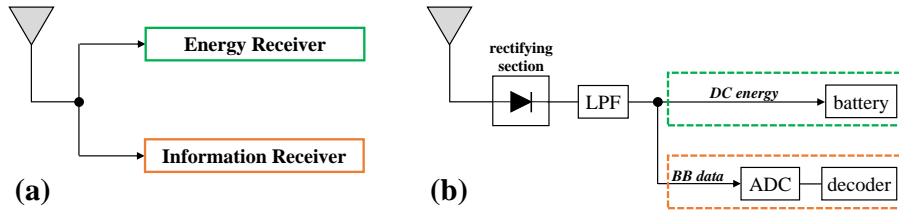


Figure 2.1: Schematic representation of (a) a conventional, separated, harvesting and information receiver architecture, where two distinct nonlinear conversion units are employed and (b) integrated harvesting and information architecture, featuring a single nonlinear rectifying/mixing section followed by a low-pass filter.

information are substantially power-consuming. Obviously, the circuit power consumed by information decoding becomes a significant design issue for simultaneous information and power transfer, since it entails a reduction of the net harvested energy that can be exploited by the device.

These aspects boost the investigation of a new solution able to perform data and power communication in a unique, efficient way, as schematically represented in Fig. 2.1(b), where a sole nonlinear passive device performs the RF-to-BB conversion. The straightforward decoding of a modulated signal integrated in the rectifying section can indeed result in a less power-consuming receiver, by avoiding the use of active devices [101].

To enable the design of such a new architecture, the behavior of the rectifying/mixing element (i.e. the diode) and its distortion introduced on the modulated signal has to be accurately modeled [104, 105]. Unfortunately, in most cases information available to the designer are simply related to those given by the device manufacturer, which can turn out to be not sufficiently accurate. The feasibility of such an integrated harvesting and information architecture, though, can only be assessed recurring to a highly accurate device model. If, as often happens, this

is not straightforwardly provided by the device manufacturer, a more correct and solid model should be derived.

With the goal of reaching a more reliable device model, mandatory step paving the way to investigations of the SWIPT concept, a measurement setup enabling the synchronous acquisition of low and high frequency signals has been adopted for the study of an RF two-tone input signal and its corresponding baseband output [106], therefore oriented to the emulation of a simplified multi-tone/modulated signal processing. The diode employed for this representative example is the Skyworks Schottky SMS7630-079LF [80], a widely adopted diode for RF energy harvesting and wireless power transfer systems [107, 108, 109, 110].

As excitation signal, a two-tone RF input has been employed around the fundamental central frequency of 800 MHz, envisioned for an application in the UHF RFID band, but the proposed setup can be opportunely applied to other frequency bands or modulated RF signals. This setup allows for a rigorous test of the diode model with respect to the baseband intermodulation (IM) products when a two- (or multi-) tone RF signal is applied. Based on these measurements, the manufacturer model was further optimized, in order to reach a highly accurate description of the diode behavior, mandatory for enabling SWIPT implementations. A simple configuration involving a single series diode has been first considered, thus allowing a very precise diode behavior examination by eliminating possible influences from other circuit additional elements. Finally, similar measurements have been also repeated in two different setups for validation purposes, first for a full-wave rectifier and then for a single-diode rectifier.

2.1 Experimental Setup and Model Optimization

A detailed description of the adopted measurement setup can be found in [111]. It is based on an eight-channel large-signal-network-analyzer (LSNA), enabling vector-calibrated nonlinear measurements at both low and high frequencies. Indeed, an LSNA is capable of acquiring a whole spectral content in a single one-shot measurement, including the fundamental component, baseband and harmonics, as well as possible modulation around them [112]. This feature guarantees a synchronized acquisition of both low- and high-frequencies, therefore allowing a direct evaluation of the device baseband response to the RF excitation, in terms of both magnitude and phase.

A picture of the measurement setup is reported in Fig. 2.2. In order to be able to isolate the diode behavior from any other influence of different circuit components, the simplest possible configuration has been chosen for the circuit topology, i.e. a single series diode connected in the center of a $50\ \Omega$ microstrip transmission line. The printed circuit board (PCB) was realized by means of a conventional 0.76 mm-thick Rogers RO3003 substrate ($\epsilon_r = 3$, $\tan(\delta) = 0.0013$ at 10 GHz).

The Skyworks Schottky SMS7630-079LF diode has been measured in the above-described setup by applying a two-tone RF excitation. This rather simple RF signal has been chosen as preliminary investigation, but it can eventually be extended to a more extensive case, for the reproduction of a general modulated signal. The fundamental frequency has been fixed to 800 MHz, while the frequency spacing between the two tones with respect to the fundamental and the average power of the signal (equally divided between the two tones), have been swept from 100 kHz to 1 MHz, with a step of 100 kHz, and from -20 to 0

2.1. Experimental Setup and Model Optimization

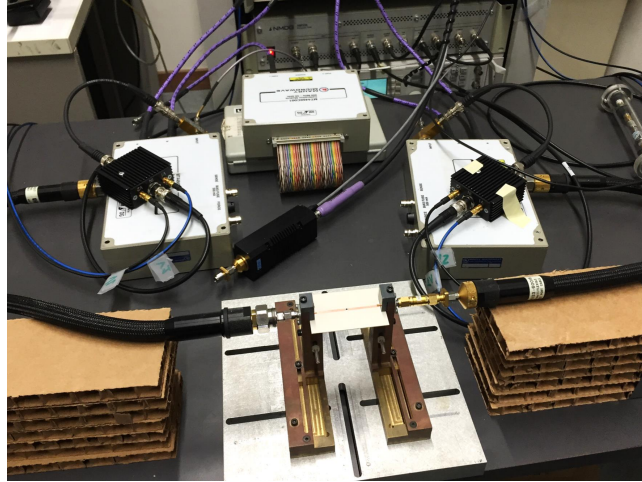


Figure 2.2: LSNA vector-calibrated measurement setup adopted for the single diode measurements. In the center part of the picture it is possible to see the PCB on Rogers substrate.

dBm, with a step of 1 dBm, respectively. The highest input power has been chosen in order not to damage the diode. The incident and reflected voltage waves [113, 114] at the intermodulation products for the two ports of the DUT were measured for all the swept values, at the fundamental frequency, harmonics, and in the baseband. Since the main goal was that of proving the feasibility to read the baseband information carried by the RF modulated signal, the intermodulation products in the baseband were considered and compared to simulated results. The simulations were carried out with Keysight ADS software [115].

The first simulations performed using the diode model provided by the manufacturer did not give enough good agreement between measured and simulated IM products. For this reason an optimization of the model has been conducted, in which the most significant parameters of the diode's Spice model [116] have been tuned, while for the parasitics of the diode package (represented as a parallel capacitance and a series inductance), already optimized values published in literature have been adopted [117]. The optimized parameters are given in Table 2.1, in which

2.1. Experimental Setup and Model Optimization

Table 2.1: Schottky Diode Model Parameters.

Parameter	Manufacturer Value	Optimized Value
Saturation current (I_S)	$5 \mu A$	$4.77 \mu A$
Series resistance (R_S)	20Ω	19.76Ω
Emission coefficient (N)	1.05	1.15
Transit time (TT)	$10 ps$	$11 ps$
Junction capacitance (C_{J0})	$0.14 pF$	$0.154 pF$
Junction potential (V_J)	$0.34 V$	$0.306 V$
Grading coefficient (M)	0.4	0.44
Reverse breakdown voltage (B_V)	$2 V$	$3.8 V$
Package parasitic capacitance	$0.1 pF$	$0.16 pF$
Package parasitic inductance	$1 nH$	$0.7 nH$

the manufacturer model parameters are also reported for comparison.

The transmitted wave of the first IM products around the fundamental tones, i.e. third-order products [106], are provided in Fig. 2.3, in which the measured data are compared with the simulated results obtained after the optimization. The results are reported only for the first frequency spacing, i.e. 100 kHz. Very good agreement is obtained, proving the effectiveness of the optimized model at RF frequencies. In order to prove the feasibility to read the modulated data, though, it is of paramount importance the evaluation of the IM products also in the baseband. To such extent, the first two intermodulation products of the transmitted wave in the BB are reported in Fig. 2.4. The results are provided again only for the first frequency spacing, i.e. 100 kHz, therefore the first two IM products in the baseband occur at 200 kHz (second-order) and 400 kHz (fourth-order), respectively. In these

2.2. Model Validation

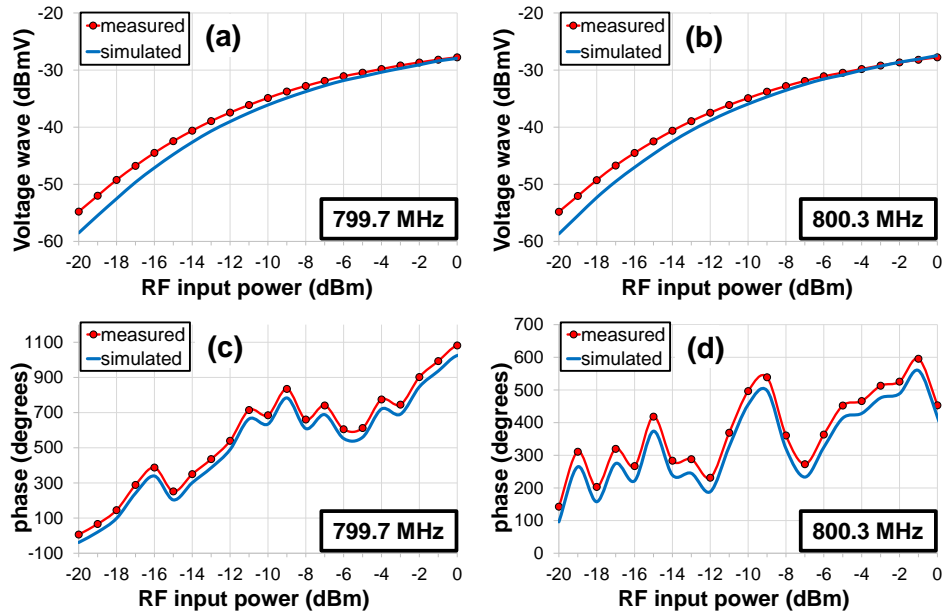


Figure 2.3: Magnitude of the transmitted voltage waves at the third-order (a) low and (b) high IM products around the fundamental frequency and respective phase (c-d).

graphs, it is possible to see that below a power level of approximately -60 dBm, the IM products become noisy. From the comparisons above the noise level, it is possible to observe again a very good agreement between measured and simulated data, in terms of both magnitude and phase.

2.2 Model Validation

The results obtained in Figs. 2.3 and 2.4 proved accurate modeling of the Schottky diode behavior. With the purpose of discerning the diode contribution from those of other circuit elements, for these tests a single diode was considered alone. In order to further prove the validity of the optimized model, a double-stage verification was then performed. For these validations, a different instrument was employed: a nonlinear vector network analyzer - NVNA (model Keysight N5247A), which can

2.2. Model Validation

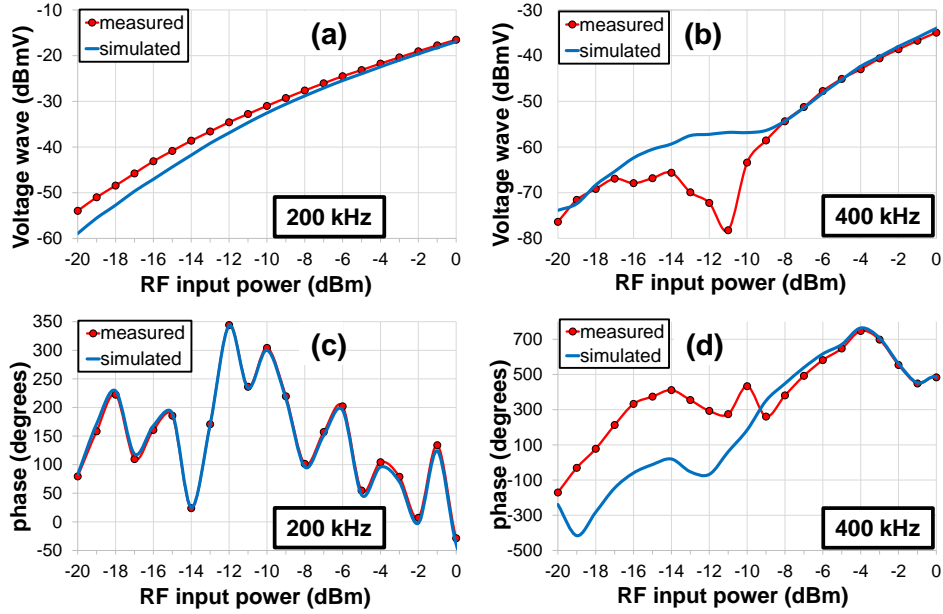


Figure 2.4: Magnitude of the transmitted voltage waves at the (a) first and (b) second IM products in the baseband and respective phase (c-d).

be considered a mixer-based LSNA [112]. Indeed, the NVNA, also called performance network analyzer (PNA), instead of performing a one-shot measurement, sweeps a single local oscillator, down-converting the RF harmonics one by one. It is possible to say that measurements with NVNA are therefore slower, but since in this case the acquisition of the signal is narrowband, the dynamic range of the signal is much larger than the one of the LSNA, allowing the acquisition of signals at much lower power levels.

2.2.1 Frequency Validation

The first verification is aimed at assessing the frequency validity of the model, for this reason a full-wave rectifier matched at 930 MHz has been realized, in this case employing a 0.635-mm-thick Taconic RF60A substrate ($\epsilon_r = 6.15$, $\tan(\delta) = 0.0028$ at 10 GHz). For these measurements the NVNA source is only exploited as single-tone RF input for the rec-

2.2. Model Validation

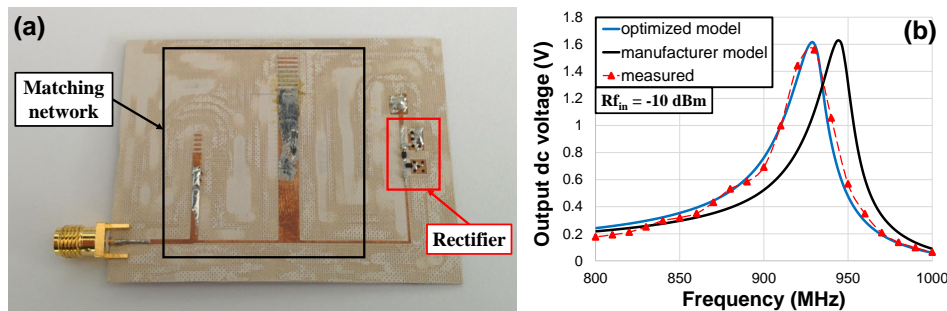


Figure 2.5: (a) Picture of the full-wave rectifier and (b) comparison between measured and modeled OC dc voltage at the rectifier output, for a fixed input RF power of -10 dBm.

tifier, able to provide a constant power level over frequency. The open circuit (OC) dc voltage at the output of the rectifier is then registered for different power levels from -20 to 0 dBm, by sweeping the RF input frequency. Fig. 2.5(a) shows a picture of the full-wave rectifier, where a two-stage microstrip filter is employed for matching purposes. In Fig. 2.5(b), the measurements are compared to simulations for a fixed RF input power, where the substantial difference between the manufacturer and the optimized model of table 2.1 is visible. A very good agreement is observed between measured data and simulated ones employing the optimized model. Similar behavior has been obtained for all the other RF power levels.

2.2.2 Fundamental Frequency and Baseband Validation

In order to further verify the above-reported results, a second validation was performed, this time investigating also the baseband response, for another different configuration, in which the Schottky diode is used in a single-diode rectifier with matching network at 800 MHz. In order to assess the baseband behavior, a two-tone measurement excitation was generated with the NVNA. In this case the frequency spacing between the two tones was chosen equal to 10 MHz, which is the lowest frequency

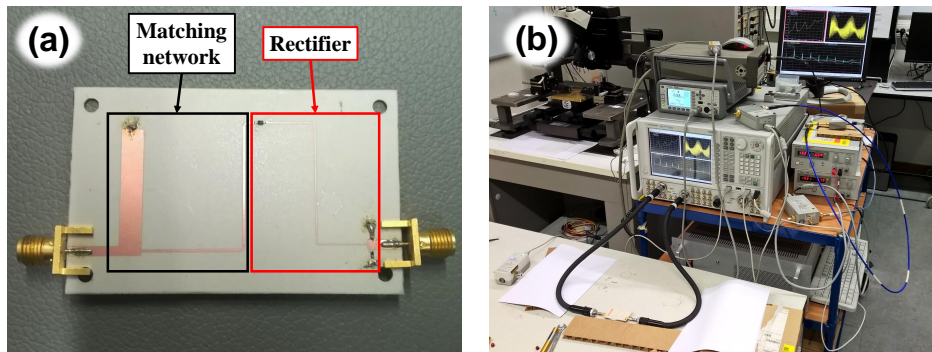


Figure 2.6: (a) Picture of the single-diode rectifier, realized on 0.76 mm-thick Rogers RO3003 substrate and (b) NVNA measurement setup.

the adopted NVNA can measure at. For the verification of the BB response, the rectifier output RC low-pass filter has been designed to be less selective than the first intermodulation product, thus allowing its measurement at the output of the rectifier. At the same time, the output resistance was designed to offer the optimum loading condition to the rectifier. In this case the two tones were excited at 800 and 810 MHz respectively, and the average power of the signal (equally divided between the two tones) was swept over 4 values: [-16.4, -11.5, -6.6, -1.7] dBm. A digital multimeter is connected to the “dc bias” of the NVNA output port, in order to measure also the dc voltage at the output of the rectifier. Fig. 2.6 shows a picture of the prototype and the measurement setup.

During the model optimization from LSNA measurements the unmatched condition of the previous setup was permitting only a low amount of power to be injected inside the diode. For this reason the model optimization led to the modification of all the optimized parameters reported in Table 2.1, except for the reverse breakdown voltage (B_V). The manufacturer B_V value was hence initially left unchanged, since the model was only optimized for lower power levels, typical of energy harvesting and wireless communication scenarios [38, 39, 118].

2.2. Model Validation

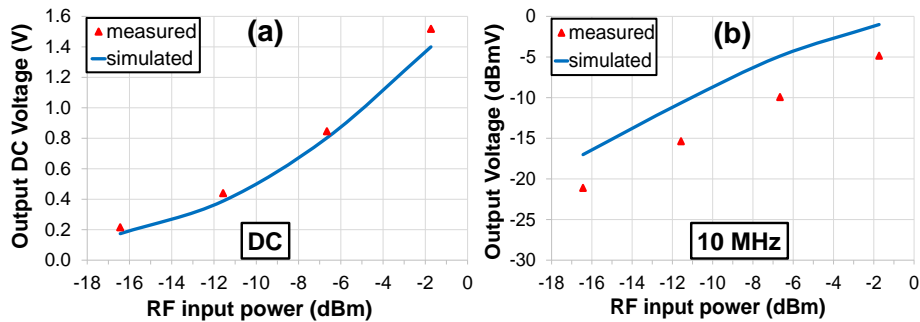


Figure 2.7: (a) dc output voltage of the single-diode rectifier for different values of RF input power and (b) output voltage wave magnitude at the first IM product in the baseband.

Since the new NVNA setup, involving a complete rectifier with a properly designed matching network, allows for a higher power flow through the diode, a correct value for the breakdown voltage, different from the manufacturer's one, has been also empirically derived and reported in Table 2.1.

This finally optimized diode model was adopted during the simulations and the comparison with the measured data is reported in Fig. 2.7. Fig. 2.7(a) shows a good alignment between the simulated and measured output dc voltage. Fig. 2.7(b) reports the comparison between the simulated and measured output voltage wave at 10 MHz, corresponding to the first intermodulation product. Also in this case it is possible to observe a reasonable agreement, while the slight discrepancies are due to the fact that in this setup the circuit comprises a higher number of elements, namely the input matching network and the RC filter at the output of the rectifier, which introduce more uncertainty in the system, as well as possible slight variations among different diode chips.

2.3 Remarks and Future Developments

The demand for efficient energy management calls for new solutions able to possibly integrate information decoding and power harvesting in a unique operation. The reported results highlight how the available manufacturer device model is typically not accurate enough to allow such integrated designs. By means of a proper measurement setup, the model of a widely adopted Schottky diode was optimized by analyzing the baseband response to an RF two-tone excitation signal, therefore proving the feasibility of such an integrated system for a simplified RF multi-tone input. The same inspection was then also applied to different rectifier configurations, as validation.

The promising results provided foster the future investigation for a direct recovery of the information carried by a modulated signal at the baseband output of a rectifier. Nevertheless practical implementation of integrated data and power transfer is still facing several challenges that call for further research efforts, encompassing different aspects of a SWIPT system.

The research of an optimal modulated signal is of primarily importance. Indeed, the best trade-off should be chosen between the optimization of the power conversion efficiency and the data transfer capability. Multi-tone signals have already proved the possibility to increase the system performance in different applications. In [119, 120] the concept of power optimized waveform (POW) has been used for improving the reading range in RFIDs, while in [121] it is exploited to enhance wake-up radios (WURs) sensitivity. Moreover, different solutions have been presented to increase the RF-to-dc conversion efficiency of a rectifier [122, 123, 124, 125, 126, 127]. In most cases high peak-to-average power ratio (PAPR) waveform are adopted to increase rectenna

2.3. Remarks and Future Developments

efficiency. In particular, [126] reports closed-form equations theoretically supporting the use of PAPR waveforms, [125] provides a thorough comparison among different approaches for the increase of rectifiers efficiency, while [127] estimates the impact of different solutions on the choice of the rectifier optimum load. A further step is the evaluation of the impact of different modulation schemes on the rectification capabilities [128, 129, 130, 131], though a joint analysis of the operation of both power and information transfer, as recently reported in [132], appears to be the most reliable approach to appraise the total system performance.

Chapter 3

Rectenna Array for Long Distance Autonomous IoT Tag Localization

Next generation RFID systems are expected to provide not only secure identification, but also advanced functionalities, one of the most urgent being high-precision tags localization [133]. Indeed, the capability to localize objects distributed in the environment in real-time with great accuracy (few centimeters) would pave the way to innovative context-aware applications with huge market potential.

Current RFID systems are usually based on the narrowband Gen. 2 standard [46], which was initially devised only for identification purposes. Nevertheless, rough localization information can be obtained exploiting different attributes of the received signal, such as: received signal strength (RSS), signal time of arrival (TOA), time difference of arrival (TDOA), or angle of arrival (AOA) [134, 135, 136, 137, 138]. These methods can reach decimeter level accuracy in line of sight (LOS) conditions, but strongly suffer from deep fading, typical of indoor multipath

propagation. To date, the best positioning accuracy, in the order of 3-15 cm, is offered by solutions adopting the impulse radio ultra-wideband (UWB) technology. Indeed, when transmitting pulses with duration in the order of a few nanoseconds, time-measurements (e.g., TOA/TDOA) are sufficient for gathering all the necessary information from the received signals and they are able to guarantee high localization accuracy, thanks to the capability of easily discriminating multi-path components [48]. Unfortunately, all available standards (e.g., IEEE 802.15.4a or 802.15.4f [139, 140]) and commercial solutions are uniquely based on active tags (i.e. equipped with batteries and power-hungry active transmitters), and hence not capable of self-sustained passive operations. In order to guarantee high-accuracy localization along with energy autonomy of tags, a successful solution could be represented by the combination of UWB technology with passive backscatter modulation principles [52], achieved by means of a proper time variation of the tag antenna load [47].

The viability of this solution is strictly dependent on the possibility to properly energize the passive tags with battery-less techniques. Indeed, tag operations, such as recovery and interpretation of the received signal and antenna load modulation, require auxiliary energy availability. For this purpose, the combination of UWB techniques and far-field WPT strategies at UHF frequencies is proposed, similarly to what already anticipated in Chapter 1. Nonetheless, battery-less tags make the design of such systems very challenging, calling for extremely low power consumption electronics and efficient energy recovery solutions.

With these premises, an indoor scenario is envisaged, where reference nodes, referred to as UWB readers, are distributed in the environment in fixed locations. The reference nodes are also acting as wireless UHF

power providers, wirelessly energizing the tags with the maximum allowed RF transmitted power in the European RFID band, i.e. 2 W ERP [75]. The system shall operate in a typical indoor harsh environment where multi-path and non line of sight (NLOS) conditions might be frequent. Moreover, tags might be as far as 10 meters from the reference nodes, or more. In order to satisfy the strict power budgets dictated by the application scenario, it is essential that the intrinsic consumption of tags be aggressively low (a few μW) and to employ electronics working at minimum operating voltages, which are in general in the 1.8 - 3 V range. From the electronics point of view, it might result convenient being able to satisfy the low-power requirements without recurring to the development of new dedicated ICs, though at the expense of slightly higher power consumption. Sub- μA energy harvesting circuits with power conversion and management functionalities implemented with discrete components have been recently designed and successfully tested with good performance and efficiency [141], although for piezoelectric sources. These components require at least few μW of input dc power to work properly. For the present power management unit (PMU) the recent, commercially available TI BQ25570 has been adopted, well suited for ultra-low power applications [142, 143]. The dc/dc converter is specifically designed to efficiently acquire and manage the μW of power generated from a variety of dc sources. In this case the rectified voltage of the UHF rectenna is provided at its input. This component is then responsible of increasing the dc voltage input to higher values, usable as supply voltage of the active components of the tag, as well as to store sufficient energy locally, to sustain a single localization operation. During the localization phase, energy consuming operations are executed by the tag: a microcontroller unit (MCU) is

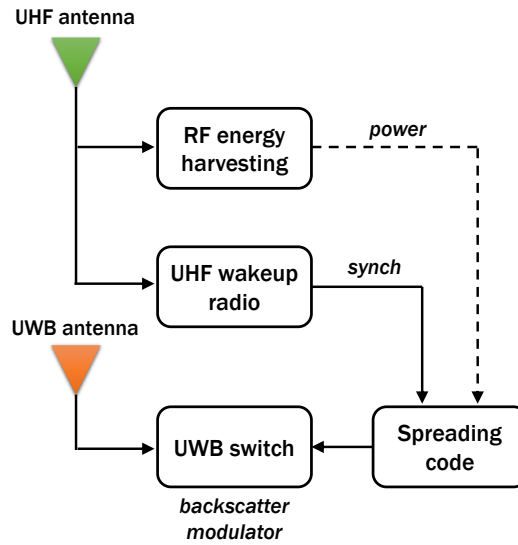


Figure 3.1: Schematic representation of the system architecture.

activated and a UWB switch modulates the received UWB signal for the backscattering. Indeed, the MCU represent the most power-hungry part of the system and strategies to keep it in an idle state for most of the time, except during the active phases, play a crucial role [144]. To this extent, usage of a low-power and low-latency wake-up radio (WUR) is adopted, with the purpose of waking up the active components only when required [145, 146].

3.1 System Architecture

The proposed system architecture is reported in Fig. 3.1 and more in detail in Fig. 3.2, where the single electronics components are represented.

The tag is composed of a UWB antenna whose reflectivity is modulated using a wideband switch loaded on short and open circuits. The energy is provided by an energy-harvesting block working in the UHF band, connected to a UHF antenna. As clearly seen, the dc source com-

3.1. System Architecture

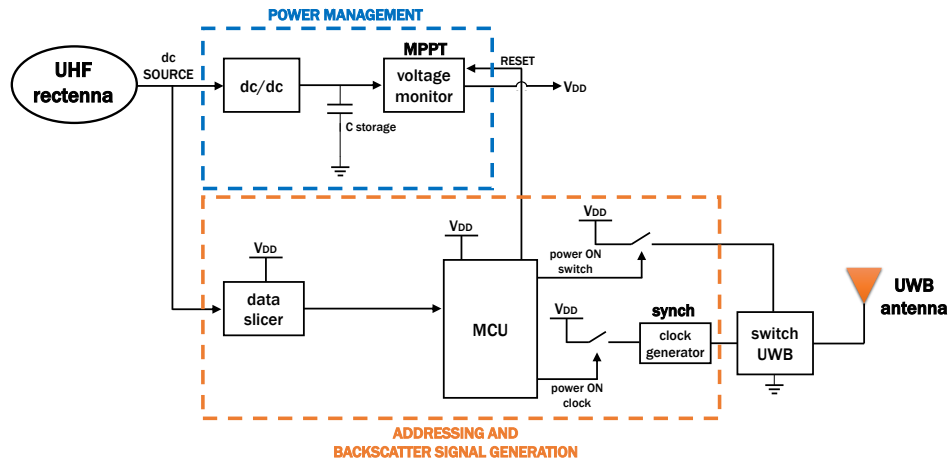


Figure 3.2: Detailed representation of the digital electronic blocks.

ing from the rectenna has to be split into two parts: one responsible for the provisioning of power to the tag and the other one for the WUR implementation. Besides tag wake-up, the WUR is responsible also for providing the proper timing for the switch operations. As detailed in Fig. 3.2, the dc/dc boost/buck-converter regulates the voltage level to the circuitry needs. It operates with a joint voltage monitor, which provides the power to the circuit when it is within a given range of valid supply voltages (between 2.3 and 2.5 V). The PMU implements also maximum power point tracking (MPPT) in order to maximize the power extracted from the energy harvester source. The value of the storage capacitor has to be optimized for the best trade-off between reduced start-up times (lower values, e.g., nF) and reduced switching of the dc/dc converter and thus of the consumed power (higher values, e.g., μF). However, the value of the capacitor has to be chosen large enough to sustain a single activation of the tag and, because of the consistent overall consumption in the active phase, this inevitably leads to long wake-up times. This consideration further motivates the adoption of a low-latency WUR in parallel to the main harvesting section. In the addressing segment, the

3.1. System Architecture

data slicer is responsible for providing a stream of digital data to the MCU, which has to wake-up when the tag address is recognized. The control logic then provides to the backscatter modulator the spreading code and the proper timing for switching the RF path between open and short circuits. The address and synchronization signals are sent by the UHF power provider nodes, with an ON-OFF keying modulation of the CW UHF carrier. In between each interrogation cycle, a continuous UHF CW signal is emitted by these nodes, to let all tags collect the sufficient energy needed to operate in case of a received interrogation.

The most stringent requirement is imposed by the PMU start-up from a completely discharged state (cold start). In this situation the TI BQ25570 needs an input dc voltage of 330 mV, together with a dc input power of 15 μ W. Once started, it is able to continue the charging operation with input voltages as low as 100 mV and it consumes only 7.5 μ W. These values are adopted as reference for the design of the rectifying unit and define the maximum operative distance of the system.

3.1.1 Performance Evaluation of the Available Solution

It is worth noting that two different requirements are dictated by the PMU, depending on whether it is in a completely discharged state or it is already accumulating energy. When designing harvesting systems, often the second situation is considered, therefore claiming the PMU consumption in a normal operation state. This assumption, though, should be appraised carefully. Indeed, in practical scenarios it is typically not possible to know a priori whether the interested tag has already been exposed to a favorable power delivery condition, and has therefore already overcome the “cold start” phase, or not, and is therefore completely inactive. For this reason, the PMU specification considered hereunder

will be all referring to the situation in which a “cold start” activation is foreseen, which defines the most stringent requirement.

As a first evaluation, the performance of the already available solution, presented in Chapter 1, are assessed. A compact, one-port, integrated UWB-UHF tag was described, which thanks to a properly optimized diplexer network is able to provide simultaneous UWB operation and UHF energy conversion. For an evaluation of the rectenna performance in the present scenario a UHF transmitter is considered, emitting the maximum ERP of 2 W in the UHF band and located at 10-meter distance in free-space propagation. In the best-case RF link conditions, i.e. with the TX antenna linearly polarized and in perfect polarization matching with the RX dipole, given the 0 dBi gain of the receiving antenna, the RF received power at the harvester input is -16 dBm ($\sim 25.1 \mu\text{W}$). As described in Section 1.5.1, with this input power level the measured dc voltage is approximately 240 mV and the RF-to-dc conversion efficiency is equal to 29%, which results in a total available dc power of 7.3 μW . Moreover, it is worth noting that if polarization worsens, the available RF power is reduced and the dc output decreases accordingly. Hence, it is clear that with a conventional rectenna design, as the one adopted for the integrated UWB-UHF tag of Chapter 1, the PMU requirements cannot be satisfied for the envisaged long distance operations.

In order to obtain a higher dc voltage at the rectenna output, a possible solution could be that of changing the rectifier topology and implement voltage multiplication. Indeed, by increasing the number of rectifying stages, as schematically represented in Fig. 3.3, it is possible to obtain an according gain in terms of dc voltage. The results comparing different multi-stage topologies are reported in Table 3.1, where one

3.1. System Architecture

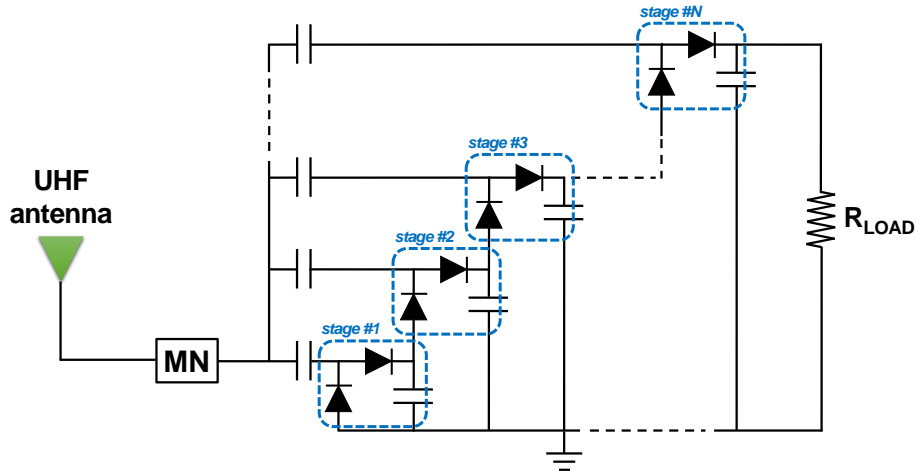


Figure 3.3: Schematic representation of a multi-stage rectifier topology for voltage multiplication, connected to the UHF antenna through a proper matching network.

Table 3.1: dc outputs of the multi-stage rectifier topology.

# stages	V_{dc} (mV)	RF-to-dc eff.	P_{dc} (μ W)
1	240	29 %	7.3
2	354	25.5 %	6.4
4	392	21 %	5.3
6	398	16 %	4.0
8	305	12 %	3.0

stage corresponds to a full-wave rectifier, identical to the one described in Section 1.5.

The advantage obtained in terms of rectified voltage by increasing the number of stages is evident: by merely doubling the number of stages the 330 mV voltage requirement is guaranteed. Nevertheless several drawbacks pertain to this solution. Indeed, every additional diode employed in the rectifier introduces also additional voltage drops, which contribute to overall increased losses. Moreover, as the number of stages raises, the optimum load of the rectifier assumes higher values. This twofold effect

translates in a reduction of the conversion efficiency and therefore of the dc output power. In addition, it is also possible to observe that beyond a certain number of stages, the increased diode losses suppress also the advantages in terms of voltage multiplication.

3.2 Single Rectenna Design

The obtained results show that adopting a multi-stage rectifier is not a viable solution for the present case. This outcome motivates the investigation of new harvesting strategies, to increase the activation distance of the tag. An alternative solution would be that of implementing a multi-rectenna harvester: in this way both voltage and power multiplication are foreseen.

In order to better address the design of a UHF rectenna array, the integrated, one-port UWB-UHF architecture of Chapter 1 is temporarily abandoned. As a first step a classical single rectenna, composed of a UHF monopole, is first designed, to be used for performance comparison with the correspondingly-derived array architecture. Besides the comparison between the single rectenna and the rectenna array, this new single rectenna design is also employed for the analysis of a novel WUR implementation.

As anticipated, in parallel to the rectenna design a wake-up radio is also adopted for the present tag. The purpose of the WUR is to bound the employment of the power-consuming components of the tag to the sole active phase. These components can therefore be kept in an idle, listening state and be waken-up by the low-latency WUR when the specific tag is addressed. The input for the WUR implementation has to be derived from the UHF received signal. Recent designs dedicate a separate antenna to the WUR receiver [147, 148]; this solutions, though, would

3.2. Single Rectenna Design

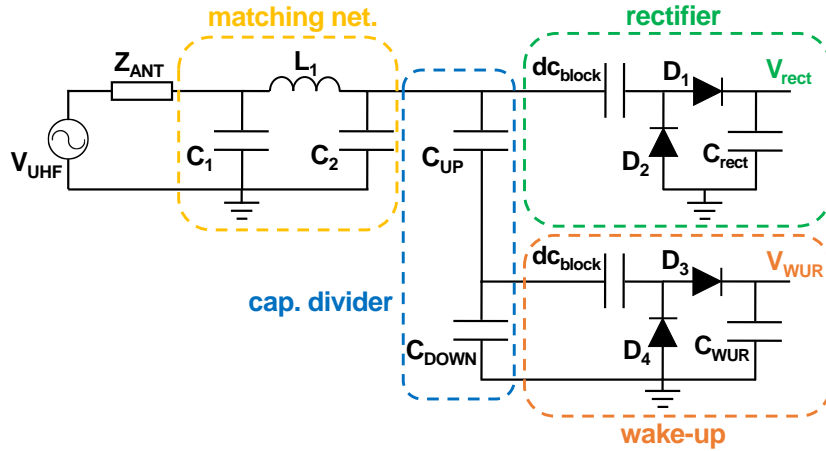


Figure 3.4: Circuit schematic of the monopole rectenna. The RF available power is modeled as an ac voltage source with the antenna impedance as internal resistance. V_{rect} and V_{WUR} are fed at the input of the respective electronic block described in Fig. 3.2.

require much larger tag areas, contrasting with the usual tag miniaturization requirements. For this reason, the possibility to integrate the rectification and WUR functionalities within a single antenna are much more appealing. To this extent the most obvious solution would be that of providing an input for the WUR by splitting the dc voltage at the output of the rectifier with a conventional resistive divider. This solution, though, is by definition lossy, as it involves lossy components. Given the extremely low values of power available at the high distances foreseen for the present system, losing even only few μW of power is not acceptable. For this reason a novel solution is proposed, where the voltage is split at RF level, by means of a capacitive divider. In this way, only reactive components are involved, resulting in almost no losses, except for the parasitic ones due to the non-ideal capacitors. The capacitive divider topology is provided in Fig. 3.4, where the rectenna circuit schematic is shown.

Table 3.2 lists the SMD components used for the circuit, while Fig. 3.5 shows the realized rectenna prototype on a 0.5-mm-thick Rogers

3.2. Single Rectenna Design

Table 3.2: List of SMD components of the monopole rectenna.

Part name	Manufacturer	Product code	Value
L_1	Coilcraft	0603HP-18NXGLU	18 nH
C_1	Murata	GJM1555C1H120FB01	12 pF
C_2	Murata	GJM1555C1HR50WB01	0.5 pF
C_{UP}	Murata	GJM1555C1HR70WB01	0.7 pF
C_{DOWN}	Murata	GJM1555C1H1R0WB01	1 pF
dc_{block}	ATC	600L100FT200T	10 pF
D1-D2-D3-D4	Skyworks	SMS7630-079LF	
C_{rect}	Murata	GJM1555C1H100FB01	10 pF
C_{WUR}	Murata	GJM1555C1H100FB01	10 pF

RO4350B substrate ($\epsilon_r = 3.48$, $\tan(\delta) = 0.0037$ at 10 GHz).

Finally, the performance of the monopole rectenna are provided in Fig. 3.6. Fig. 3.6(a) reports the values of the OC voltages at the rectifier and wake-up outputs, for different values of available RF power at the input of the rectenna. It is possible to see that, with the proposed capacitive divider implementation, V_{WUR} is a derivation of the main dc output, corresponding to about 20-25% of V_{rect} . In Fig. 3.6(b) the rectified dc voltage on the optimum load (equal to $10 k\Omega$ for the present case), as well as the RF-to-dc conversion efficiency of the rectifier are reported, for different RF power levels at the rectenna input. Very good agreement between measured and simulated results is obtained in all cases, except at the higher power levels, where the breakdown voltage of the Schottky diode is not providing accurate model prediction, as described in Chapter 2.

The monopole antenna exhibits a realized gain of 1.8 dBi and a radiation efficiency of 95%. Thanks to the slightly increased radiation

3.2. Single Rectenna Design

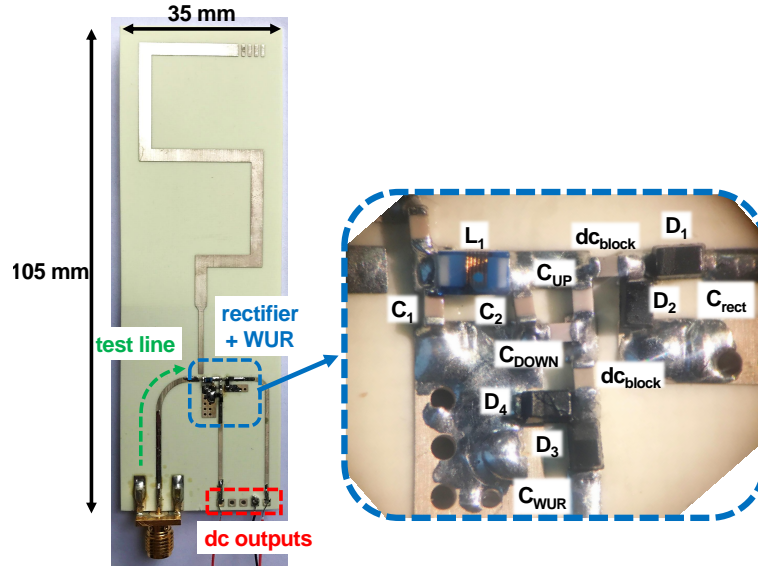


Figure 3.5: Picture of the monopole rectenna prototype. The zoomed view shows the layout of the rectifier and wake-up circuitry.

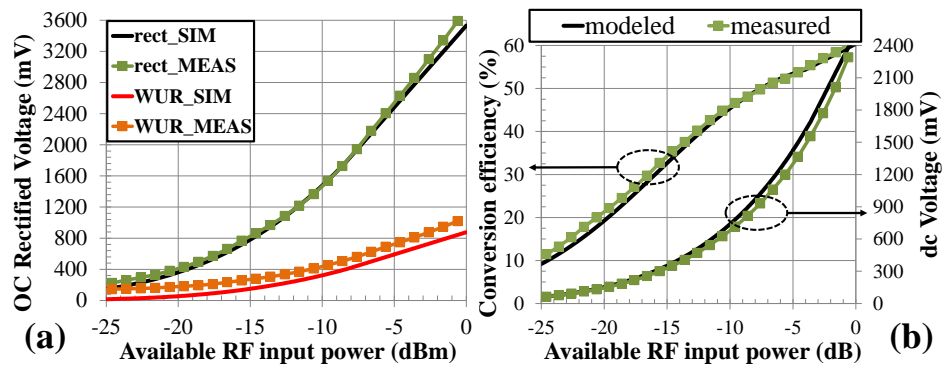


Figure 3.6: Comparison between measured and modeled (a) OC voltages at the output of the rectifier and wake-up sections and (b) RF-to-dc conversion efficiency and dc voltage on the optimum load of the rectifier, for different values of RF input power.

3.2. Single Rectenna Design

performance with respect to the one provided by the antenna of Chapter 1, when transmitting 2 W ERP at 10-meter distance, the RF received power at the harvester input is -14.3 dBm ($\sim 37.2 \mu\text{W}$). With this input power level the measured dc voltage is approximately 360 mV and the RF-to-dc conversion efficiency is equal to 35%, which results in a total available dc power of 13 μW . The obtained dc voltage is able to satisfy the PMU requirements, although the dc power is still below the requested value. Nevertheless, it is worth noting that also in this case the RF received power is assessed in the best RF link conditions, i.e. assuming perfect polarization matching between the transmitter and the receiving antenna. The possibility to rotate the tag can be provided by adopting a circularly polarized antenna at the transmitter side; this however causes a 3 dB power drop, resulting in dc voltage and power outputs of 220 mV and 5 μW , respectively. The obtained performance, therefore, cannot be considered satisfactory.

Besides the obtained rectifier dc outputs, the designed rectenna proved the validity of the capacitive divider solution, which is able to provide a WUR implementation with no need for a dedicated antenna. In order to assess the effectiveness of this solution, though, it is important to evaluate how the two signals might affect each other. Indeed, since the WUR is obtained from a direct derivation of the RF voltage which feeds the rectifier, a variation of the loading conditions of one signal could translate in a consequent alteration of the second one. Though the WUR alteration due to different rectifier conditions is an obvious consequence of the adopted capacitive divider implementation, the opposite case would result particularly detrimental, since the WUR should perform its operations in a seamless fashion, without affecting the main functionalities of the harvester.

3.2. Single Rectenna Design

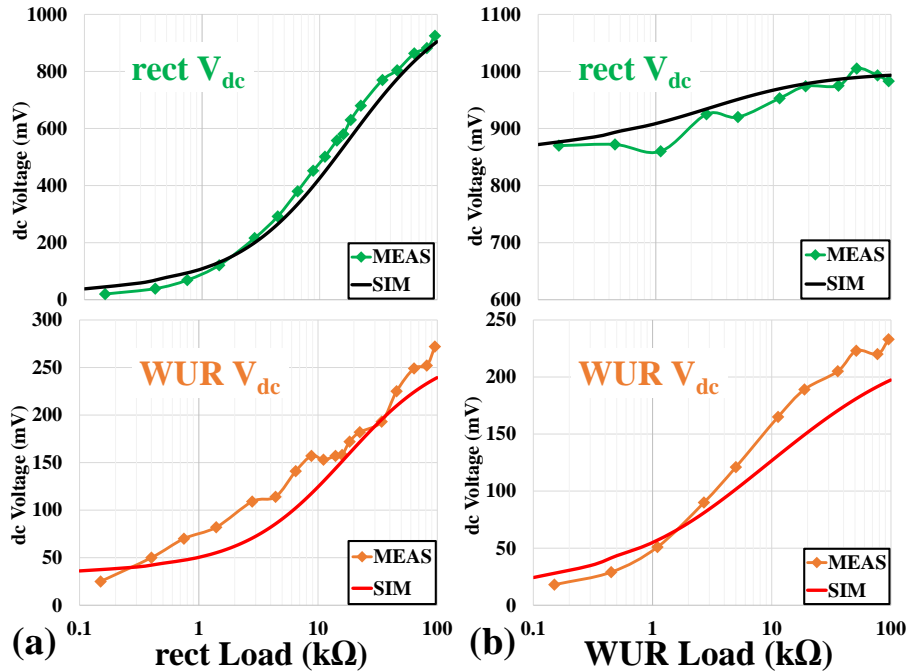


Figure 3.7: Comparison between measured and modeled dc voltage at the rectifier and WUR outputs for different values of (a) the rectifier load and (b) the WUR load.

To this extent, the load at the rectifier output is swept from an almost short circuit (SC) condition to an almost open circuit (OC) one. Then, the dc outputs are evaluated for both the rectifying and wake-up sections. The resulting voltage patterns are depicted in Fig. 3.7(a). As expected, variations of the rectifier voltages reflect in direct variations of the wake-up ones, being these directly derived from the main voltage signal. This effect, though, does not result in fake tag activation. Indeed, for almost 95% of the time the PMU provides a constant value at the rectifier output, corresponding to the optimum loading conditions, and even though the MPPT periodically refreshes its state, the refresh rate is significantly lower (few Hz) with respect to the frequency of the UHF CW modulation employed for tag addressing (in the order of kHz), therefore it is not affecting the WUR functionalities. Even though the WUR load can be considered almost purely reactive, the

3.3. Four Dipoles Rectenna Array

dual evaluation is done by sweeping its value and comparing how this translates respectively to the rectifier and the wake-up outputs. The corresponding results are given in Fig. 3.7(b). Obviously, the voltage at the wake-up output is changed accordingly, but it is possible to observe that this variation exerts only a minor influence on the rectifier signal. These evaluations are reported for a fixed available power level of -13 dBm, but equivalent conclusions are obtained all over the expected incident power range. Therefore, these results prove the effectiveness of the proposed seamless implementation of the wake-up radio.

3.3 Four Dipoles Rectenna Array

The results obtained by the reported rectenna designs are not able to satisfy the system requirements, especially in terms of rectified power delivered to the PMU. For this reason, the investigation of new harvesting strategies is carried out, in particular focusing on the possibility to implement a multi-rectenna harvester, for which power multiplication is foreseen.

When it comes to rectennas connection in the design of a multi-harvester array, two possibilities are typically envisioned: series- or parallel-connection among the rectenna elements [149, 32, 150, 151, 152, 34, 153, 154]. In both cases an increment of the overall dc power is expected at the array output; in case of series-connection the overall dc voltage is also multiplied, while if a parallel-connection is adopted the resulting dc current is augmented. The 360 mV obtained with the monopole rectenna prototype satisfy the 330 mV requirement of the PMU with a very short margin and only in case of perfect polarization matching with a linearly polarized transmitter. For this reason the series-connection has been adopted in the rectenna array design, with

3.3. Four Dipoles Rectenna Array

the goal of satisfying the $15 \mu\text{W}$ power requisite and at the same time guaranteeing a consistent margin in terms of dc voltage.

Regarding the choice of the array elements, a thoughtful analysis has to be undertaken. Indeed, in most harvesting scenarios direction of arrival and polarization of the incident RF signal is usually unknown or time-varying. The most effective solution for unknown polarization reception is the use of a couple of dual linearly-polarized antennas [95, 155] or circularly polarized ones [156], while the unknown direction of arrival forces the use of non-directional antennas, the most common being dipole-like antennas, which have omnidirectional behavior. A dipole-like antenna, such as the one described in Section 3.2, represents the most adopted omnidirectional choice, but it obviously presents radiation nulls along the dipole axis direction. A second drawback ensues from its linear polarization (LP), which can result in zero RF power at the rectenna input in case of cross-polarized incident signals. This obstacle is often overcome by adopting circular polarization (CP) at the transmitter side, nevertheless in most cases a direct control on the radiofrequency source is not possible.

For the present rectenna array a dual-linear polarization has been adopted and further extended in order to better fulfill dc requirements: two couples of dual linearly-polarized UHF planar dipoles are integrated on the same substrate, together with an Archimedean spiral for UWB communication, this way leading to a compact exploitation of the tag area. The dual linear polarization allows to receive the same amount of RF power irrespective of the incident polarization, i.e. CP, both left- and right-handed, and LP, for any given polarization rotation: this represents an unreachable performance for a CP receiving antenna. Moreover, thanks to the integration of two couples of dual linearly-polarized

3.3. Four Dipoles Rectenna Array

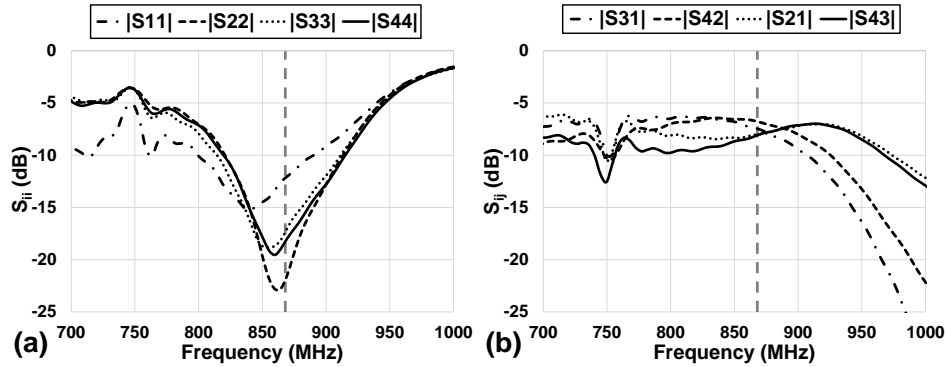


Figure 3.8: Modeled dipoles (a) reflection coefficient and (b) mutual coupling. Ports numbers are in accordance with the numbering of Fig. 3.9.

antennas, the resulting RF received power by the harvester can be further increased, by combining the outputs of four distinct rectifiers.

Since distance among the dipoles is within fractions of wavelength, a quite strong coupling among antenna elements is reached. Fig. 3.8(a) reports the simulated reflection coefficients of the four dipoles. Despite the good matching for all the elements at 868 MHz, a strong coupling is observed in Fig. 3.8(b). The complete avoidance of this mutual influence could be reached only by placing the antennas very far from each other, procedure that would lead to impractical tag dimensions. For this reason this coupling is instead exploited for the optimization of the radiation characteristics of the tag. The integration of the five antennas on the same device is optimized with a parametric study. The UWB spiral, covering the 3.1 to 4.8 GHz band, is fixed in a central position. With the goal of reaching the higher gain in all the possible directions, the dipoles relative distance, d , with respect to the operating wavelength, has been varied by λ/x , with x swept from 1 to 6, where $x = 6$ corresponds to the minimum possible distance, i.e. dipole and spiral overlapping. Some representative results in terms of gain patterns are reported in Fig. 3.10, while Fig. 3.9 illustrates the optimized layout, where the UHF dipoles have been meandered for miniaturization purpose.

3.3. Four Dipoles Rectenna Array

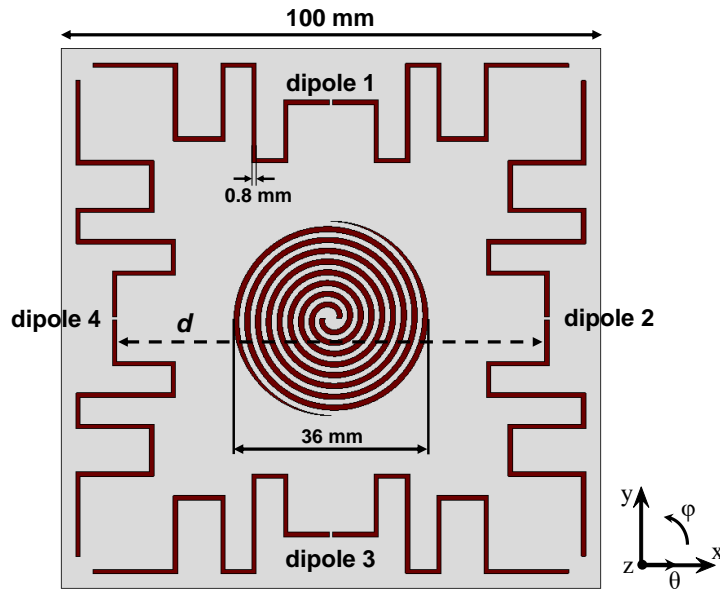


Figure 3.9: Layout of the quasi-isotropic four-element harvester, co-planar with a UWB spiral antenna for the optimum dipole distance $d = \lambda/4.3$. Dimensions $100 \times 100 \times 1.5 \text{ mm}^3$, designed on Rogers RO4350B substrate ($\epsilon_r = 3.48$, $\tan(\delta) = 0.0037$ at 10 GHz).

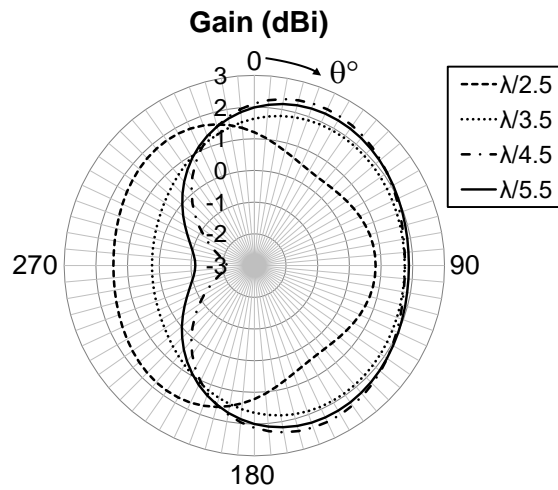


Figure 3.10: Gain patterns of dipole 1 in $\varphi = 90^\circ$ -plane (yz -plane) (see Fig. 3.9), for different inter-dipole distances $d = \lambda/x$.

3.3. Four Dipoles Rectenna Array

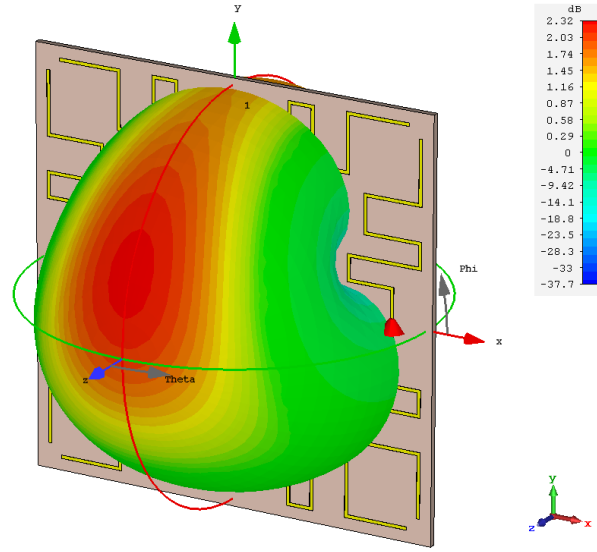


Figure 3.11: 3D gain pattern of dipole 1 for the optimum dipole distance $d = \lambda/4.3$. Identical gain patterns pertain to the other three dipoles, with a 90 degrees rotation along φ .

Fig. 3.10 displays the gain patterns of dipole 1 (see Fig. 3.9), where the influence due to the mutual coupling with the other dipoles can be observed. Identical gain patterns pertain to the other three dipoles, with a 90 degrees rotation along φ . The distance $\lambda/4.3$, corresponding to 80 mm, has been chosen as optimal, providing the maximum gain in both the $\theta = 0^\circ, 180^\circ$ (broadside) directions and the $\theta = 90^\circ$ (lateral) direction, equal to 2.1 and 1.7 dBi, respectively. The radiation efficiency is in this case equal to 96%. For easiness of visualization, the 3D gain pattern of dipole 1 is also reported in Fig. 3.11. In this way the mutual coupling among the dipoles at the optimum distance increases their directivity in the broadside and respective lateral directions. The topological combination of the four elements leads to an overall quasi-isotropic behavior, with no radiation nulls in any direction. This result is of paramount importance in RF energy harvesting applications, as it leads to the highest power being collected for any given orientation with respect to the RF source.

3.3. Four Dipoles Rectenna Array

At this point, though, it is important to observe that, due to the strong inter-antenna coupling, the single dipole-element impedance becomes useless for quantifying the true amount of RF power received by each dipole and the actual coupling mechanism (in the near-field) among the dipole antennas ports has to be used. Moreover, it is noteworthy that such quantities vary with the reciprocal orientation between the RF source and the dipoles system [157]. This can be obtained by means of the reciprocity theorem, under the assumption of a uniform plane wave incident on the dipoles system, with a procedure equivalent to the one described in Section 1.5.2. In this way the Norton equivalent sources of the dipoles system four-port network can be derived for any possible combination of the RF excitation and of the dipoles system orientation. To do so the four-port admittance matrix of the dipoles system computed by EM simulation is used in place of the scalar one representing each stand-alone dipole. This does have a significant impact on the system description as can be seen from Fig. 3.12(a), where the real and imaginary part of the self-admittance parameters Y_{ii} are compared with the corresponding quantities computed for a standalone dipole. Fig. 3.12(b) shows the trans-admittance behavior in the same conditions. Finally, regarding the spiral antenna, its behavior is not influenced by the UHF dipoles location and it provides a maximum gain in the broadside direction, ranging from 3 to 6 dBi over the UWB band and with a constant radiation efficiency of 97%.

Each dipole of Fig. 3.9 is connected to a rectifying section by means of a π -matching network. This way, four distinct rectennas are integrated on the same device. In order to provide a unique dc output, a dc-series connection is realized, therefore maximizing the overall output voltage. A schematic of each rectifying section and of their correspond-

3.3. Four Dipoles Rectenna Array

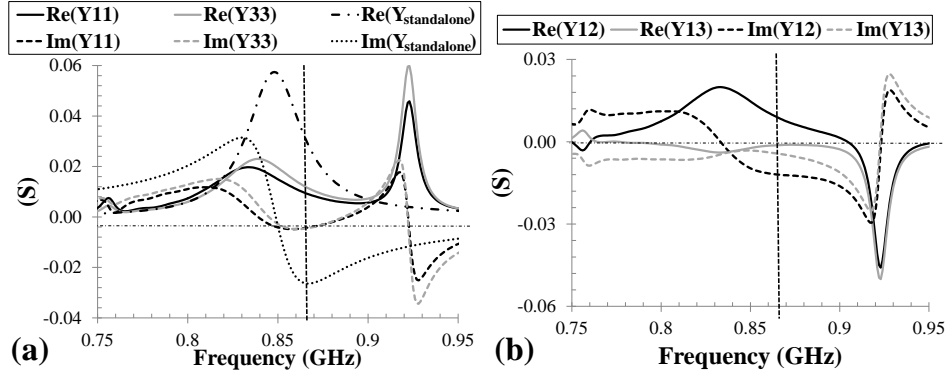


Figure 3.12: Near-field behavior in terms of (a) self-admittances and stand-alone dipole admittance, (b) trans-admittances.

ing connection is given in Fig. 3.13, where UHF power from each dipole is represented as an ac voltage source with the antenna impedance as series resistance. It is possible to observe that the capacitive divider for the WUR output is implemented only in the first stage; indeed, for the present system it is possible to choose the most suitable polarization at the transmitter side and in this case a CP has been adopted for the transmitting UHF antenna. In addition, a single WUR stage is enough, thanks to the extremely low requirements of the WUR [121]. Nevertheless, the system could be straightforwardly adapted to the case of unknown radiating sources by simply providing a capacitive division at the second stage, too. In this way dual-linear polarization functionalities can be guaranteed as well for the WUR signal.

A full-wave rectifier topology is adopted in each stage, where Schottky diodes are the Skyworks SMS7630-079LF. Values of the optimized network are given in Table 3.3, while Fig. 3.14 reports the final tag layout on Rogers RO4350B substrate.

Validation experiments of the described tag, unfortunately, did not provide good agreement with the predicted results. Indeed, the measured dc values obtained at the tag output were lower than expected.

3.3. Four Dipoles Rectenna Array

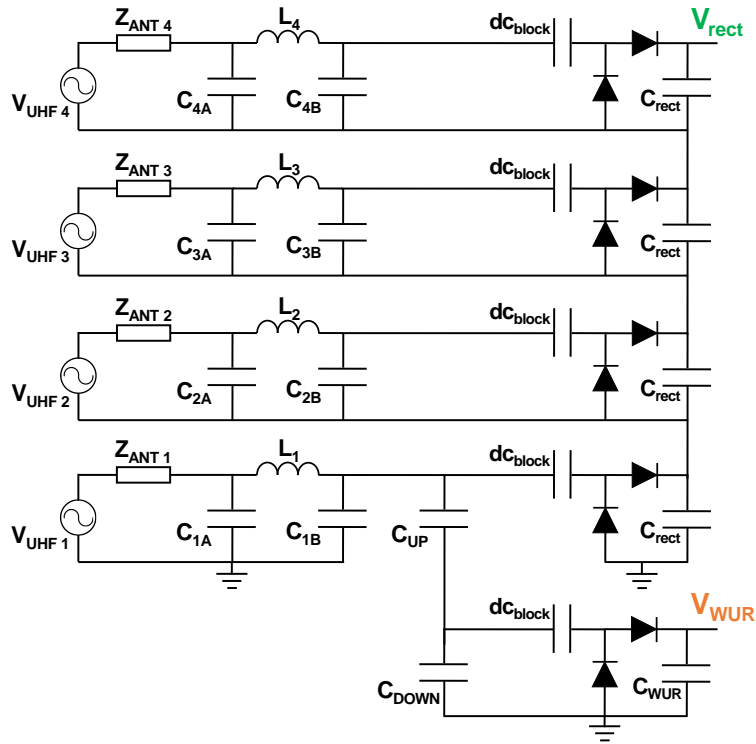


Figure 3.13: Topology of the multi-rectenna series dc connection. Each stage number corresponds to the respective dipole of Fig. 3.9. Matching networks of stages 2 to 4 are identical, while the first stage is optimized for the provisioning of the additional WUR output.

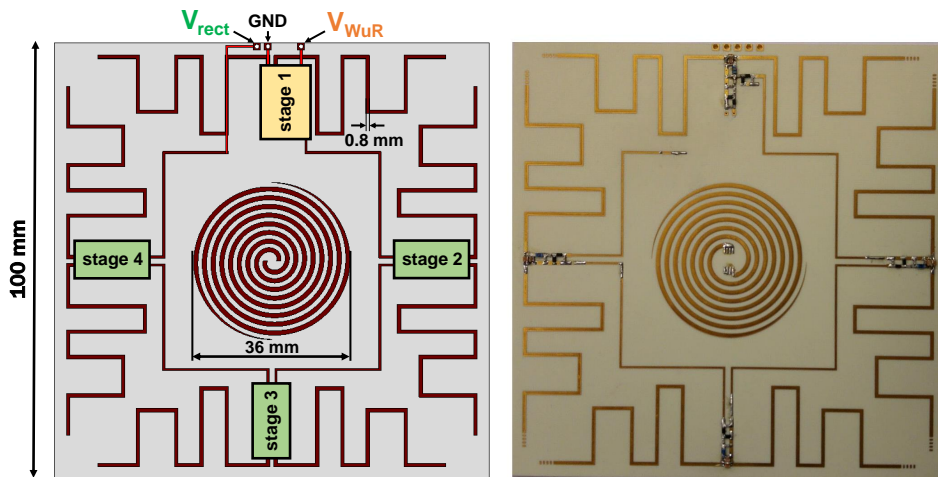


Figure 3.14: Representation of the final layout and picture of the four-rectenna array prototype. Red lines on the left image represent metalizations on the bottom side of the PCB.

3.3. Four Dipoles Rectenna Array

Table 3.3: List of SMD components of the four-dipole rectenna array.

Part name	Manufacturer	Product code	Value
L_1	Coilcraft	0603HP-22NXGLW	22 nH
$L_2 = L_3 = L_4$	Coilcraft	0603HP-23NXGLW	23 nH
C_{1A}	Murata	GJM1555C1H150FB01D	15 pF
C_{1B}	Murata	GJM1555C1HR50WB01	0.5 pF
$C_{2A} = C_{3A} = C_{4A}$	Murata	GJM1555C1H9R5BB01D	9.5 pF
$C_{2B} = C_{3B} = C_{4B}$	Murata	GJM1555C1H1R2WB01D	1.2 pF
C_{UP}	Murata	GJM1555C1HR90WB01D	0.9 pF
C_{DOWN}	Murata	GJM1555C1H1R7WB01D	1.7 pF
$d_{c_{block}}$	ATC	600L100FT200T	10 pF
diodes	Skyworks	SMS7630-079LF	
C_{rect}	Murata	GJM1555C1H390JB01D	39 pF
C_{WUR}	Murata	GJM1555C1H100FB01	10 pF

3.3. Four Dipoles Rectenna Array

Table 3.4: OC rectified voltage comparison of the presented harvesters.

Available RF power	Monopole Rectenna	Four-rectenna Array
- 16 dBm	0.7 V	1.2 V
- 11 dBm	1.25 V	2.1 V
- 6 dBm	2.3 V	3.9 V

Representative results in terms of OC rectified voltage are reported in Table 3.4, where the corresponding results of the monopole rectenna of Section 3.2 are also reported for comparison. The available RF power at the input of the rectenna is calculated by means of the reciprocity theorem as previously explained. For equivalent RF power, the four-element rectenna array is able to provide an increase of the OC voltage of about 70% with respect to the single rectenna case. Nevertheless, though, the corresponding optimum load value at the series-connected rectifiers output assumes an increase value of 33 k Ω , therefore the resulting overall dc power is slightly lower than the one provided by the monopole rectenna. These results can be justified by the consistent mutual coupling emerged from the tight integration among the array elements. This coupling result in RF contributions received by each rectification stage not exclusively coming from the UHF source, but also due to the inter-exchange of power among the antennas. Since this last phenomenon is uncontrolled, these power exchanges are able to sum to each other with discording phases, resulting in destructive contributions. Moreover, part of these signals can also end up being re-radiated by the antennas, entailing an additional power loss. This outcome justifies the imperative necessity of resorting to a more accurate design when dealing with multi-rectenna array implementation, with the goal of better controlling the resulting RF mutual influence among the array elements.

3.4 Two Monopoles Rectenna Array

Due to the extreme close proximity of the antenna array elements, the occurred RF coupling of the antennas ports resulted to be too strong and a performance degradation with respect to the EM simulation-based results has been observed. The near-field elements coupling causes an uncontrolled exchange of signals (since the phases of the received waves are uncontrolled), causing a portion of the coupled power to be re-radiated instead of being converted to dc, as well as possible destructive signal summations. Therefore, if not properly controlled, this mutual influence results in significant variations of the dc rectenna outputs [158].

These results indicate that, even if the array elements are dc-connected, a proper interface among the antennas should be designed as well at the radiofrequency level, this way providing independent RF contributions with a suitable control over signal phases [159, 160, 161]. To this extent, a possible solution can be represented by designing an RF decoupling network between the array elements [162]. This solution has been adopted for the present tag design. In order to better control the decoupling between the array elements a two-element array has been adopted in this case, involving two monopole antennas. The proposed circuit schematic of this new two monopole rectenna array is reported in Fig. 3.15.

The antenna near-field behavior is considered by means of the 2-port S matrix obtained by EM simulation and the UHF incident power on each dipole is represented with an ac current source at each port input. The implemented decoupling network is composed of two parallel lumped elements and two couples of series ones, realized with SMD components, whose values are detailed in Table 3.5. This network is also responsible to provide proper matching conditions between the an-

3.4. Two Monopoles Rectenna Array

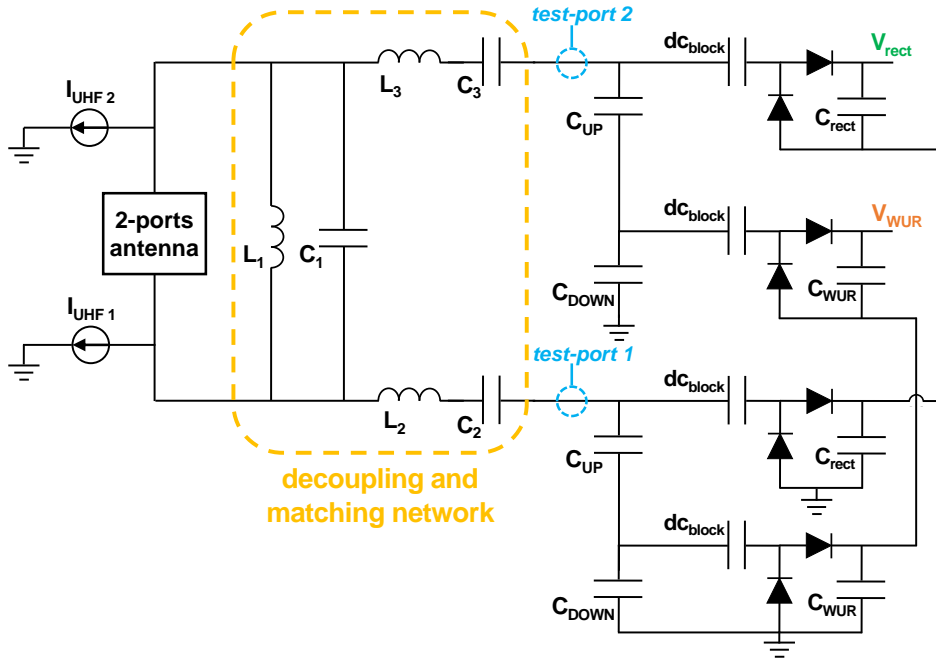


Figure 3.15: Circuit schematic of the two-monopole rectenna array with decoupling network.

tennas and the rectifying sections. In this case the WUR is implemented at both stages, still exploiting the capacitive divider solution. It is also possible to see that series dc connection has been realized for both the rectifier and the WUR.

A picture of the realized prototype, realized on a 1.5-mm-thick Rogers RO4350B substrate ($\epsilon_r = 3.48$, $\tan(\delta) = 0.0037$ at 10 GHz), is reported in Fig. 3.16, with the corresponding dimensions. As seen from the figure, this layout has been realized in view of a direct integration with the electronic components on the same PCB. The inclusion of a miniaturized UWB chip antenna is also foreseen in the space left between the two monopoles (a proper soldering pattern is realized in this case on the backside of the PCB).

For a proper design of the decoupling/matching circuitry, the network has been first optimized by means of linear simulations, assuming a reference value for the rectifying sections input impedance of $9 - j150\Omega$,

3.4. Two Monopoles Rectenna Array

Table 3.5: List of SMD components of the two-monopole rectenna array.

Part name	Manufacturer	Product code	Value
L_1	Coilcraft	0603HP-56NXGLU	56 nH
C_1	Murata	GJM1555C1H2R8WB01D	2.8 pF
$L_2 = L_3$	Coilcraft	0603HP-27NXGLU	27 nH
$C_2 = C_3$	Murata	GJM1555C1H390JB01D	39 pF
C_{UP}	Murata	GJM1555C1HR70WB01D	0.7 pF
C_{DOWN}	Murata	GJM1555C1H1R0WB01D	1 pF
d_{cblock}	ATC	600L100FT200T	10 pF
diodes	Skyworks	SMS7630-079LF	
C_{rect}	Murata	GJM1555C1H100FB01	10 pF
C_{WUR}	Murata	GJM1555C1H100FB01	10 pF

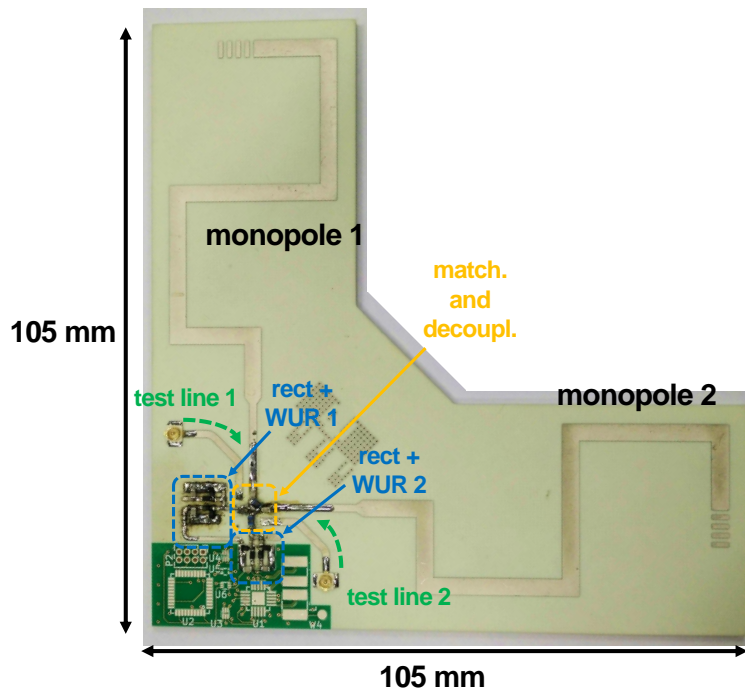


Figure 3.16: Picture of the realized two-monopole prototype. The bottom-left part of the tag, containing a green solder mask, is designed for integration of the electronic components.

3.4. Two Monopoles Rectenna Array

in correspondence of the two test ports inserted in the schematic of Fig. 3.15. Indeed, this number was found as impedance at the capacitive divider input, loaded by the corresponding rectifiers, for a fixed RF power level of -13 dBm. This value was chosen as a reference since it is the power quantity at which PMU requirements were satisfied by the single monopole rectenna. Obviously this is a power-dependent optimization, which is only valid for a given RF power level of the nonlinear circuitry. Therefore the matching conditions, and consequently the conversion efficiency, can be degraded for slightly different impedances offered by the rectifying section at higher power levels. Nevertheless, in these conditions the higher received RF power compensates the degradation of the conversion efficiency and the dc power output is still capable of satisfying the PMU requirements.

The modeled matching and decoupling behavior of the optimized network are reported in Fig. 3.17 in terms of scattering parameters, where port 1 and port 2 are the corresponding test ports of Fig. 3.15, normalized on $9 - j150\Omega$. The matching and decoupling conditions at the UHF 868 MHz frequency are clearly observed. The test lines visible in Fig. 3.16 are then exploited for the evaluation of the equivalent measured performance. The results are superimposed in Fig. 3.17, where the S parameters obtained with a VNA measurement at the two test ports are reported after a proper de-embedding of the test lines [114] and a re-normalization on $9 - j150\Omega$. A quite good agreement is obtained between simulated and measured data, despite for a small decrease in the measured decoupling.

In order to evaluate the overall rectenna performance, the rectified outputs are finally measured for different distances from a UHF transmitter emitting the maximum value of 2 W ERP and are compared to

3.4. Two Monopoles Rectenna Array

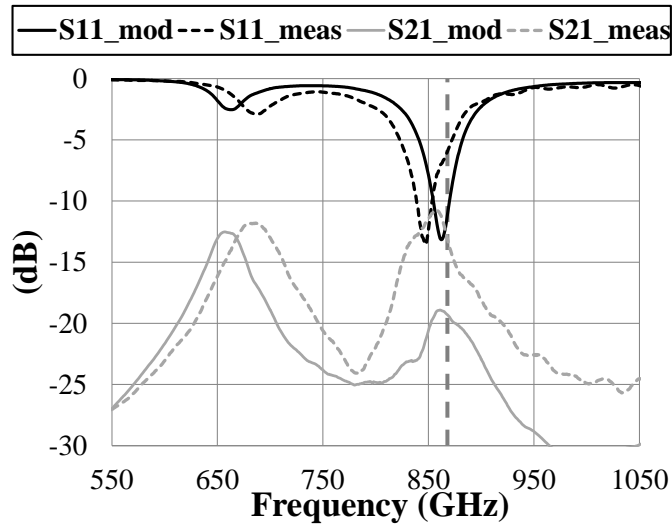


Figure 3.17: Comparison between the measured and modeled insertion and return loss at the two test ports, in correspondence of the interface between the decoupling network and the two rectifying sections.

the ones reached by the corresponding monopole rectenna. In this final evaluation, a CP transmitting antenna is adopted, which introduces a 3 dB polarization mismatching. This choice however allows a less stringent system operation, since tags should be able to rotate freely, without being restricted to predefined orientation positions. The results are reported in Fig. 3.18. It is possible to observe that this time the new rectenna array provides a positive increase in terms of both voltage and power dc outputs. The obtained rectified power is more than two times the one provided by the single monopole rectenna, while the rectified voltage is almost twice that reached by the single monopole. These excellent results confirm the effectiveness of the decoupling implemented between the array elements and provide an acceptable constant satisfaction of the PMU requirements for the high operation distances foreseen by the presented system.

3.5. Remarks and Future Developments

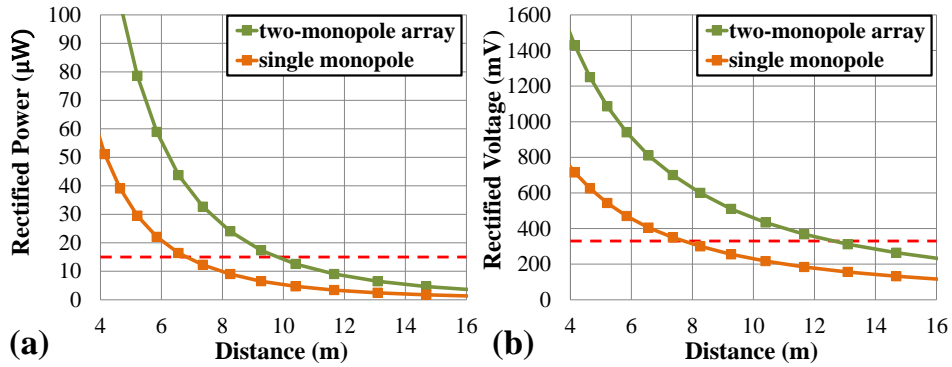


Figure 3.18: Comparison between measured (a) dc power and (b) dc voltage for the single monopole and the two-monopole array rectennas for different distances from a CP UHF source, transmitting 2 W ERP. PMU requirements are highlighted in red. The optimum load for the two-monopole array is equal to 15 k Ω .

3.5 Remarks and Future Developments

The described architectures propose the combination of UWB and UHF technologies for the implementation of energy-autonomous tags, capable of high accuracy localization. The demand for increased reading ranges, possibly leading to context-aware innovative market applications featuring zero-power IoT tags, motivated the investigation of new solutions in the tag design, for increasing the dc outputs of the rectenna unit. The first solution, involving a four-element rectenna-array, proposes a quasi-isotropic energy harvester, with all-polarization receiving capabilities, both essential features in real harvesting applications. Nevertheless, the unavoidable coupling between the antennas motivates a more elaborated design approach, which thoroughly considers the mutual influence of the rectenna-array elements. A second solution is therefore provided, successfully satisfying the demanded decoupling requirements. The obtained results show that the new two-rectennas array guarantees and increased performance in terms of rectenna dc output power of almost two times the one obtained with the corresponding standalone rectenna.

Chapter 4

Low-Cost UHF Near-Field Contactless Solution for RFID Applications

Wireless power transmission in the far-field region has many potential applications, especially for low power devices and sensors and is envisioned as key enabler for a pervasive deployment of the Internet of Things. However, when dealing with consumer electronics, or more in general with applications where power transfer efficiency and safety become the main concerns, for the time being near-field WPT finds more room for adoption, thanks to its inherent advantages. Indeed, contrary to the far-field case, where transmission of energy is obtained through electromagnetic propagation, in near-field WPT the exchange of energy takes place by means of electric or magnetic coupling, with no fields being propagated outside the proximity of the WPT system [20, 163, 164].

The non-radiative exchange of energy in the near-field can be categorized into three main groups, depending on the adopted type of coupling technique: (i) inductive coupling, (ii) magnetic resonant coupling and

4.1. WPT for RFID Applications

(iii) capacitive coupling. The first kind of near-field coupling takes place by induction of a magnetic field from a primary coil to a secondary coil [16, 15, 165], which is essentially based on the same working principle of an electrical transformer. Magnetic resonant coupling can be considered to some extent an evolution of the inductive coupling mechanism: in this case the primary and secondary are tuned in resonance by adding compensation capacitors, so that the two resonators become coupled at the same resonance frequency [166, 167, 168]. Finally, the third kind of near-field WPT is realized by the exchange of electric field between two adjacent capacitors [169, 170, 171], also in this case a resonant condition can be realized by implementing compensation inductors [172]. The first two mechanism of near-field WPT are often identified as inductive power transfer (IPT), while the last one is also referred to as capacitive power transfer (CPT).

Each implementation has its own advantages and disadvantages, nevertheless a common factor combines the majority of the well-known solutions so far: in almost all cases, the operating frequency is in the range from LF (30-300 kHz) to HF (3-30 MHz), while very few solutions have been proposed at UHF or microwave frequencies [27, 173]. In this Chapter a near-field WPT system is presented, envisioned for, but not limited to, low-cost RFID applications in the European UHF 868 MHz band.

4.1 WPT for RFID Applications

RFID technology is a very well-know technique, which has been deeply investigated in the last decades [174, 175, 176, 177] and since then became a pervasive technology in everyday life. Its applications span a high number of different scenarios, such as logistics and supply chain, item-level inventory tracking, access control, mobile healthcare, distributed

4.1. WPT for RFID Applications

sensor networks and real time locating systems (RTLS). A key feature demanded in the vast majority of cases is the necessity for very low-cost materials and manufacturing techniques, both deemed important requirements for the effective mass deployment of RFID technology in market applications [178].

A representative example of UHF RFID application can be the coverage of shelves for inventory tracking, featuring highly stacked items. Such scenarios typically require hundreds of meters of shelves to be covered with RFID readers, compliant with the maximum EIRP emission [75], so that every item falls within the reading range of the readers. In order to decrease the system costs, the reader units, which represent the expensive part of the RFID system [47], tend to be kept at the minimum possible number. For this reason in many cases one single reader unit is connected to different antennas by means of a multiplexer or similar kind of splitters and the RF signal is typically propagated to the radiating units by means of coaxial cables of different lengths. Depending on the application scenario, the radiating units can have to be placed at a very close distance (e.g., half a meter) and in a quite high number in order to guarantee an acceptable coverage. Covering hundreds of meters of shelves with such techniques results in a considerable cost, not only for the consistent amount of required RF coaxial cables, but also in terms of installation. Moreover, this large number of antennas should also be able to be periodically replaced, for maintenance or upgrade needs.

In such a context, the possibility to replace physical connections between hardware components with contactless techniques using inexpensive materials and featuring high repeatability is very attractive and enabling for large-scale adoption. Fig. 4.1 depicts a schematic representation of a possible architecture, where the signal of the main cen-

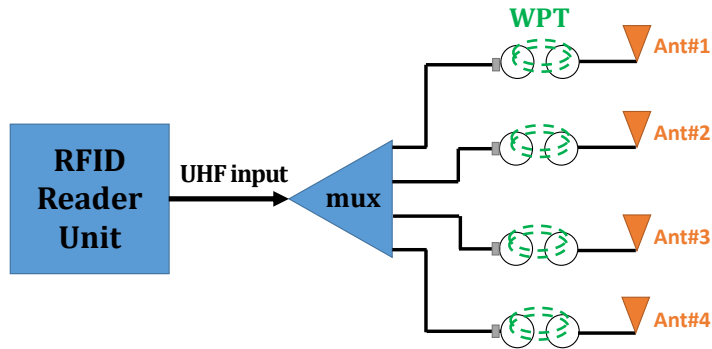


Figure 4.1: Schematic representation of a contactless connection between the RFID reader processing unit and the reader antennas.

tralized reader unit is divided among different paths and is fed to several distributed reader antennas with no need for connectors, allowing a straightforward and easy antenna removal or replacing. Such migration could be performed in a seamless fashion taking advantage of near-field wireless power transmission capabilities. Nevertheless most implementations of this kind take place at the underlying low and high frequencies, while from the RFID point of view, the simplest and less expensive choice would be realizing near-field coupling at the same frequency of operation of the UHF RFID communication, with no need for additional frequency conversion modules.

Recently a method for near-field coupling at UHF has been proposed [179, 180]. This solution exploits the resonant behavior of an optimized defected ground structure to create a near-field coupling between two closely spaced resonators. This method is adopted and further developed for a low-cost implementation, envisioned for RFID applications in the European UHF 868 MHz band.

4.1.1 DGS Resonators

Defected ground structures (DGSs) can be considered as an evolution of photonic band gap (PBG) structures, i.e. periodic structures specifically

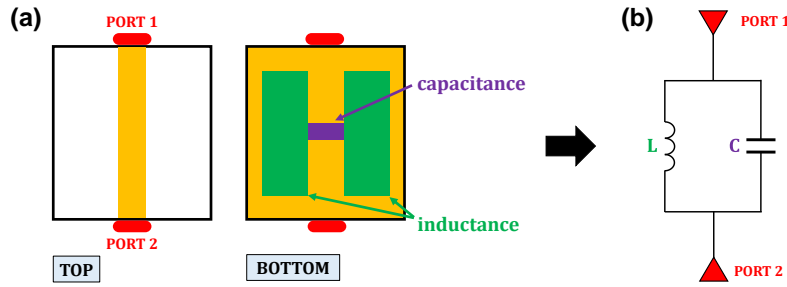


Figure 4.2: (a) H-shaped DGS, where the capacitive and inductive areas of the deflection are highlighted and (b) equivalent circuit representation.

designed in a way that propagation of certain frequency bands is prohibited [181, 182]. As a general definition, a DGS basically consists in a section of microstrip line which presents a removal, or deflection, in the ground plane, with a specific size and shape. Such deflection introduces a perturbation of the current distribution in the ground plane, which results in modifications of the transmission line capacitance and inductance [183]. Thanks to the quasi-lumped LC resonant circuit behavior of the defected section, DGSs have been widely investigated in the last years for the implementation of band-stop and band-pass planar filters [184, 185, 186, 187, 188].

The resonance behavior of the DGS was recently proposed as a building block for wireless power transmission applications [179, 180]. Indeed, by placing two resonant DGSs next to each other, power can be transmitted wirelessly, similarly to what is done in any near-field WPT resonant link, but with the main advantage of providing a WPT link at UHF frequencies, exploiting the particular structure of the DGS to overcome the usual limitation of the increased radiation resistance and losses of inductors at higher frequencies [189].

A H-shaped DGS can be modeled as a parallel LC resonator [183, 184, 190], as schematically represented in Fig. 4.2, where the inductance contribution mainly comes from the wider etching in the ground plane

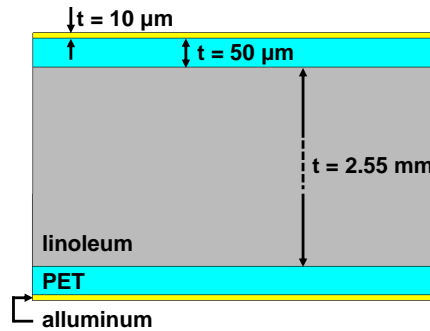


Figure 4.3: Multilayer substrate representation. Two PET layers with printed conductive aluminum are employed as top and bottom metalization, linoleum is used as main dielectric substrate.

and the capacitive one from the center facing metalized strips. By means of quasi-static modeling [191] it is possible to identify a relationship among the DGS dimensions and the values of the circuit equivalent representation [180], which can be exploited for the initial design of the DGS.

4.1.2 Low-Cost Materials

A requirement of paramount importance in RFID systems is a low-cost implementation. This poses strict constraints on the materials choice, which have to be available at a very low-cost, but also on the manufacturing costs: adopting cheap materials that require labored and/or expensive machining is still not acceptable in most cases. Finally, the final products should be designed in such a way that their deployment in the intended working environment can be achieved smoothly and easily, reducing also the deployment costs. A second feature that is of increasing importance in many emerging applications is flexibility in the structure, in order to be conformable with non-planar surfaces. The choice of material should be based on these two requirements.

For this purpose thin polyethylene terephthalate (PET), which is flexible, low-cost and widely adopted in RFID systems, especially for

4.2. WPT Implementation

tags realization [177, 192, 193, 194, 195], is a good candidate. Nevertheless, it is suitable as a supporting material for printing antennas, but it is usually too thin to be adopted as the sole substrate for microstrip lines and microstrip antennas. In order to provide the convenient thickness, linoleum, a very cheap, flexible material widely used for floor covering, though not directly suitable for RF applications, can be adopted as a further supporting medium besides the PET. The combination of these two materials offers a very cheap solution that can be effectively adopted for practical applications. In order to obtain accurate modeling of the structure, the electrical properties of the two materials are measured by means of a standard resonant cavity method with a Damaskos Model 08 Thin Sheet Tester. The electrical properties are found to be $\epsilon_r = 3.2$, $\tan(\delta) = 0.003$ (at 1 GHz) and $\epsilon_r = 1.89$, $\tan(\delta) = 0.011$ (at 1 GHz) for PET and linoleum, respectively. By superimposing the materials, microstrip lines and antennas can be created: a schematic representation of a possible multilayer low-cost substrate adopted for the present design is reported in Fig. 4.3. Printed aluminum on PET is employed for the metallic layers, while linoleum acts as main dielectric substrate. The three layers can be simply superimposed on top of each other, without any extra glue or fixing material.

4.2 WPT Implementation

The presented multilayer substrate is adopted for the design of H-shaped DGSs to be used as resonators for near-field UHF WPT. As a first step the microstrip line is truncated, acting as an open circuit stub, which from the circuital point of view can be modeled as an additional series capacitance. The stub length can therefore also be tuned to regulate the resonant frequency and for matching purposes. As opposed to [180],

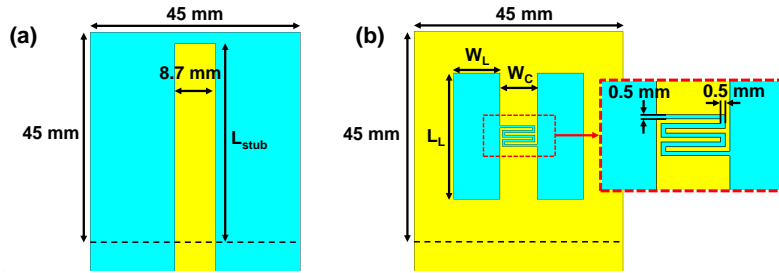


Figure 4.4: Schematic representation of the designed DGS: (a) top view, where the line width is set for a 50Ω characteristic impedance and (b) bottom view, showing the interdigital capacitor. The bottom dotted black line marks the DGS section, at the far end of the multilayer microstrip line.

where the needed value of capacitance is reached by adding a lumped SMD capacitor in parallel to the one offered by the DGS, for the present design SMD components are avoided and an interdigital capacitor is implemented to simplify the manufacturing and to lower the overall costs. In this way all metallic structures are planar and can be directly printed on a PET substrate. A 2D representation of the presented H-shaped DGS is reported in Fig. 4.4, together with the relative parametric dimensions.

For an effective implementation in real scenarios, the evaluation of the impact of surrounding materials which are placed nearby the resonating structure has to be carried out. The strip line of the structure reported in [180] is facing the supporting material. So, placing the whole structure onto any material other than air will deeply affect its behavior. Indeed, either the effective dielectric constant of the bottom microstrip will change or it will become a stripline if it is placed on top of a metallic surface. To overcome this limitation, the bottom microstrip line is flipped over such that the ground plane is facing the supporting material: the effect of the latter is restricted to the area of the DGS, due to the partial metal removals in the ground plane. This way, the effect of different materials used as support has to be evaluated only in this

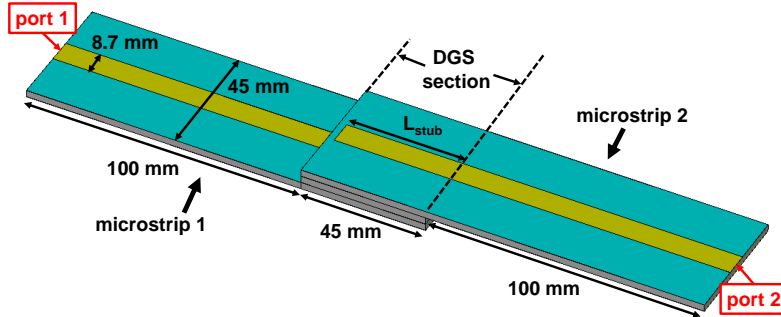


Figure 4.5: Perspective view of the two microstrip lines ending/beginning with the DGS section. One layer of linoleum is placed as spacer between the two DGSs.

region. A 3D representation of the near-field WPT system is depicted in Fig. 4.5.

4.2.1 DGS Parametric Study

The multilayer substrate described in the previous Sections is chosen for the investigation of the near-field coupling performance between the two closely spaced resonators. By tuning the dimensions of the structure, a parametric study is conducted with electromagnetic simulations, using CST Microwave Studio [76]. As a first step, the dimensions of the interdigital capacitor are found in order to provide a fixed capacitance of approximately 1 pF [196]. Secondly, the other dimensions reported in Fig. 4.4 are tuned in order to highlight their impact on the inductive behavior of the DGS and therefore on the operating frequency. Fig. 4.6 illustrates some results reporting the impact of the parameters L_L , W_L and W_C on the resonant frequency. One parameter is changed at a time while keeping the other two fixed. From these results, it is possible to notice that L_L has a smaller impact, it produces a shift of approximately 10-15 MHz/mm, and it is therefore suitable for fine tuning of the resonant frequency. W_L and W_C have a greater influence, introducing shifts of about 35-40 MHz/mm. The modification of W_L is preferred since the

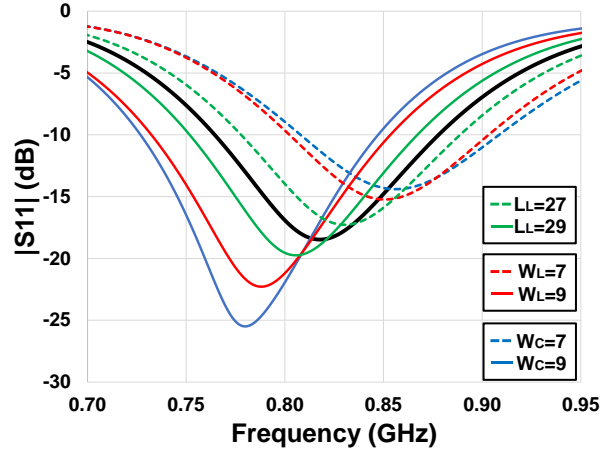


Figure 4.6: Tuning of the resonant frequency obtained by varying the significant parameters of the DGS. The black curve represents the reference starting point, obtained for $L_L = 28 \text{ mm}$, $W_L = 8 \text{ mm}$ and $W_C = 8 \text{ mm}$.

latter parameter influences also the interdigital capacitor. During these tuning the length of the stubs, L_{stub} , is kept fixed to 20 mm.

The second significant design parameter is the distance between the two resonators. It is well known in near-field resonant WPT applications that by changing the distance between the two resonators a frequency separation of the two resonances is produced [197, 198]. Even though a possible method for obtaining constant power transfer even in case of varying distances has been recently proposed [199], for the present application a constant distance is foreseen throughout the whole operation of power transfer and can therefore be chosen a priori. Such phenomenon of frequency bifurcation is graphically described in Fig. 4.7, where the simulated performance of the near-field coupling is reported for different values of distance. For a real physical implementation of the structure, the material used as spacer between the two resonators cannot simply be free space but necessarily has to be a physical medium. Hence, to comply with the low-cost requirements, the same linoleum material already used is employed as spacer.

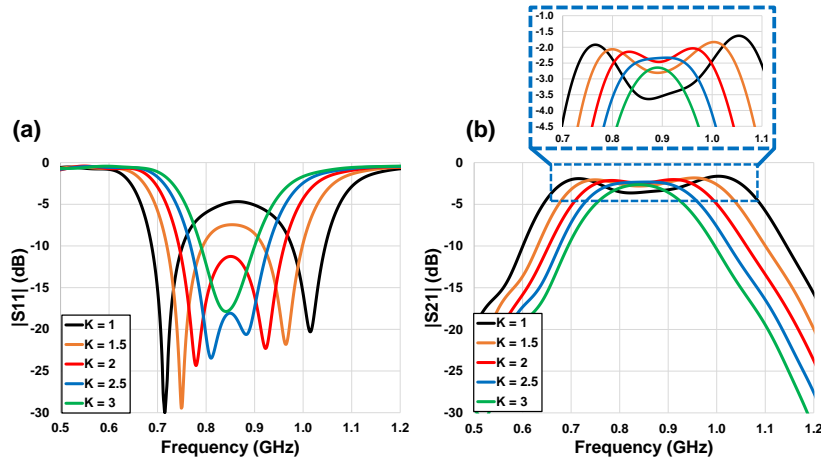


Figure 4.7: Effect of the varying distance between the two DGSs in terms of number of linoleum layers, K , placed as spacer between the two. One layer of linoleum has a thickness of 2.55 mm, in accordance with Fig. 4.3. DGS dimensions are in this case $L_L = 27\text{ mm}$, $W_L = 8\text{ mm}$, $W_C = 8\text{ mm}$ and $L_{stub} = 18\text{ mm}$. (a) Reflection coefficient and (b) transmission coefficient.

It is interesting to notice from the results of Fig. 4.7 that, even though the optimum distance is given by $K=3$, which provides a single, wide operating bandwidth, the maximum transmission value is obtained for $K=1$, which is therefore chosen for the present design, even though this entails a doubling of the operating bands. The 0.5-1 dB drop of the transmission coefficient for higher values of K can be explained by the increased quantity of lossy materials inserted between the two resonators. Even if it is reduced, the operating bandwidth obtained is still well suitable for applications in the European 868 MHz band. Obviously, in case a higher bandwidth would be required, for example for coverage of other RFID frequency bands, the optimum distance could be chosen, at the expense of a slight reduction of the transmission coefficient. To this extent, a second prototype is also implemented, with $K=3$, in order to test also the feasibility of the wider bandwidth solution.

4.2. WPT Implementation

Table 4.1: List of realized prototypes.

	L_L (mm)	W_L (mm)	W_C (mm)	L_{stub} (mm)	N. of layers (K) as spacer	Type of material
Proto 1	26	6	7	18	1	non-metallic
Proto 2	28	9	8	14	3	non-metallic
Proto 3	27	10	11	14	1	metallic

4.2.2 Experimental Validation on Different Materials

Based on the previously described considerations, three different prototypes of the proposed system were realized and measured. For a practical implementation, it is extremely important to evaluate the effect of the materials surrounding the DGS section, specifically the physical support on which the coupling structure is placed during operation. In this Section, the effects of plastic and wood materials are first considered as they have the same influence on the coupling structure. In a second step, metallic material is also assessed, estimated as the most influencing yet widely adopted medium for a vast number of applications.

Since $K=1$ is the distance which provides the best transmission coefficient, this has been chosen for both the metallic and non-metallic cases. In the latter, an additional prototype, with $K=3$, is also implemented and measured, to assess the wider bandwidth solution. Table 4.1 summarizes the three realized prototypes, together with the corresponding dimensions.

The pictures of the two measurement setups are reported in Fig. 4.8. In both cases, a single additional layer of linoleum is placed between the coupling structure and the physical support.

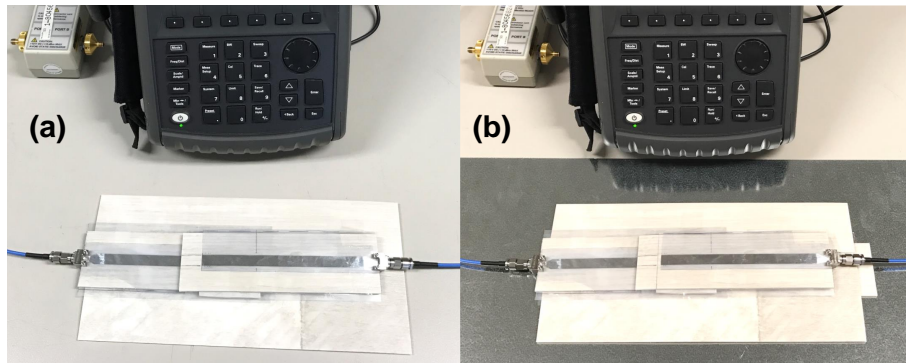


Figure 4.8: Pictures of the measurement setup on different material. (a) Non-metallic support. (b) Metallic support.

Non-Metallic Environment

The dimensions of the DGS are first optimized for the structure to be put over a plastic or wood material. For the first prototype, with $K=1$, the first of the two resonances of Fig. 4.7 is shifted in the UHF band. The values of the parameters are detailed in Table 4.1. Fig. 4.9 reports the behavior of the structure in terms of reflection and transmission coefficients. A good agreement is observed between measured and simulated data. The slight discrepancies are mainly due to realization tolerances and to small air-gaps inevitably present between the different layers of the adopted substrate, depicted in Fig. 4.3. Moreover, it is worth noting that a slight influence on the performance is also introduced by the bending of the second microstrip line, caused by the thickness of the linoleum layer introduced as spacer between the two resonators.

The second prototype, also optimized for use on non-metallic material, is chosen with three layers of linoleum as spacer between the two resonators, whose dimensions, optimized to have central resonance in the UHF band, are provided in Table 4.1. The corresponding reflection and transmission coefficients are reported in Fig. 4.10. A good agreement is observed in this case too, with the same considerations of

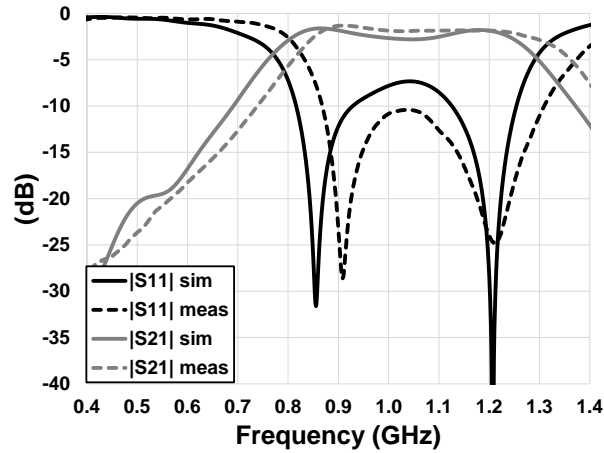


Figure 4.9: Comparison between simulated and measured reflection and transmission coefficients for the first prototype, over non-metallic material.

the first prototype. Both prototypes exhibit very good performance in terms of transmission coefficient, even though, as expected, prototype 1 reaches a maximum measured transmission coefficient of -1.3 dB, as opposed to the -2.6 dB obtained by prototype 2, at the expenses of a slightly reduced operating bandwidth.

Metallic Environment

In a large number of applications, the RFID operation has to take place in close proximity of metallic objects. This represents by far the worst possible scenario and it is therefore chosen as the second case study. Once again, the dimensions of the structure were optimized by EM simulations.

It is found that placing the resonating structure on top of a metallic surface exerts a significant influence on the behavior of the coupling. In particular, the presence of the metallic surface appears to have a detrimental effect mainly on the first of the two resonances of Fig. 4.7, canceling it, while the second resonance is only slightly affected. This effect is explained by the fact that the first resonance is mainly attributed

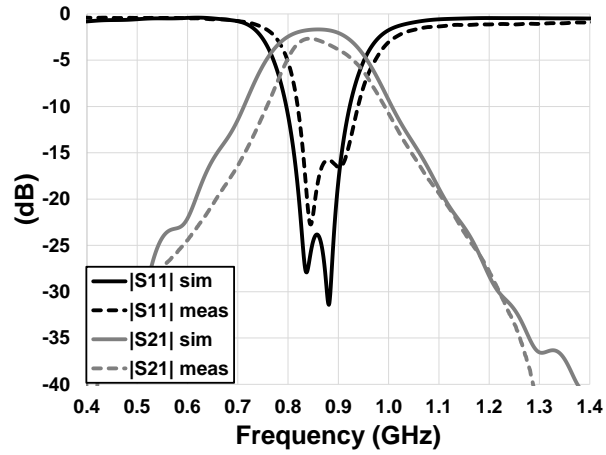


Figure 4.10: Comparison between simulated and measured reflection and transmission coefficients for the second prototype, over non-metallic material.

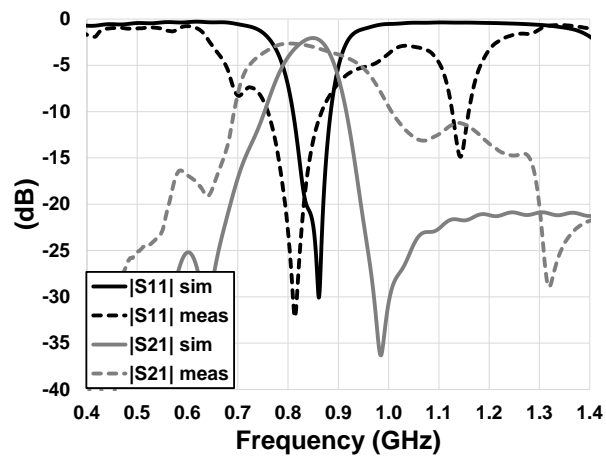


Figure 4.11: Comparison between simulated and measured reflection and transmission coefficients for the third prototype, over metallic material.

to the DGS closer to the metallic surface. The second resonance, conversely, mainly attributed to the further DGS, features only a slight frequency shift and a small degradation in the transmission coefficient. It is therefore chosen for the present design. A second prototype was realized by shifting the frequency of the second resonance to be centered at 868 MHz. The corresponding dimensions are given in Table 4.1 and comparison between the measured and simulated data is provided in Fig. 4.11. An acceptable agreement is obtained in this case, too, even though it is possible to observe a more adverse influence due to the presence of nearby metallic material.

4.3 RFID Reader Antenna

As previously discussed, the present design can be applied to a large number of applications, where the possibility of providing contactless coupling between two planar microstrip lines that need to operate at UHF sounds attractive. A possible implementation can be that of wireless connection between an RFID reader unit and its antenna. Indeed, there are a several number of cases in which the radiating element of an RFID reader needs to be replaced or modified in a certain way. Since these kinds of operations typically involve a very high number of units at a time, a contactless connection can result in a significant cost reduction with respect to a solution requiring physical connections. Moreover, its high repeatability can easily speed up the entire process.

4.3.1 Antenna Implementation

As a proof of concept, a UHF microstrip patch antenna is designed and realized on the same multilayer substrate of Fig. 4.3, it is then connected to the microstrip line corresponding to the second DGS of Fig. 4.5, in

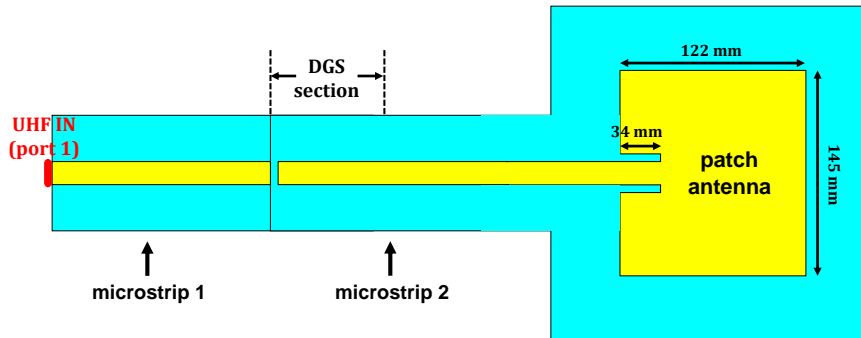


Figure 4.12: Schematic representation of a possible application for RFID antenna contactless feeding.

correspondence of the port 2 termination. The designed patch antenna is fed with an inset of 34 mm for impedance matching and it has a width and length of 145 and 122 mm, respectively. The dimensions of the DGS are the same as those employed for prototype 1, with $K=1$, except for the stubs which are in this case tuned to different lengths for matching purposes, since the loads of the two DGSs are different in the present case. In particular, the length of the stub fed by port 1 is fixed to 16 mm, while the length of the second stub, connected to the patch antenna, is chosen equal to 20 mm. A schematic representation of the patch antenna contactless feeding is reported in Fig. 4.12.

In the first place, the feasibility of the contactless antenna feeding is tested in terms of return loss at port 1. A comparison between the measured and modeled data is provided in Fig. 4.13. First, it is possible to notice the suppression of the second resonance, previously seen in Figs. 4.7-4.9, due to the loading of the second termination with the patch antenna, whose impedance is obviously frequency dependent. Second, it is possible to observe an excellent matching for the antenna, nevertheless exhibiting the usual frequency shift due to air-gaps.

The resonance is moved from the designed 868 MHz up to 915 MHz. Such shift finds theoretical justification by manually inserting in the EM

4.3. RFID Reader Antenna

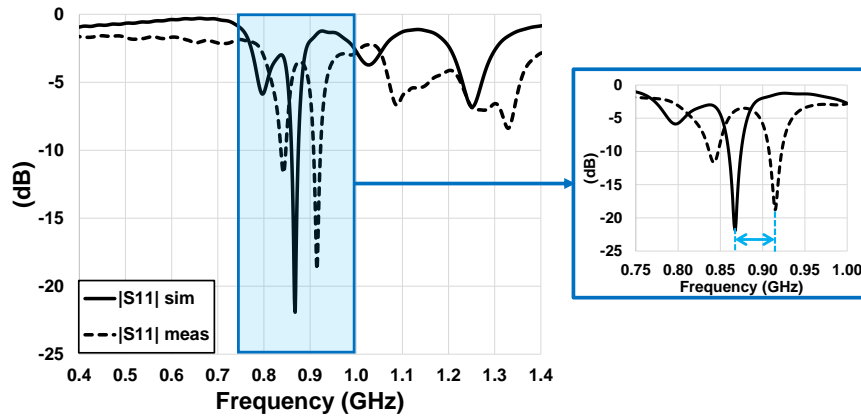


Figure 4.13: Comparison between the measured and simulated contactless fed patch antenna return loss. In the zoomed graph it is possible to observe the frequency shift due to air-gaps.

simulations a constant air-gap of about $130 \mu\text{m}$ among the layers of Fig. 4.3, value that can be reasonably expected, since the several layers are simply superimposed on top of each other.

From EM simulation, the system is expected to provide a maximum realized gain equal to 4.9 dBi and a radiation efficiency of 45%, values mainly limited by the employed lossy substrate.

In order to verify this performance, the contactless fed patch antenna is finally tested inside an anechoic chamber. A picture of the DUT is shown in Fig. 4.14. Given the frequency shift, observed in Fig. 4.13, the measurements in the anechoic chamber are performed in correspondence of the shifted resonance at 915 MHz. The measured gain patterns in both H- and E-plane are depicted in Fig. 4.15, superimposed to the modeled ones.

These measurements validate once again the excellent performance of the contactless fed antenna, with a measured maximum realized gain of 3.7 MHz.

4.3. RFID Reader Antenna

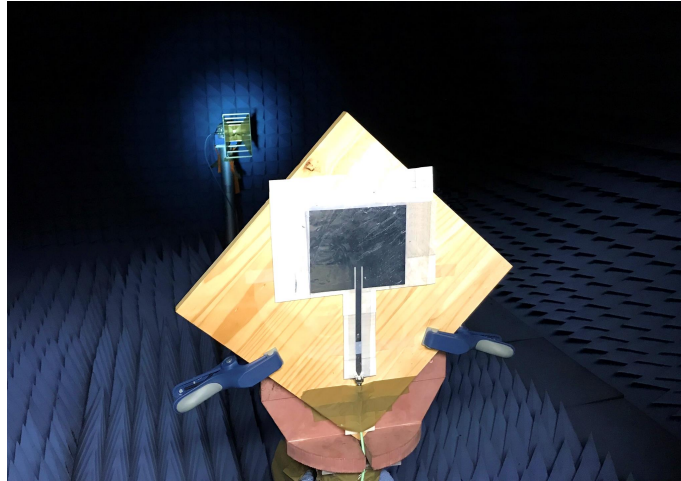


Figure 4.14: Picture of the realized contactless fed patch antenna prototype, tested in the anechoic chamber.

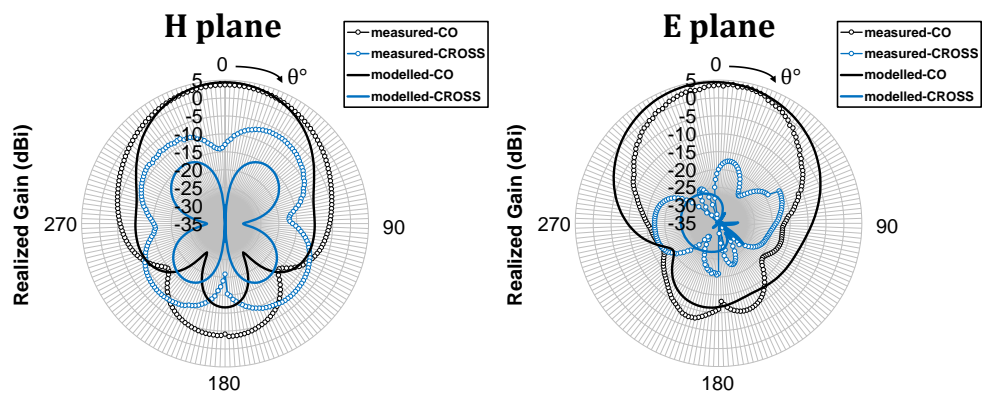


Figure 4.15: Measured and simulated gain patterns of the contactless fed microstrip patch antenna, in both H- and E-planes.

4.4 Remarks and Future Developments

The presented systems demonstrates a novel low-cost implementation for contactless near-field coupling between two resonating structure at UHF for European 868 MHz RFID applications. The effects of different nearby low-cost materials used as support for the resonant structure are evaluated and the EM design is confirmed by measurement results. The substrate and the power transfer technique used in the present study entitle the proposed system for wide deployment in mass market applications thanks to the very low cost and high repeatability. For future possible realization the possibility to print aluminum directly on linoleum (or similar materials) should be investigated, for example by means of the well-known techniques of inkjet printing [84, 200]. This would lead to the twofold advantage of increasing speed in the manufacturing and elimination of the air-gaps.

Conclusions

This doctoral thesis describes the main outcomes of the research activity conducted throughout the duration of the Ph.D. program. Some innovative solutions for wireless power transmission and radiofrequency energy harvesting were successfully achieved and have here been reported.

The system detailed in Chapter 1 illustrates the implementation of a novel, single-port, compact, low-profile tag, capable of hybrid UWB-UHF operations, with the goal of providing sensing, communication and high accuracy localization/tracking functions [50]. The miniaturized, eco-compatible architecture has dimensions suitable for current and future RFID applications. UWB technology, for accurate localization and communication, and a UHF rectenna, for efficient RF energy harvesting, can be exploited simultaneously thanks to the excellent performance provided by the diplexer network, both in terms of respective matching and strong decoupling between the two operating bands. The designed diplexer miniaturization exerts only minor influence on antenna performance and provides a final tag thickness lower than 1 mm. It is noteworthy that such influence can be totally overcome by future UWB-UHF integrated chip, to be directly connected in the inner part of the antenna

port. Numerical EM simulations have been validated by measurements, performed in real application scenarios, therefore proving the readiness of the tag for direct adoption in future RFID networks. The implementation on paper substrate guarantees eco-compatibility for more than 93% of the total tag volume, enabling the proposed solution for pervasive, massive market applications. Despite the non-negligible losses of the substrate, the antenna performances are fully compatible with UWB communication and UHF energy harvesting requirements. Nevertheless, exploitation of alternative recyclable materials, introducing lower losses (e.g., PET, fabrics), can be straightforwardly addressed by simply scaling the antenna layout. Consequently, the high performance, simultaneous data and power transfer capabilities, compact low-profile structure and eco-compatible material, recommend the proposed tag for next-generation UWB-based RFID systems.

The activity described in Chapter 3 can be considered a natural evolution of the first one. Where the combination of UWB and UHF technologies is still exploited for the implementation of energy-autonomous tags, featuring accurate localization. The demand for increased reading ranges motivated the investigation of new solutions in the tag design, for increasing the dc outputs of the rectenna unit. The first solution, involving a four-element rectenna-array, showcased a quasi-isotropic energy harvester, with all-polarization receiving capabilities, both essential features in real harvesting applications. Nevertheless, a consistent coupling between the antenna elements was observed, whose proper consideration is of paramount importance in rectenna-array design. A second solution is therefore provided, successfully satisfying decoupling requirements. The new two-rectennas array guarantees and increased performance in terms of rectenna dc output power of almost two times the one obtained

with the standalone rectenna.

Finally, Chapter 4 illustrates a new near-field wireless power transfer implementation, on planar low-cost substrate. Thanks to its high repeatability and very-low-cost deployment, the proposed system can be a possible candidate for mass market RFID applications.

Acknowledgements

Desidero innanzitutto ringraziare i miei relatori, Prof.ssa Alessandra Costanzo e Prof. Diego Masotti, per il loro supporto e per la loro guida in questo percorso di crescita degli ultimi anni.

Ringrazio la mia fidanzata (e a breve sposa) Jessica, per essermi sempre stata vicino. Mia madre Mariarosa, mio padre Lauro e mia sorella Alessandra, il cui sostegno non è mai mancato. Mia nonna Tilde e tutta la mia famiglia.

Ringrazio inoltre i compagni di avventure del laboratorio, i momenti difficili non sono mancati, ma il successo è stato superarli insieme.

Penso che non scorderò mai questa esperienza. Il cammino di questi anni mi ha permesso di crescere enormemente, sia dal punto di vista professionale che personale. Mi ha permesso di viaggiare, di apprezzare condizioni e situazioni culturali lontane dalla nostra, di vivere in prima persona nuove realtà. Opportunità spesso sottovalutate, ma che mi rendo conto non dovrebbero essere private a nessuno degli innumerevoli talenti italiani. Sperando che la consapevolezza del valore del Dottorato di Ricerca acquisti sempre più lo spazio che merita, ringrazio tutti quelli che hanno reso quest'esperienza possibile e così unica.

Grazie a tutti!

List of Achievements

Publications

Journals

1. M. Fantuzzi, D. Masotti, and A. Costanzo, "A Novel Integrated UWB-UHF One-Port Antenna for Localization and Energy Harvesting," *IEEE Trans. Antennas Propag.*, vol. 63, no. 9, pp. 3839-3848, Sept 2015.
2. V. Palazzi, M. D. Prete, and M. Fantuzzi, "Scavenging for Energy: A Rectenna Design for Wireless Energy Harvesting in UHF Mobile Telephony Bands," *IEEE Microw. Mag.*, vol. 18, no. 1, pp. 91-99, Jan 2017.
3. A. Costanzo, D. Masotti, M. Fantuzzi, and M. D. Prete, "Co-Design Strategies for Energy-Efficient UWB and UHF Wireless Systems," *IEEE Trans. Microw. Theory Techn.*, vol. 65, no. 5, pp. 1852-1863, May 2017.
4. A. Costanzo, D. Dardari, J. Aleksandravicius, N. Decarli, M. Del Prete, D. Fabbri, M. Fantuzzi, A. Guerra, D. Masotti, M. Pizzotti, and A. Romani, "Energy Autonomous UWB Localization," *IEEE J. Radio Freq. Identification*, vol. 1, no. 3, pp. 228-244, Sept. 2017.

Conference Papers

5. A. Costanzo, D. Masotti, P. Francia, and M. Fantuzzi, "Detection and movement estimation of items by a smart microwave handheld reader," in *2014 IEEE RFID Technology and Applications Conference (RFID-TA)*, pp. 214-218, Sept 2014.
6. A. Costanzo, M. Fantuzzi, D. Masotti, and V. Rizzoli, "A Microwave Displacement Sensor System Exploiting Electromagnetic Interferometry," in *XX Riunione Nazionale di Elettromagnetismo (RiNEm)*, pp. 345-348, Sept 2014.
7. D. Masotti, A. Costanzo, M. Fantuzzi, F. Mastri, M. Aldrigo, and M. Dragoman, "Graphene-based nano-rectenna in the far infrared frequency band," in *2014 44th European Microwave Conference (EuMC)*, pp. 1202-1205, Oct 2014.
8. M. Fantuzzi, D. Masotti, and A. Costanzo, "Simultaneous UHF energy harvesting and UWB-RFID communication," in *2015 IEEE MTT-S International Microwave Symposium (IMS)*, pp. 1-4, May 2015.
9. A. Costanzo, M. Fantuzzi, D. Masotti, F. Mastri, and V. Rizzoli, "A rigorous circuit-level description of IR-UWB links," in *2015 International Conference on Electromagnetics in Advanced Applications (ICEAA)*, pp. 553-556, Sept 2015.
10. M. Fantuzzi, D. Masotti, and A. Costanzo, "A multilayer compact-size UWB-UHF antenna system for novel RFID applications," in *2015 European Microwave Conference (EuMC)*, pp. 255-258, Sept 2015.
11. M. Fantuzzi, D. Masotti, and A. Costanzo, "Electromagnetic pre-

- diction of antenna layout impact on UWB localization and sensing,” in *2015 International EURASIP Workshop on RFID Technology (EURFID)*, pp. 16-21, Oct 2015.
12. N. Decarli, A. Guerra, F. Guidi, M. Chiani, D. Dardari, A. Costanzo, M. Fantuzzi, D. Masotti, S. Bartoletti, J. S. Dehkordi, A. Conti, A. Romani, M. Tartagni, R. Alesii, P. D. Marco, F. Santucci, L. Roselli, M. Virili, P. Savazzi, and M. Bozzi, “The GRETA architecture for energy efficient radio identification and localization,” in *2015 International EURASIP Workshop on RFID Technology (EURFID)*, pp. 1-8, Oct 2015.
 13. M. Fantuzzi, M. Rajabi, G. Avolio, A. Costanzo, and D. Schreurs, “Large signal rectifier characterization for simultaneous data and Power Transfer,” in *2016 IEEE Wireless Power Transfer Conference (WPTC)*, pp. 1-4, May 2016.
 14. D. Masotti, M. Fantuzzi, and A. Costanzo, “Next generation zero-power RFID-tag for UWB pervasive identification,” in *2016 IEEE International Smart Cities Conference (ISC2)*, pp. 1-4, Sept 2016.
 15. M. Fantuzzi, D. Masotti, and A. Costanzo, “UWB-UHF RFID Tag on Paper for Simultaneous Communication and RF Energy Harvesting,” in *XXI Riunione Nazionale di Elettromagnetismo (RiNEM)*, pp. 1-4, Sept 2016.
 16. M. Fantuzzi, M. D. Prete, D. Masotti, and A. Costanzo, “Quasi-isotropic RF energy harvester for autonomous long distance IoT operations,” in *2017 IEEE MTT-S International Microwave Symposium (IMS)*, pp. 1345-1348, June 2017.
 17. A. Costanzo, D. Masotti, M. Fantuzzi, F. Berra, and M. D. Prete,

“Solutions for simultaneous wireless information and power transfer,” in *2017 International Conference on Electromagnetics in Advanced Applications (ICEAA)*, pp. 1898-1901, Sept 2017.

18. M. Fantuzzi, A. Costanzo, S. Tedjini, and P. Lemaitre-Auger, “Low-Cost UHF Near-Field Power Transmission for RFID Applications,” in *2017 European Microwave Conference (EuMC)*, pp. 212-215, Oct 2017.

Invited Talks

- A. Costanzo, D. Masotti, and M. Fantuzzi, “RF-baseband nonlinear co-design of zero-power harvesting systems”, Workshop “Non-linear RFID systems, characterization and exploitation”, in *IEEE MTT-S International Microwave Symposium (IMS)*, 17-22 May 2015.
- A. Costanzo, D. Masotti, and M. Fantuzzi, “Combining UWB- and UHF-RFID for Localization and Sensing”, Workshop “European Initiatives to Develop Wireless Power Supply for Sensor Node Evolution”, in *IEEE Radio and Wireless Week (RWW)*, 24-27 Jan. 2016.

Awards and Recognitions

- Winner (team) of ESoA-COST IC1301 Student Design Competition “Wireless Networks: from Energy Harvesting to Information Processing” – Barcelona (Spain), Nov. 2015.
- Winner of IEEE MTT-S 2016 Graduate Fellowship Award, May 2016.

List of Achievements

- Winner (team) of 2016 International Microwave Symposium (IMS) Student Design Competition “Wireless Energy Harvesting” – San Francisco (USA), May 2016.
- Winner of COST IC1301 Student Paper Competition – Aalborg (Denmark), Sep. 2016.
- Third place at University of Bologna 3MT[®] (Three Minutes Thesis) Competition – Bologna (Italy), Mar. 2017.
- Finalist at 2017 International Microwave Symposium (IMS) 3MT[®] (Three Minutes Thesis) Competition – Hawai’i (USA), Jun. 2017.
- Winner of SIEm-GTTI Student Paper Competition – Udine (Italy), Jun. 2017.

Bibliography

- [1] W. C. Brown, "The History of Power Transmission by Radio Waves," *IEEE Trans. Microw. Theory Techn.*, vol. 32, pp. 1230–1242, Sep 1984.
- [2] B. Strassner and K. Chang, "Microwave Power Transmission: Historical Milestones and System Components," *Proc. IEEE*, vol. 101, pp. 1379–1396, June 2013.
- [3] N. Tesla, "The true wireless," *Electrical Experimenter*, May 1919.
- [4] N. Tesla, "Apparatus for transmitting electrical energy," Dec 1914. US Patent 4 119 732.
- [5] G. Falciasecca and B. Valotti, "Guglielmo Marconi: The pioneer of wireless communications," in *2009 European Microwave Conference (EuMC)*, pp. 544–546, Sept 2009.
- [6] H. Matsumoto, "Research on solar power satellites and microwave power transmission in Japan," *IEEE Microw. Mag.*, vol. 3, pp. 36–45, Dec 2002.
- [7] J. O. McSpadden and J. C. Mankins, "Space solar power programs and microwave wireless power transmission technology," *IEEE Microw. Mag.*, vol. 3, pp. 46–57, Dec 2002.

- [8] P. Jaffe and J. McSpadden, “Energy Conversion and Transmission Modules for Space Solar Power,” *Proc. IEEE*, vol. 101, pp. 1424–1437, June 2013.
- [9] S. Sasaki, K. Tanaka, and K. i. Maki, “Microwave Power Transmission Technologies for Solar Power Satellites,” *Proc. IEEE*, vol. 101, pp. 1438–1447, June 2013.
- [10] W. C. Brown and E. E. Eves, “Beamed microwave power transmission and its application to space,” *IEEE Trans. Microw. Theory Techn.*, vol. 40, pp. 1239–1250, Jun 1992.
- [11] N. B. Carvalho, A. Georgiadis, A. Costanzo, H. Rogier, A. Collado, J. A. García, S. Lucyszyn, P. Mezzanotte, J. Kracek, D. Masotti, A. J. S. Boaventura, M. de las Nieves Ruíz Lavín, M. Piñuela, D. C. Yates, P. D. Mitcheson, M. Mazanek, and V. Pankrac, “Wireless Power Transmission: R and D Activities Within Europe,” *IEEE Trans. Microw. Theory Techn.*, vol. 62, pp. 1031–1045, April 2014.
- [12] Wireless Power Consortium. Online: <http://www.wirelesspower-consortium.com/>.
- [13] AirFuel (merger of Alliance for Wireless Power and Power Matter Alliance). Online: <http://www.airfuel.org/>.
- [14] A. W. Green and J. T. Boys, “10 kHz inductively coupled power transfer-concept and control,” in *1994 Fifth International Conference on Power Electronics and Variable-Speed Drives*, pp. 694–699, Oct 1994.
- [15] S. Y. R. Hui and W. W. C. Ho, “A new generation of universal contactless Battery Charging platform for portable Consumer Elec-

- tronic equipment,” *IEEE Trans. Power Electron.*, vol. 20, pp. 620–627, May 2005.
- [16] C.-S. Wang, O. H. Stielau, and G. A. Covic, “Design considerations for a contactless electric vehicle battery charger,” *IEEE Trans. Ind. Electron.*, vol. 52, pp. 1308–1314, Oct 2005.
- [17] G. A. Covic and J. T. Boys, “Inductive Power Transfer,” *Proc. IEEE*, vol. 101, pp. 1276–1289, June 2013.
- [18] I. Mayordomo, T. Dräger, P. Spies, J. Bernhard, and A. Pflaum, “An Overview of Technical Challenges and Advances of Inductive Wireless Power Transmission,” *Proc. IEEE*, vol. 101, pp. 1302–1311, June 2013.
- [19] A. P. Sample, B. H. Waters, S. T. Wisdom, and J. R. Smith, “Enabling Seamless Wireless Power Delivery in Dynamic Environments,” *Proc. IEEE*, vol. 101, pp. 1343–1358, June 2013.
- [20] J. Garnica, R. A. Chinga, and J. Lin, “Wireless Power Transmission: From Far Field to Near Field,” *Proc. IEEE*, vol. 101, pp. 1321–1331, June 2013.
- [21] Powermat. Online: <https://www.powermat.com/>.
- [22] Wipower. Online: <https://www.qualcomm.com/products/wipower>.
- [23] WiTricity. Online: <http://witricity.com/>.
- [24] U. K. Madawala and D. J. Thrimawithana, “A Bidirectional Inductive Power Interface for Electric Vehicles in V2G Systems,” *IEEE Trans. Ind. Electron.*, vol. 58, pp. 4789–4796, Oct 2011.

- [25] G. A. Covic and J. T. Boys, “Modern Trends in Inductive Power Transfer for Transportation Applications,” *IEEE Trans. Emerg. Sel. Topics Power Electron.*, vol. 1, pp. 28–41, March 2013.
- [26] J. Shin, S. Shin, Y. Kim, S. Ahn, S. Lee, G. Jung, S. J. Jeon, and D. H. Cho, “Design and Implementation of Shaped Magnetic-Resonance-Based Wireless Power Transfer System for Roadway-Powered Moving Electric Vehicles,” *IEEE Trans. Ind. Electron.*, vol. 61, pp. 1179–1192, March 2014.
- [27] S. Kim, J. S. Ho, and A. S. Y. Poon, “Wireless Power Transfer to Miniature Implants: Transmitter Optimization,” *IEEE Trans. Antennas Propag.*, vol. 60, pp. 4838–4845, Oct 2012.
- [28] J. S. Ho, S. Kim, and A. S. Y. Poon, “Midfield Wireless Powering for Implantable Systems,” *Proc. IEEE*, vol. 101, pp. 1369–1378, June 2013.
- [29] A. Kurs, A. Karalis, R. Moffatt, J. D. Joannopoulos, P. Fisher, and M. Soljačić, “Wireless Power Transfer via Strongly Coupled Magnetic Resonances,” *Science*, vol. 317, no. 5834, pp. 83–86, 2007.
- [30] W. C. Brown, “An experimental low power density rectenna,” in *1991 IEEE MTT-S International Microwave Symposium Digest*, pp. 197–200 vol.1, July 1991.
- [31] N. Shinohara and H. Matsumoto, “Experimental study of large rectenna array for microwave energy transmission,” *IEEE Trans. Microw. Theory Techn.*, vol. 46, pp. 261–268, Mar 1998.
- [32] L. W. Epp, A. R. Khan, H. K. Smith, and R. P. Smith, “A compact dual-polarized 8.51-GHz rectenna for high-voltage (50 V) actua-

- tor applications,” *IEEE Trans. Microw. Theory Techn.*, vol. 48, pp. 111–120, Jan 2000.
- [33] N. Shinohara, “Beam Control Technologies With a High-Efficiency Phased Array for Microwave Power Transmission in Japan,” *Proc. IEEE*, vol. 101, pp. 1448–1463, June 2013.
- [34] A. Massa, G. Oliveri, F. Viani, and P. Rocca, “Array Designs for Long-Distance Wireless Power Transmission: State-of-the-Art and Innovative Solutions,” *Proc. IEEE*, vol. 101, pp. 1464–1481, June 2013.
- [35] J. A. Hagerty, F. B. Helmbrecht, W. H. McCalpin, R. Zane, and Z. B. Popovic, “Recycling ambient microwave energy with broadband rectenna arrays,” *IEEE Trans. Microw. Theory Techn.*, vol. 52, pp. 1014–1024, March 2004.
- [36] E. Falkenstein, M. Roberg, and Z. Popovic, “Low-Power Wireless Power Delivery,” *IEEE Trans. Microw. Theory Techn.*, vol. 60, pp. 2277–2286, July 2012.
- [37] H. J. Visser and R. J. M. Vullers, “RF Energy Harvesting and Transport for Wireless Sensor Network Applications: Principles and Requirements,” *Proc. IEEE*, vol. 101, pp. 1410–1423, June 2013.
- [38] M. Piñuela, P. D. Mitcheson, and S. Lucyszyn, “Ambient RF Energy Harvesting in Urban and Semi-Urban Environments,” *IEEE Trans. Microw. Theory Techn.*, vol. 61, pp. 2715–2726, July 2013.
- [39] S. Kim, R. Vyas, J. Bito, K. Niotaki, A. Collado, A. Georgiadis, and M. M. Tentzeris, “Ambient RF Energy-Harvesting Technolo-

- gies for Self-Sustainable Standalone Wireless Sensor Platforms,” *Proc. IEEE*, vol. 102, pp. 1649–1666, Nov 2014.
- [40] IHS Technology - IoT platforms: enabling the Internet of Things. March 2016. Online: <https://cdn.ihs.com/www/pdf/enabling-IOT.pdf>.
- [41] Open Geospatial Consortium, "OGC Abstract Specification". Online: <http://www.opengeospatial.org/docs/as>.
- [42] M. Botts, G. Percivall, C. Reed, and J. Davidson, *OGC Sensor Web Enablement: Overview and High Level Architecture*, pp. 175–190. Berlin, Heidelberg: Springer Berlin Heidelberg, 2008.
- [43] Kevin Ashton, "That 'Internet of Things' Thing", *RFID Journal*. Online: <http://www.rfidjournal.com/articles/view?4986>.
- [44] M. Belleville, H. Fanet, P. Fiorini, P. Nicole, M. Pelgrom, C. Piguet, R. Hahn, C. V. Hoof, R. Vullers, M. Tartagni, and E. Cantatore, "Energy autonomous sensor systems: Towards a ubiquitous sensor technology," *Microelectronics Journal*, vol. 41, no. 11, pp. 740–745, 2010. IEEE International Workshop on Advances in Sensors and Interfaces 2009.
- [45] Z. Popovic, E. A. Falkenstein, D. Costinett, and R. Zane, "Low-Power Far-Field Wireless Powering for Wireless Sensors," *Proc. IEEE*, vol. 101, pp. 1397–1409, June 2013.
- [46] EPCTM Radio-Frequency Identity Protocols Generation-2 UHF RFID, v 2.0.1, 2015.
- [47] K. Finkenzeller, *RFID Handbook: Fundamentals and Applications in Contactless Smart Cards and Identification*. Wiley, 2 ed., 2003.

- [48] D. Dardari, M. Luise, and E. Falletti, *Satellite and terrestrial radio positioning techniques: a signal processing perspective*. Elsevier, 1 ed., 2011.
- [49] R. Verdone, D. Dardari, G. Mazzini, and A. Conti, *Wireless Sensor and Actuator Networks - Technologies, Analysis and Design*. Elsevier, 1 ed., 2008.
- [50] Italian National project PRIN-GRETA ("GREEn TAGs and sensors with ultra-wideband identification and localization capabilities"), 2012-2015. Online: <http://www.greentags.eu/>.
- [51] M. Chiani and A. Giorgetti, "Coexistence Between UWB and Narrow-Band Wireless Communication Systems," *Proc. IEEE*, vol. 97, pp. 231–254, Feb 2009.
- [52] D. Dardari, R. D'Errico, C. Roblin, A. Sibille, and M. Z. Win, "Ultrawide Bandwidth RFID: The Next Generation?," *Proc. IEEE*, vol. 98, pp. 1570–1582, Sept 2010.
- [53] C. Xu and C. L. Law, "TOA Estimator for UWB Backscattering RFID System with Clutter Suppression Capability," *EURASIP J. Wireless Comm. Net.*, vol. 2010, p. 753129, Jun 2010.
- [54] N. Decarli, F. Guidi, and D. Dardari, "A Novel Joint RFID and Radar Sensor Network for Passive Localization: Design and Performance Bounds," *IEEE J. Sel. Topics Signal Process.*, vol. 8, pp. 80–95, Feb 2014.
- [55] A. Ramos, D. Girbau, A. Lázaro, A. Collado, and A. Georgiadis, "Solar-Powered Wireless Temperature Sensor Based on UWB RFID With Self-Calibration," *IEEE Sensors J.*, vol. 15, pp. 3764–3772, July 2015.

- [56] V. Lakafosis, A. Rida, R. Vyas, L. Yang, S. Nikolaou, and M. M. Tentzeris, "Progress Towards the First Wireless Sensor Networks Consisting of Inkjet-Printed, Paper-Based RFID-Enabled Sensor Tags," *Proc. IEEE*, vol. 98, pp. 1601–1609, Sept 2010.
- [57] ETSI EN 302 065, "Electromagnetic compatibility and Radio spectrum Matters (ERM); Short Range Devices (SRD) using Ultra Wide Band technology (UWB) for communications purposes", v 1.2.1, 2010.
- [58] D. Masotti, A. Costanzo, P. Francia, M. Filippi, and A. Romani, "A Load-Modulated Rectifier for RF Micropower Harvesting With Start-Up Strategies," *IEEE Trans. Microw. Theory Techn.*, vol. 62, pp. 994–1004, April 2014.
- [59] R. D'Errico, M. Bottazzi, F. Natali, E. Savioli, S. Bartoletti, A. Conti, D. Dardari, N. Decarli, F. Guidi, F. Dehmas, L. Ouvre, U. Alvarado, N. Hadaschik, C. Franke, Z. Mhanna, M. Sacko, Y. Wei, and A. Sibille, "An UWB-UHF semi-passive RFID System for localization and tracking applications," in *2012 IEEE International Conference on RFID-Technologies and Applications (RFID-TA)*, pp. 18–23, Nov 2012.
- [60] C. C. Cruz, J. R. Costa, and C. A. Fernandes, "Hybrid UHF/UWB Antenna for Passive Indoor Identification and Localization Systems," *IEEE Trans. Antennas Propag.*, vol. 61, pp. 354–361, Jan 2013.
- [61] A. Ramos, A. Lazaro, and D. Girbau, "Semi-Passive Time-Domain UWB RFID System," *IEEE Trans. Microw. Theory Techn.*, vol. 61, pp. 1700–1708, April 2013.

- [62] M. Pigeon, R. D’Errico, and C. Delaveaud, “UHF-UWB tag antenna for passive RFID applications,” in *2013 7th European Conference on Antennas and Propagation (EuCAP)*, pp. 3968–3972, April 2013.
- [63] V. Rizzoli, A. Costanzo, and P. Spadoni, “Computer-Aided Design of Ultra-Wideband Active Antennas by Means of a New Figure of Merit,” *IEEE Microw. Compon. Lett.*, vol. 18, pp. 290–292, April 2008.
- [64] Y. Lu, Y. Huang, Y. C. Shen, and H. T. Chattha, “A further study of planar UWB monopole antennas,” in *2009 Loughborough Antennas Propagation Conference*, pp. 353–356, Nov 2009.
- [65] W. Wiesbeck, G. Adamiuk, and C. Sturm, “Basic Properties and Design Principles of UWB Antennas,” *Proc. IEEE*, vol. 97, pp. 372–385, Feb 2009.
- [66] E. Gazit, “Improved design of the Vivaldi antenna,” *IEE Proc-H*, vol. 135, pp. 89–92, April 1988.
- [67] W. L. Stutzman and G. A. Thiele, *Antenna Theory and Design*. Wiley, 3 ed., 2013.
- [68] O. A. Mashaal, S. K. A. Rahim, A. Y. Abdulrahman, M. I. Sabran, M. S. A. Rani, and P. S. Hall, “A Coplanar Waveguide Fed Two Arm Archimedean Spiral Slot Antenna With Improved Bandwidth,” *IEEE Trans. Antennas Propag.*, vol. 61, pp. 939–943, Feb 2013.
- [69] A. R. Guraliuc, R. Caso, P. Nepa, and J. L. Volakis, “Numerical Analysis of a Wideband Thick Archimedean Spiral Antenna,” *IEEE Antennas Wireless Propag. Lett.*, vol. 11, pp. 168–171, 2012.

- [70] M. Lee, B. A. Kramer, C.-C. Chen, and J. L. Volakis, "Broadband Spiral Antenna Miniaturization Limit," in *2006 IEEE Antennas and Propagation Society International Symposium*, pp. 3701–3704, July 2006.
- [71] B. A. Kramer, C. C. Chen, M. Lee, and J. L. Volakis, "Fundamental Limits and Design Guidelines for Miniaturizing Ultra-Wideband Antennas," *IEEE Antennas Propag. Mag.*, vol. 51, pp. 57–69, Aug 2009.
- [72] B. A. Kramer, M. Lee, C.-C. Chen, and J. L. Volakis, "Design and performance of an ultrawide-band ceramic-loaded slot spiral," *IEEE Trans. Antennas Propag.*, vol. 53, pp. 2193–2199, July 2005.
- [73] M. Aldrigo, A. Costanzo, D. Masotti, C. Baldisserrri, I. Dumitru, and C. Galassi, "Numerical and experimental characterization of a button-shaped miniaturized UHF antenna on magneto-dielectric substrate," *Int. J. Microw. Wireless Tech.*, vol. 5, no. 3, pp. 231–239, 2013.
- [74] C. Ding, C. Ruan, L. Peng, and J. Chu, "A novel archimedean spiral antenna with uniplanar EBG substrate," in *2008 8th International Symposium on Antennas, Propagation and EM Theory*, pp. 313–315, Nov 2008.
- [75] ETSI EN 302 208-1, "Radio Frequency Identification Equipment operating in the band 865 MHz to 868 MHz with power levels up to 2 W", v 2.1.0, 2014.
- [76] Computer Simulation Technologies (CST) Studio Suite. Online: <http://www.cst.com>.

- [77] K. D. Palmer and M. W. van Rooyen, "Simple broadband measurements of balanced loads using a network analyzer," *IEEE Trans. Instrum. Meas.*, vol. 55, pp. 266–272, Feb 2006.
- [78] K. Hirose, M. Miyamoto, and H. Nakano, "A two-wire spiral antenna with unbalanced feed," in *IEEE Antennas and Propagation Society International Symposium. 2001 Digest. Held in conjunction with: USNC/URSI National Radio Science Meeting (Cat. No.01CH37229)*, vol. 4, pp. 128–131 vol.4, July 2001.
- [79] R. K. Tallos, Z. Wang, and J. L. Volakis, "Wi-Fi energy harvesting system using body-worn antennas," in *2014 IEEE Antennas and Propagation Society International Symposium (APSURSI)*, pp. 1405–1406, July 2014.
- [80] Skyworks Solutions Inc., *Surface Mount Mixer and Detector Schottky Diodes - SMS7630-079LF*, 2016.
- [81] D. Masotti, A. Costanzo, F. Mastri, M. Aldrigo, and V. Rizzoli, "Nonlinear/electromagnetic co-design of MIMO and UWB radio links," in *Computational Electromagnetics International Workshop (CEM), 2011*, pp. 47–52, Aug 2011.
- [82] E. A. Navarro, J. M. Blanes, J. A. Carrasco, and C. Reig, "Yagi-Like Printed Antennas for Wireless Sensor Networks," in *2007 International Conference on Sensor Technologies and Applications (SENSORCOMM 2007)*, pp. 254–259, Oct 2007.
- [83] M. D. Prete, D. Masotti, N. Arbizzani, and A. Costanzo, "Remotely Identify and Detect by a Compact Reader With Mono-Pulse Scanning Capabilities," *IEEE Trans. Microw. Theory Techn.*, vol. 61, pp. 641–650, Jan 2013.

- [84] L. Yang, A. Rida, R. Vyas, and M. M. Tentzeris, "RFID Tag and RF Structures on a Paper Substrate Using Inkjet-Printing Technology," *IEEE Trans. Microw. Theory Techn.*, vol. 55, pp. 2894–2901, Dec 2007.
- [85] S. Kim, A. Georgiadis, A. Collado, and M. M. Tentzeris, "An Inkjet-Printed Solar-Powered Wireless Beacon on Paper for Identification and Wireless Power Transmission Applications," *IEEE Trans. Microw. Theory Techn.*, vol. 60, pp. 4178–4186, Dec 2012.
- [86] B. S. Cook and A. Shamim, "Inkjet Printing of Novel Wideband and High Gain Antennas on Low-Cost Paper Substrate," *IEEE Trans. Antennas Propag.*, vol. 60, pp. 4148–4156, Sept 2012.
- [87] S. Kim, C. Mariotti, F. Alimenti, P. Mezzanotte, A. Georgiadis, A. Collado, L. Roselli, and M. M. Tentzeris, "No Battery Required: Perpetual RFID-Enabled Wireless Sensors for Cognitive Intelligence Applications," *IEEE Microw. Mag.*, vol. 14, pp. 66–77, July 2013.
- [88] Y. Kawahara, S. Hodges, N. W. Gong, S. Olberding, and J. Steimle, "Building Functional Prototypes Using Conductive Inkjet Printing," *IEEE Pervasive Comput.*, vol. 13, pp. 30–38, July 2014.
- [89] C. Mariotti, F. Alimenti, P. Mezzanotte, M. Dionigi, M. Virili, S. Giacomucci, and L. Roselli, "Modeling and characterization of copper tape microstrips on paper substrate and application to 24 GHz branch-line couplers," in *2013 European Microwave Conference*, pp. 794–797, Oct 2013.

- [90] A. Costanzo, M. Dionigi, D. Masotti, M. Mongiardo, G. Monti, L. Tarricone, and R. Sorrentino, "Electromagnetic Energy Harvesting and Wireless Power Transmission: A Unified Approach," *Proc. IEEE*, vol. 102, pp. 1692–1711, Nov 2014.
- [91] H. J. Visser, S. Keyrouz, and A. B. Smolders, "Optimized rectenna design," *Wireless Power Transfer*, vol. 2, no. 1, pp. 44–50, 2015.
- [92] N. Decarli, A. Guerra, F. Guidi, M. Chiani, D. Dardari, A. Costanzo, M. Fantuzzi, D. Masotti, S. Bartoletti, J. S. Dehkorrdi, A. Conti, A. Romani, M. Tartagni, R. Alesii, P. D. Marco, F. Santucci, L. Roselli, M. Virili, P. Savazzi, and M. Bozzi, "The GRETA architecture for energy efficient radio identification and localization," in *2015 International EURASIP Workshop on RFID Technology (EURFID)*, pp. 1–8, Oct 2015.
- [93] D. Dardari, A. Conti, U. Ferner, A. Giorgetti, and M. Z. Win, "Ranging With Ultrawide Bandwidth Signals in Multipath Environments," *Proc. IEEE*, vol. 97, pp. 404–426, Feb 2009.
- [94] V. Rizzoli, F. Matri, A. Costanzo, and D. Masotti, "Harmonic-Balance Algorithms for the Circuit-Level Nonlinear Analysis of UWB Receivers in the Presence of Interfering Signals," *IEEE Trans. Comput.-Aided Design Integr. Circuits Syst.*, vol. 28, pp. 516–527, April 2009.
- [95] A. Georgiadis, G. V. Andia, and A. Collado, "Rectenna design and optimization using reciprocity theory and harmonic balance analysis for electromagnetic (EM) energy harvesting," *IEEE Antennas Wireless Propag. Lett.*, vol. 9, pp. 444–446, 2010.

- [96] A. Costanzo, A. Romani, D. Masotti, N. Arbizzani, and V. Rizzoli, “RF/baseband co-design of switching receivers for multiband microwave energy harvesting,” *Sensors and Actuators A: Physical*, vol. 179, pp. 158–168, Mar 2012.
- [97] A. Costanzo, F. Mastri, D. Masotti, and V. Rizzoli, “Circuit-level nonlinear/EM co-simulation and co-design of UWB receivers,” in *2011 IEEE International Conference on Ultra-Wideband (ICUWB)*, pp. 425–429, Sept 2011.
- [98] F. Guidi, N. Decarli, S. Bartoletti, A. Conti, and D. Dardari, “Detection of Multiple Tags Based on Impulsive Backscattered Signals,” *IEEE Trans. Commun.*, vol. 62, pp. 3918–3930, Nov 2014.
- [99] E. Hossain, M. Rasti, H. Tabassum, and A. Abdelnasser, “Evolution toward 5G multi-tier cellular wireless networks: An interference management perspective,” *IEEE Wireless Commun.*, vol. 21, pp. 118–127, June 2014.
- [100] J. Huang, C. C. Xing, and C. Wang, “Simultaneous Wireless Information and Power Transfer: Technologies, Applications, and Research Challenges,” *IEEE Commun. Mag.*, vol. 55, pp. 26–32, Nov 2017.
- [101] X. Zhou, R. Zhang, and C. K. Ho, “Wireless Information and Power Transfer: Architecture Design and Rate-Energy Tradeoff,” *IEEE Trans. Commun.*, vol. 61, pp. 4754–4767, November 2013.
- [102] I. Krikidis, S. Timotheou, S. Nikolaou, G. Zheng, D. W. K. Ng, and R. Schober, “Simultaneous wireless information and power transfer in modern communication systems,” *IEEE Commun. Mag.*, vol. 52, pp. 104–110, Nov 2014.

- [103] Z. Ding, C. Zhong, D. W. K. Ng, M. Peng, H. A. Suraweera, R. Schober, and H. V. Poor, "Application of smart antenna technologies in simultaneous wireless information and power transfer," *IEEE Commun. Mag.*, vol. 53, pp. 86–93, April 2015.
- [104] T. W. Yoo and K. Chang, "Theoretical and experimental development of 10 and 35 GHz rectennas," *IEEE Trans. Microw. Theory Techn.*, vol. 40, pp. 1259–1266, Jun 1992.
- [105] J. O. McSpadden, L. Fan, and K. Chang, "Design and experiments of a high-conversion-efficiency 5.8-GHz rectenna," *IEEE Trans. Microw. Theory Techn.*, vol. 46, pp. 2053–2060, Dec 1998.
- [106] J. C. Pedro and N. B. Carvalho, *Intermodulation Distortion in Microwave and Wireless Circuits*. 685 Canton Street Norwood, 02062, MA, USA: Artech House, Inc., 2003.
- [107] J. H. Kim, J. Bito, and M. M. Tentzeris, "Design optimization of an energy harvesting RF-DC conversion circuit operating at 2.45GHz," in *2015 IEEE International Symposium on Antennas and Propagation USNC/URSI National Radio Science Meeting*, pp. 1280–1281, July 2015.
- [108] I. Ramos and Z. Popovic, "A compact 2.45 GHz, low power wireless energy harvester with a reflector-backed folded dipole rectenna," in *2015 IEEE Wireless Power Transfer Conference (WPTC)*, pp. 1–3, May 2015.
- [109] M. Fantuzzi, D. Masotti, and A. Costanzo, "A multilayer compact-size UWB-UHF antenna system for novel RFID applications," in *2015 European Microwave Conference (EuMC)*, pp. 255–258, Sept 2015.

- [110] C. H. P. Lorenz, S. Hemour, and K. Wu, “Physical Mechanism and Theoretical Foundation of Ambient RF Power Harvesting Using Zero-Bias Diodes,” *IEEE Trans. Microw. Theory Techn.*, vol. 64, pp. 2146–2158, July 2016.
- [111] G. Pailloncy, G. Avolio, M. Myslinski, Y. Rolain, M. V. Bossche, and D. Schreurs, “Large-Signal Network Analysis Including the Baseband,” *IEEE Microw. Mag.*, vol. 12, pp. 77–86, April 2011.
- [112] W. V. Moer and L. Gomme, “NVNA versus LSNA: enemies or friends?,” *IEEE Microw. Mag.*, vol. 11, pp. 97–103, Feb 2010.
- [113] E. H. Fooks and R. A. Zakarevičius, *Microwave Engineering Using Microstrip Circuits*. Upper Saddle River, NJ, USA: Prentice-Hall, Inc., 1990.
- [114] G. Crupi and D. M.-P. Schreurs, *Microwave De-embedding - From Theory to Applications*. Elsevier, 1 ed., 2013.
- [115] Keysight Advanced Design System (ADS). Online: <http://www.keysight.com/en/pc-1297113/advanced-design-system-ads?nid=-34346.0&cc=US&lc=eng>.
- [116] G. Massobrio and P. Antognetti, *Semiconductor Device Modeling with SPICE*. McGraw-Hill, 2 ed., 1993.
- [117] T. J. Lee, P. Patil, C. Y. Hu, M. Rajabi, S. Farsi, and D. M. M. P. Schreurs, “Design of efficient rectifier for low-power wireless energy harvesting at 2.45 GHz,” in *2015 IEEE Radio and Wireless Symposium (RWS)*, pp. 47–49, Jan 2015.
- [118] X. Lu, P. Wang, D. Niyato, D. I. Kim, and Z. Han, “Wireless Networks With RF Energy Harvesting: A Contemporary Survey,”

- IEEE Communications Surveys Tutorials*, vol. 17, pp. 757–789, Secondquarter 2015.
- [119] M. S. Trotter, J. D. Griffin, and G. D. Durgin, “Power-optimized waveforms for improving the range and reliability of RFID systems,” in *2009 IEEE International Conference on RFID*, pp. 80–87, April 2009.
- [120] A. J. S. Boaventura and N. Carvalho, “Extending Reading Range of Commercial RFID Readers,” *IEEE Trans. Microw. Theory Techn.*, vol. 61, pp. 633–640, Jan 2013.
- [121] M. D. Prete, A. Costanzo, M. Magno, D. Masotti, and L. Benini, “Optimum Excitations for a Dual-Band Microwatt Wake-Up Radio,” *IEEE Trans. Microw. Theory Techn.*, vol. 64, pp. 4731–4739, Dec 2016.
- [122] A. S. Boaventura and N. B. Carvalho, “Maximizing DC power in energy harvesting circuits using multisine excitation,” in *2011 IEEE MTT-S International Microwave Symposium*, pp. 1–4, June 2011.
- [123] C. L. Yang, C. L. Tsai, Y. L. Yang, and C. S. Lee, “Enhancement of Wireless Power Transmission by Using Novel Multitone Approaches for Wireless Recharging,” *IEEE Antennas Wireless Propag. Lett.*, vol. 10, pp. 1353–1357, 2011.
- [124] A. Collado and A. Georgiadis, “Improving wireless power transmission efficiency using chaotic waveforms,” in *2012 IEEE/MTT-S International Microwave Symposium Digest*, pp. 1–3, June 2012.
- [125] A. Boaventura, D. Belo, R. Fernandes, A. Collado, A. Georgiadis, and N. B. Carvalho, “Boosting the Efficiency: Unconventional

- Waveform Design for Efficient Wireless Power Transfer,” *IEEE Microw. Mag.*, vol. 16, pp. 87–96, April 2015.
- [126] C. R. Valenta, M. M. Morys, and G. D. Durgin, “Theoretical Energy-Conversion Efficiency for Energy-Harvesting Circuits Under Power-Optimized Waveform Excitation,” *IEEE Trans. Microw. Theory Techn.*, vol. 63, pp. 1758–1767, May 2015.
- [127] F. Bolos, J. Blanco, A. Collado, and A. Georgiadis, “RF Energy Harvesting From Multi-Tone and Digitally Modulated Signals,” *IEEE Trans. Microw. Theory Techn.*, vol. 64, pp. 1918–1927, June 2016.
- [128] H. Sakaki, K. Nishikawa, S. Yoshida, and S. Kawasaki, “Modulated scheme and input power impact on rectifier RF-DC efficiency for WiCoPT system,” in *2015 European Microwave Conference (EuMC)*, pp. 60–63, Sept 2015.
- [129] H. Shimamura, R. Tanaka, H. Sakaki, S. Yoshida, K. Nishikawa, and S. Kawasaki, “Impact of symbol rate and roll-off factor on rectifier RF-DC conversion efficiency for WiCoPT system,” in *2016 46th European Microwave Conference (EuMC)*, pp. 934–937, Oct 2016.
- [130] M. Rajabi, S. Pollin, and D. Schreurs, “Hybrid rectifier-receiver node,” in *2017 IEEE MTT-S International Microwave Symposium (IMS)*, pp. 1038–1041, June 2017.
- [131] N. Pan, D. Belo, M. Rajabi, D. Schreurs, N. B. Carvalho, and S. Pollin, “Bandwidth Analysis of RF-DC Converters Under Multisine Excitation,” *IEEE Trans. Microw. Theory Techn.*, vol. 66, pp. 791–802, Feb 2018.

- [132] S. Claessens, M. Rajabi, N. Pan, S. Pollin, and D. Schreurs, “Measurement-based analysis of the throughput-power level trade-off with modulated multisine signals in a SWIPT system,” in *2017 89th ARFTG Microwave Measurement Conference (ARFTG)*, pp. 1–4, June 2017.
- [133] D. Zhang, L. T. Yang, M. Chen, S. Zhao, M. Guo, and Y. Zhang, “Real-Time Locating Systems Using Active RFID for Internet of Things,” *IEEE Syst. J.*, vol. 10, pp. 1226–1235, Sept 2016.
- [134] R. Miesen, R. Ebelt, F. Kirsch, T. Schäfer, G. Li, H. Wang, and M. Vossiek, “Where is the Tag?,” *IEEE Microw. Mag.*, vol. 12, pp. S49–S63, Dec 2011.
- [135] R. Miesen, F. Kirsch, and M. Vossiek, “Holographic localization of passive UHF RFID transponders,” in *2011 IEEE International Conference on RFID*, pp. 32–37, April 2011.
- [136] Y. Ma, L. Zhou, K. Liu, and J. Wang, “Iterative Phase Reconstruction and Weighted Localization Algorithm for Indoor RFID-Based Localization in NLOS Environment,” *IEEE Sensors J.*, vol. 14, pp. 597–611, Feb 2014.
- [137] L. Qiu, Z. Huang, N. Wirström, and T. Voigt, “3DinSAR: Object 3D localization for indoor RFID applications,” in *2016 IEEE International Conference on RFID (RFID)*, pp. 1–8, May 2016.
- [138] A. Costanzo, D. Masotti, T. Ussmueller, and R. Weigel, “Tag, You’re It: Ranging and Finding via RFID Technology,” *IEEE Microw. Mag.*, vol. 14, pp. 36–46, July 2013.
- [139] IEEE Std 802.15.4a-2007, pp. 1-203, Aug 2007.
- [140] IEEE Std 802.15.4f-2012, pp. 1-72, Apr 2012.

- [141] A. Romani, M. Filippi, M. Dini, and M. Tartagni, "A Sub- μ A Stand-By Current Synchronous Electric Charge Extractor for Piezoelectric Energy Harvesting," *AMC J. Emerg. Technol. Comput. Syst.*, vol. 12, Jul 2015.
- [142] Texas Instruments Inc., *BQ25570 Nano Power Boost Charger and Buck Converter for Energy Harvester Powered Applications*, 2015.
- [143] H. W. Pflug, H. J. Visser, and S. Keyrouz, "Practical applications of radiative wireless power transfer," in *2015 IEEE Wireless Power Transfer Conference (WPTC)*, pp. 1–4, May 2015.
- [144] E. Popovici, M. Magno, and S. Marinkovic, "Power management techniques for Wireless Sensor Networks: A review," in *5th IEEE International Workshop on Advances in Sensors and Interfaces IWASI*, pp. 194–198, June 2013.
- [145] M. Magno and L. Benini, "An ultra low power high sensitivity wake-up radio receiver with addressing capability," in *2014 IEEE 10th International Conference on Wireless and Mobile Computing, Networking and Communications (WiMob)*, pp. 92–99, Oct 2014.
- [146] M. D. Prete, D. Masotti, A. Costanzo, M. Magno, and L. Benini, "A dual-band wake-up radio for ultra-low power Wireless Sensor Networks," in *2016 IEEE Topical Conference on Wireless Sensors and Sensor Networks (WiSNet)*, pp. 81–84, Jan 2016.
- [147] M. Magno, N. Jackson, A. Mathewson, L. Benini, and E. Popovici, "Combination of hybrid energy harvesters with MEMS piezoelectric and nano-Watt radio wake up to extend lifetime of system for wireless sensor nodes," in *26th International Conference on Architecture of Computing Systems 2013*, pp. 1–6, Feb 2013.

- [148] R. Piyare, A. L. Murphy, C. Kiraly, P. Tosato, and D. Brunelli, “Ultra Low Power Wake-Up Radios: A Hardware and Networking Survey,” *IEEE Communications Surveys Tutorials*, vol. 19, pp. 2117–2157, Fourthquarter 2017.
- [149] N. Shinohara and H. Matsumoto, “Dependence of dc output of a rectenna array on the method of interconnection of its array elements,” *Electrical Engineering in Japan*, vol. 125, no. 1, pp. 9–17, 1998.
- [150] B. Strassner and K. Chang, “5.8-GHz circularly polarized rectifying antenna for wireless microwave power transmission,” *IEEE Trans. Microw. Theory Techn.*, vol. 50, pp. 1870–1876, Aug 2002.
- [151] Y.-J. Ren and K. Chang, “New 5.8-GHz circularly polarized retrodirective rectenna arrays for wireless power transmission,” *IEEE Trans. Microw. Theory Techn.*, vol. 54, pp. 2970–2976, July 2006.
- [152] U. Olgun, C. C. Chen, and J. L. Volakis, “Investigation of Rectenna Array Configurations for Enhanced RF Power Harvesting,” *IEEE Antennas Wireless Propag. Lett.*, vol. 10, pp. 262–265, 2011.
- [153] R. Yuwono, M. A. Hamdany, F. K. Dwi, N. Auliya, and Aisah, “Serial rectifier antenna to increase its output power,” in *2016 International Seminar on Intelligent Technology and Its Applications (ISITIA)*, pp. 451–456, July 2016.
- [154] D. J. Lee, S. J. Lee, I. J. Hwang, W. S. Lee, and J. W. Yu, “Hybrid Power Combining Rectenna Array for Wide Incident Angle

- Coverage in RF Energy Transfer,” *IEEE Trans. Microw. Theory Techn.*, vol. 65, pp. 3409–3418, Sept 2017.
- [155] H. Sun and W. Geyi, “A New Rectenna With All-Polarization-Receiving Capability for Wireless Power Transmission,” *IEEE Antennas Wireless Propag. Lett.*, vol. 15, pp. 814–817, 2016.
- [156] A. Costanzo, F. Donzelli, D. Masotti, and V. Rizzoli, “Rigorous design of RF multi-resonator power harvesters,” in *Proceedings of the Fourth European Conference on Antennas and Propagation*, pp. 1–4, April 2010.
- [157] V. Rizzoli, A. Costanzo, and G. Monti, “General electromagnetic compatibility analysis for nonlinear microwave integrated circuits,” in *2004 IEEE MTT-S International Microwave Symposium Digest (IEEE Cat. No.04CH37535)*, vol. 2, pp. 953–956 Vol.2, June 2004.
- [158] H. Kamoda, M. Hanazawa, S. Kitazawa, H. Ban, and K. Kobayashi, “Mutual coupling effect on rectenna array for RF energy harvesting,” in *2013 European Microwave Conference*, pp. 503–506, Oct 2013.
- [159] A. Stjernman, “Relationship between radiation pattern correlation and scattering matrix of lossless and lossy antennas,” *Electronics Letters*, vol. 41, pp. 678–680, June 2005.
- [160] C. Craeye and D. González-Ovejero, “A review on array mutual coupling analysis,” *Radio Science*, vol. 46, no. 2, 2011.
- [161] M. S. Sharawi, “Printed Multi-Band MIMO Antenna Systems and Their Performance Metrics,” *IEEE Antennas Propag. Mag.*, vol. 55, pp. 218–232, Oct 2013.

- [162] S. C. Chen, Y. S. Wang, and S. J. Chung, "A Decoupling Technique for Increasing the Port Isolation Between Two Strongly Coupled Antennas," *IEEE Trans. Antennas Propag.*, vol. 56, pp. 3650–3658, Dec 2008.
- [163] L. Xie, Y. Shi, Y. T. Hou, and A. Lou, "Wireless power transfer and applications to sensor networks," *IEEE Wireless Commun.*, vol. 20, pp. 140–145, August 2013.
- [164] A. M. Jawad, R. Nordin, S. K. Gharghan, H. M. Jawad, and M. Ismail, "Opportunities and Challenges for Near-Field Wireless Power Transfer: A Review," *Energies*, vol. 10, no. 7, 2017.
- [165] W. X. Zhong, X. Liu, and S. Y. R. Hui, "A Novel Single-Layer Winding Array and Receiver Coil Structure for Contactless Battery Charging Systems With Free-Positioning and Localized Charging Features," *IEEE Trans. Ind. Electron.*, vol. 58, pp. 4136–4144, Sept 2011.
- [166] B. L. Cannon, J. F. Hoburg, D. D. Stancil, and S. C. Goldstein, "Magnetic Resonant Coupling As a Potential Means for Wireless Power Transfer to Multiple Small Receivers," *IEEE Trans. Power Electron.*, vol. 24, pp. 1819–1825, July 2009.
- [167] T. Imura and Y. Hori, "Maximizing Air Gap and Efficiency of Magnetic Resonant Coupling for Wireless Power Transfer Using Equivalent Circuit and Neumann Formula," *IEEE Trans. Ind. Electron.*, vol. 58, pp. 4746–4752, Oct 2011.
- [168] H. Kim, C. Song, D. H. Kim, D. H. Jung, I. M. Kim, Y. I. Kim, J. Kim, S. Ahn, and J. Kim, "Coil Design and Measurements of Automotive Magnetic Resonant Wireless Charging System for

- High-Efficiency and Low Magnetic Field Leakage,” *IEEE Trans. Microw. Theory Techn.*, vol. 64, pp. 383–400, Feb 2016.
- [169] M. P. Theodoridis, “Effective Capacitive Power Transfer,” *IEEE Trans. Power Electron.*, vol. 27, pp. 4906–4913, Dec 2012.
- [170] H. Funato, H. Kobayashi, and T. Kitabayashi, “Analysis of transfer power of capacitive power transfer system,” in *2013 IEEE 10th International Conference on Power Electronics and Drive Systems (PEDS)*, pp. 1015–1020, April 2013.
- [171] J. Dai and D. C. Ludois, “Single Active Switch Power Electronics for Kilowatt Scale Capacitive Power Transfer,” *IEEE Trans. Emerg. Sel. Topics Power Electron.*, vol. 3, pp. 315–323, March 2015.
- [172] M. D. Prete, F. Berra, A. Costanzo, and D. Masotti, “Seamless exploitation of cell-phone antennas for near-field WPT by a frequency-diplexing approach,” *IET Microw. Antennas Propag.*, vol. 11, no. 5, pp. 649–656, 2017.
- [173] R. Trevisan and A. Costanzo, “A UHF Near-Field Link for Passive Sensing in Industrial Wireless Power Transfer Systems,” *IEEE Trans. Microw. Theory Techn.*, vol. 64, pp. 1634–1643, May 2016.
- [174] G. Marrocco, “Gain-optimized self-resonant meander line antennas for RFID applications,” *IEEE Antennas Wireless Propag. Lett.*, vol. 2, pp. 302–305, 2003.
- [175] K. V. S. Rao, P. V. Nikitin, and S. F. Lam, “Antenna design for UHF RFID tags: a review and a practical application,” *IEEE Trans. Antennas Propag.*, vol. 53, pp. 3870–3876, Dec 2005.

- [176] G. Marrocco, "The art of UHF RFID antenna design: impedance-matching and size-reduction techniques," *IEEE Antennas Propag. Mag.*, vol. 50, pp. 66–79, Feb 2008.
- [177] E. Perret, S. Tedjini, and R. S. Nair, "Design of Antennas for UHF RFID Tags," *Proc. IEEE*, vol. 100, pp. 2330–2340, July 2012.
- [178] F. Lolli, M. Virili, G. Orecchini, M. Dionigi, F. Alimenti, P. Mezzanotte, and L. Roselli, "Electromagnetic Characterization of Paper-Glue Compound for System-in-Package on Paper (SiPoP) Future Developments," *IEEE Microw. Compon. Lett.*, vol. 22, pp. 545–547, Oct 2012.
- [179] S. Hekal and A. B. Abdel-Rahman, "New compact design for short range wireless power transmission at 1GHz using H-slot resonators," in *2015 9th European Conference on Antennas and Propagation (EuCAP)*, pp. 1–5, May 2015.
- [180] S. Hekal, A. B. Abdel-Rahman, H. Jia, A. Allam, A. Barakat, and R. K. Pokharel, "A Novel Technique for Compact Size Wireless Power Transfer Applications Using Defected Ground Structures," *IEEE Trans. Microw. Theory Techn.*, vol. 65, pp. 591–599, Feb 2017.
- [181] E. Yablonovitch, "Photonic band-gap structures," *J. Opt. Soc. Am. B*, vol. 10, pp. 283–295, Feb 1993.
- [182] J. D. Joannopoulos, R. D. Meade, and J. N. Winn, *Photonic Crystals: Molding the Flow of Light*. Princeton University Press, 1 ed., 1995.
- [183] D. Ahn, J. S. Park, C. S. Kim, J. Kim, Y. Qian, and T. Itoh, "A design of the low-pass filter using the novel microstrip defected

- ground structure,” *IEEE Trans. Microw. Theory Techn.*, vol. 49, pp. 86–93, Jan 2001.
- [184] A. Abdel-Rahman, A. K. Verma, A. Boutejdar, and A. S. Omar, “Compact stub type microstrip bandpass filter using defected ground plane,” *IEEE Microw. Compon. Lett.*, vol. 14, pp. 136–138, April 2004.
- [185] M. K. Mandal and S. Sanyal, “A novel defected ground structure for planar circuits,” *IEEE Microw. Compon. Lett.*, vol. 16, pp. 93–95, Feb 2006.
- [186] S. U. Rehman, A. F. Sheta, and M. Alkanhal, “Compact bandstop filter using defected ground structure (DGS),” in *2011 Saudi International Electronics, Communications and Photonics Conference (SIEPCPC)*, pp. 1–4, April 2011.
- [187] Y. N. Han, B. Yang, and Q. Guo, “Design of low-pass filters with ultra-wide stopband using asymmetric DGS,” in *2013 IEEE International Symposium on Electromagnetic Compatibility*, pp. 636–639, Aug 2013.
- [188] G. M. Rafiquzzaman, A. T. Sadi, and M. N. Mollah, “A new approach to design microstrip low pass filter using novel defected ground structure,” in *8th International Conference on Electrical and Computer Engineering*, pp. 568–571, Dec 2014.
- [189] C. Florian, F. Mastri, R. P. Paganelli, D. Masotti, and A. Costanzo, “Theoretical and Numerical Design of a Wireless Power Transmission Link With GaN-Based Transmitter and Adaptive Receiver,” *IEEE Trans. Microw. Theory Techn.*, vol. 62, pp. 931–946, April 2014.

- [190] J. Hong and M. J. Lancaster, *Microstrip filters for RF/microwave applications*. Wiley, 1 ed., 2011.
- [191] N. C. Karmakar, S. M. Roy, and I. Balbin, “Quasi-static modeling of defected ground structure,” *IEEE Trans. Microw. Theory Techn.*, vol. 54, pp. 2160–2168, May 2006.
- [192] G. A. Casula, G. Montisci, and G. Mazzarella, “A Wideband PET Inkjet-Printed Antenna for UHF RFID,” *IEEE Antennas Wireless Propag. Lett.*, vol. 12, pp. 1400–1403, 2013.
- [193] R. Nair, M. Barahona, D. Betancourt, G. Schmidt, M. Bellmann, D. Höft, D. Plettemeier, A. Hübler, and F. Ellinger, “A fully printed passive chipless RFID tag for low-cost mass production,” in *The 8th European Conference on Antennas and Propagation (EuCAP 2014)*, pp. 2950–2954, April 2014.
- [194] S. Zhang, S. Li, S. Cheng, J. Ma, and H. Chang, “Research on smart sensing RFID tags under flexible substrates in printed electronics,” in *2015 16th International Conference on Electronic Packaging Technology (ICEPT)*, pp. 1006–1009, Aug 2015.
- [195] N. Javed, A. Habib, Y. Amin, and H. Tenhunen, “Miniaturized flexible chipless RFID tag for IoT market,” in *2017 International Conference on Communication, Computing and Digital Systems (C-CODE)*, pp. 71–74, March 2017.
- [196] W. Withayachumnankul, C. Fumeaux, and D. Abbott, “Compact electric-LC resonators for metamaterials,” *Opt. Express*, vol. 18, pp. 25912–25921, Dec 2010.
- [197] A. Costanzo, M. Dionigi, F. Mastri, and M. Mongiardo, “Rigorous modeling of mid-range wireless power transfer systems based on

- royer oscillators,” in *2013 IEEE Wireless Power Transfer (WPT)*, pp. 69–72, May 2013.
- [198] M. Košík, R. Fajtl, and J. Lettl, “Theoretical evaluation of bifurcation in dependence on resonance frequency in two-coil inductive power transfer,” in *2017 International Conference on Applied Electronics (AE)*, pp. 1–6, Sept 2017.
- [199] F. Mastri, A. Costanzo, and M. Mongiardo, “Coupling-Independent Wireless Power Transfer,” *IEEE Microw. Compon. Lett.*, vol. 26, pp. 222–224, March 2016.
- [200] S. Amendola, A. Palombi, and G. Marrocco, “Inkjet Printing of Epidermal RFID Antennas by Self-Sintering Conductive Ink,” *IEEE Trans. Microw. Theory Techn.*, vol. PP, no. 99, pp. 1–9, 2017.